University of California

Los Angeles

Local Parity Violation in the Strong Interactions and Parton Collectivity in Au+Au Collisions at RHIC

A dissertation submitted in partial satisfaction

of the requirements for the degree

Doctor of Philosophy in Physics

by

Dhevan Gangadharan

2010

The dissertation of Dhevan Gangadharan is approved.

George J. Morales

Charles A. Whitten Jr.

Yuanxun Ethan Wang

Huan Z. Huang, Committee Chair

University of California, Los Angeles

2010

To my parents

Table of Contents

List of Figures

List of Tables

Acknowledgments

I would like to thank my UCLA advisers Huan Huang, Charles Whitten, and George Igo for their support and encouragement of the physics topics I pursued. I would also like to thank the STAR collaboration and in particular Sergei Voloshin, Arthur Poskanzer, and Ilya Selyuzhenkov for their advise. Finally, I would like to thank Dmitry Kharzeev for his input on the theory of parity violation in QCD.

Vita

8 Jan. 1982	Born, Sacramento, California, USA.
2003	SULI Intern Stanford Linear Accelerator Center Stanford California
2004	B.S. Physics University of California at Davis
2004-2006	Teaching Assistant Department of Physics University of California at Los Angeles
2006	M.S. Physics University of California at Los Angeles
2006-2010	Graduate Research Assistant Relativistic Heavy-Ion Group University of California at Los Angeles

Publications

J. Chen, D. Gangadharan, H.Z. Huang

Parton distributions at hadronization from bulk dense matter produced in Au+Au collisions at $\sqrt{(}s_{NN}) = 200$ GeV.

Phys. Rev. C. **78**:034907. 2008.

D. Gangadharan

Measuring the Radius of the Earth from a Mountain Top Overlooking the Ocean.

The Physics Teacher **47**:8. 533-535. 2009.

B. Abelev et al.

Azimuthal Charged-Particle Correlations and Possible Local Strong Parity Violation.

Phys. Rev. Lett. **103**:251601. 2009.

D. Gangadharan

Local Parity Violation in Strong Interactions.

Proceedings of the 25^{th} *Winter Workshop on Nuclear Dynamics.* 2009.

Abstract of the Dissertation

Local Parity Violation in the Strong Interactions and Parton Collectivity in Au+Au Collisions at RHIC

by

Dhevan Gangadharan

Doctor of Philosophy in Physics

University of California, Los Angeles, 2010

Professor Huan Z. Huang, Chair

Relativistic heavy-ion collisions at the Relativistic Heavy-Ion Collider (RHIC) provide a unique opportunity to study physics under very extraordinary energy densities which only exist in the core of very dense stars and during the time of a Big Bang. Azimuthal angular correlations of particles at the Solenoidal Tracker At RHIC (STAR) allow us to study the possibility of new physics which may arise in these situations. Here we study two types of azimuthal correlations with respect to the impact parameter of the heavy-ion collision.

Azimuthal correlations which are asymmetric across the reaction-plane are shown to be sensitive to the local violation of parity in the strong interactions. Violation of parity in the weak interactions has been experimentally observed in a variety of physical systems since its discovery in 1956. It has never been experimentally observed in the strong interactions. The formalism involved with its breaking also carries over into electro-weak theory where instead of parity being broken, baryon+lepton number conservation is broken. This has implications on the matter anti-matter asymmetry we observe in the universe.

A measurement of a correlation function directly sensitive to local parity violation in the strong interactions is found to yield a signal in partial qualitative agreement with theoretical expectations. No known physics background from existing dynamical models of heavy-ion collisions has been found to mimic the signal. However, upon closer inspection of the correlation as a function of the observed charge separation, we find the signal to be even stronger over a subset of events with zero charge separation. As the signal must be caused by non-zero charge separation to be P-odd, its existence in events with zero charge separation suggests alternate P-even explanations. We conclude that since the signal is even larger in events with zero charge separation we find no convincing evidence for local parity violation in the strong interactions at RHIC.

Azimuthal angular correlations which are symmetric across the reaction-plane and across the perpendicular to the reaction-plane (e.g. v_2) are shown to be sensitive to the signatures of a 5^{th} state of matter known as the Quark Gluon Plasma (QGP). Elliptic flow (v_2) for $\pi^{\pm}$, $K^{\pm}$, K^0_s, p^+, Λ, $\Xi^{\pm}$ vs. p_t is measured. At low p_t all particles show a fair agreement with non-viscous hydrodynamical models which include a 1^{st} order phase transition to a QGP phase. This seems to suggest that some degree of thermalization is attained for low p_t particles in 200 GeV Au+Au collisions. At high p_t, a non-viscous hydrodynamical description of the data clearly breaks down. This indicates the existence of significant viscosity and/or the lack of thermalization at high p_t.

At high p_t we also observe separate v_2 saturation levels for baryons than for mesons which can be remarkably well accounted for via constituent quark number scaling. This suggests that the matter produced in 200 GeV Au+Au collisions is composed of deconfined quarks exhibiting collective behavior.

CHAPTER 1

Relativistic Heavy-Ion Collisions

The collision of ions of appreciable mass at kinetic energies much larger than their mass energies is referred to as a relativistic heavy-ion collision. Perhaps the most interesting feature of these collisions is the tremendous and unprecedented energy densities involved. To date, the highest energy density achieved in a heavy-ion collision at the Brookhaven National Laboratory is $\approx 10^{38} J/m^3$. To put this into perspective, a supersonic jet traveling at top-speed and at maximum takeoff weight reaches an energy density of only $\approx 10^{10} J/m^3$. Thus, a relativistic heavy-ion collision is roughly 10^{28} more energetically dense than even this exotic example. Clearly these collisions provide us with the unique opportunity to study matter and energy and their interactions under very extraordinary circumstances.

1.1 Initial Stages of the Collision

1.1.1 Initial Geometry of Collision

The initial state of a heavy-ion before its collision with another heavy-ion may be parameterized by 5 numbers: Energy, polarization, proton number, neutron number, and the impact parameter $(\sqrt{s}, P, Z, A - Z, b)$. Heavy-ion beams are typically unpolarized so that P=0. The impact parameter, b, is given by the distance between the centers of the two nuclei. It must also be noted that since

these nuclei travel relativistically, they experience Lorentz contraction along the direction of propagation. At the highest energies achieved at the relativistic heavy-ion collider (see chapter 2) the Lorentz factor reaches 100. At that point the size of the nucleus is contracted by a factor of 1/100 along its direction of propagation. Thus the picture of a collision we have is more like two disks colliding rather than two spheres. This is illustrated in figure 1.1. Nucleons

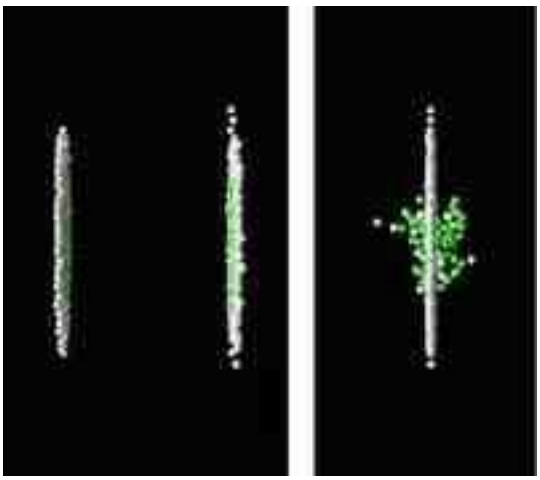

Figure 1.1: Lorentz contracted nuclei. Left-panel and right-panel show the two nuclei just before and during the moment of the collision, respectively.

of the colliding nuclei may be put into one of two categories. Those within the overlapping region of the disks are called *participant nucleons*, while those outside of this region are called *spectator nucleons*. Thus, for a collision between two identical nuclei with b=0 we have a maximum number of participant nucleons and a minimum number of spectators. These are called *central* collisions while the opposite ($b \sim$ twice gold ion radius) are called *peripheral* collisions.

In experiment the impact parameter is not an observable quantity. However, the observed multiplicity of particles is related to the impact parameter through the Glauber model of nucleus-nucleus collisions. The degree to which

nuclei collide head-on is reported as the collision centrality. The top 10% of the multiplicity distribution (central collisions) is reported as 0-10% centrality. The bottom 10% of the multiplicity distribution (peripheral collisions) is reported as 90-100% centrality. This percentage terminology will be used throughout the rest of the dissertation.

1.1.2 Initial Conditions

Particle (parton) production during the earliest moments just after the collision provides for the *initial conditions* of the phase of matter subsequently formed. In principle one may expect partons to originate from two possible sources. In one case, a parton may originate from an incident nucleon which was broken apart into its parton constituents. In the other case, a parton may originate from the spontaneous parton anti-parton emission out of the vacuum. An important distinction between the two is that while in the first case baryon number is in general introduced into the system, in the second case no baryon number is introduced. Thus the relative magnitudes of M (multiplicity observed in a detector) and N_{baryon} (baryon number observed in a detector) will provide insight into which parton production source dominates.

Heavy-ion data from three different accelerators: AGS (Au+Au, $\sqrt{s} = 5GeV$), SPS (Pb+Pb, $\sqrt{s} = 17GeV$), and RHIC (Au+Au, $\sqrt{s} = 200GeV$) show an interesting feature for $dN_{net-proton}/dy$ versus y in figure 1.2 [Bea04]. All data is from the top 5% most central collisions and errors are both statistical and systematic. The data is symmetrized across y_{CM}=0. $N_{net-proton}$ stands for the net-proton number ($N_p - N_{\bar{p}}$) and y stands for the particle rapidity. The net-proton number may be regarded as proportional to the net-baryon count, N_{baryon}. It is observed that the net-baryon rapidity density decreases with increasing collision

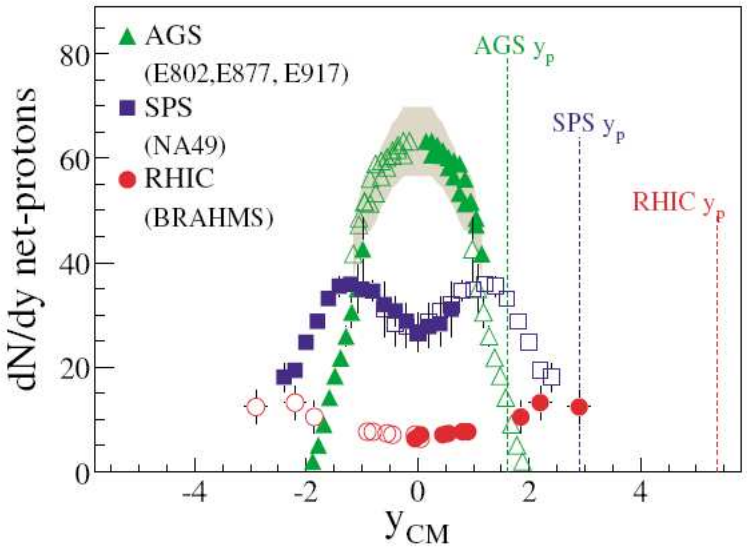

Figure 1.2: Net-proton number versus rapidity

energy. This suggests that at higher energies fewer incident quarks are themselves becoming part of the final particles observed in the detector; the nucleus has become *transparent*. This has a dramatic effect on our picture of nucleus nucleus collisions. At high enough energies, rather than incident quarks stopping and scattering outward, we have the quarks of the two nuclei *passing by each other and inducing* particle production through gluonic interactions!

To understand how parton production occurs in this scenario we look to the Bjorken picture of the space-time evolution of a high energy heavy-ion collision [Bjo83]. The target and projectile nucleus are again thought of as Lorentz contracted disks. After passing through each other, a coherent classical field is left in between the receding nuclei. This is illustrated in figure 1.3.

The receding nuclei, as we learned from figure 1.2, carry away most of the incident baryon number. The produced field in between the receding nuclei may also be thought of as a collection of excited virtual quanta. In principle, these

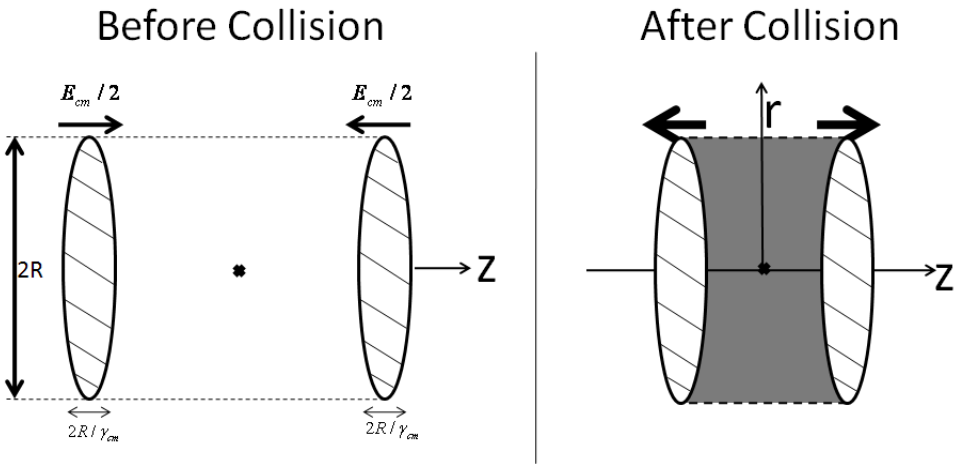

Figure 1.3: Left: Lorentz contracted nuclei before the collision. Right: After the collision a coherent classical field is left behind(gray region)

quanta may be gluons, current quarks, or even constituent quarks or hadrons provided that their formation times are small enough. The exact mechanisms for the production of these quanta is the subject of various models, i.e. Color-string breaking, Color Glass Condensate, Perturbative QCD. After some time, these excited virtual quanta will de-excite into real quanta and provide the initial conditions for an equilibrium phase. The equilibrium phase is the only realm where hydrodynamics has validity. Figure 1.4 illustrates the Bjorken picture of the space-time longitudinal evolution of high energy heavy-ion collisions. The diagonal straight lines represent the speed of light (∼spectator nuclei trajectories) and the hyperbolas indicate curves of constant proper-time.

1.2 The Quark-Gluon Plasma

Quantum chromodynamics(QCD), the theory of strong interactions, is a non-Abelian gauge field theory. In 1973 it was shown by Gross, Wilczek, and Politzer

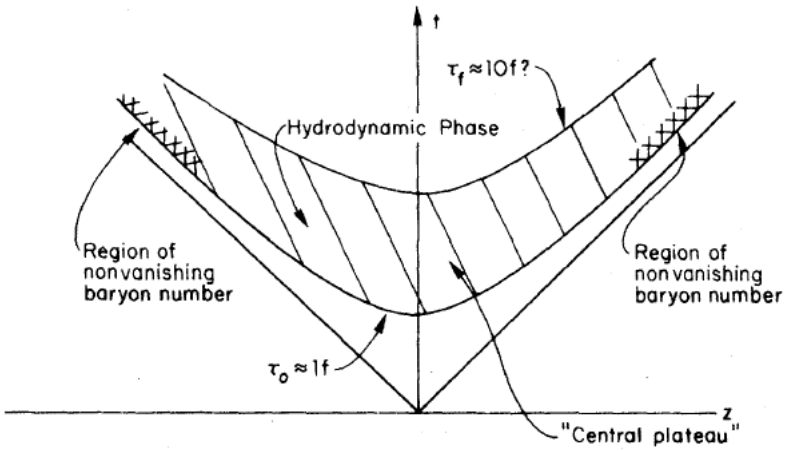

Figure 1.4: Bjorken's space-time picture of the longitudinal evolution of the produced medium in a heavy-ion collision.

[GW73] that such interacting-field theories become free-field theories at high energies. In more precise words, the coupling constant α_s of QCD decreases with increasing momentum transfer. This feature has been experimentally observed and is shown in figure 1.5. These data have the simple interpretation that quarks and gluons cease to be confined inside hadrons at sufficiently high temperatures. This is called *asymptotic freedom* or *deconfinement*. This transition from confinement to deconfinement may also be seen with lattice QCD calculations where space-time is treated as a discrete lattice (LQCD) instead of a continuum, thereby removing the ultraviolet divergences of QCD and simplifying the equations to be solved. Results for the pressure (P) of strongly interacting matter divided by temperature (T) to the fourth–which is proportional to the number of degrees of freedom–versus temperature are shown in figure 1.6 [Kar02]. From this figure it is clear that there is a sharp rise in the number of degrees of freedom (a phase transition) near $T \approx 160$ MeV. The phase beyond $T_C = 160$ MeV is a deconfined state of quarks and gluons, which, if equilibrated, constitutes a new state of matter–a 5^{th} state–and is called a *Quark-Gluon Plasma*(QGP). A Quark-Gluon

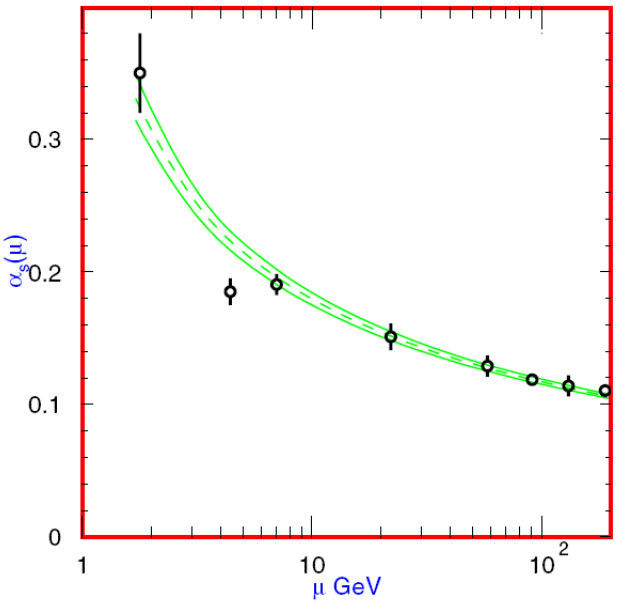

Figure 1.5: Running of the coupling constant. Data points come from a variety of experiments [Ams08]. The dotted line shows a fit with its $\pm 1\sigma$ limits as the solid lines. The parameter μ is formally regarded as the renormalization energy point, but for the purpose of this section it may be regarded simply as the energy scale.

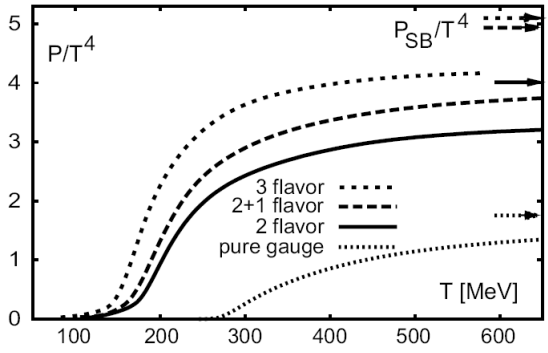

Figure 1.6: LQCD calculation for a variety of choices of dynamical quark flavors.

Plasma is analogous to an ordinary plasma in that nucleons (atoms) have dissociated into their constituent quarks-gluons (electrons-nuclei). It is believed

to exist in a heavy-ion collision in the region bounded by the two hyperbolas of figure 1.4. It should be noted that the saturation observed after T_C in figure 1.6 demonstrates that although the quarks and gluons are deconfined, they are not completely free from interactions with each other since the Stefan-Boltzmann limit is far above the curves shown. Thus, a QGP created in a heavy-ion collision may actually be a strongly interacting QGP or sQGP.

1.3 Vacuum Transitions

Another interesting feature of QCD to be explored in heavy-ion collisions is the subject of QCD vacua and their transitions. A quantum state of lowest energy (local or global) is termed *vacuum*. A vacuum is not to be thought of as empty space devoid of matter and energy but rather a state of quantum fluctuations which may bring matter in and back out of existence. Through $E = mc^2$ we know that matter can be created from pure energy and vice-versa. In Quantum Field Theory (QFT) a particular vacuum state may be parameterized by an angle θ. There are an infinite number of vacua in QCD, each corresponding to a different local minimum of energy. However, the *true* vacuum of QCD is given by $\theta = 0$, and is the absolute minimum of energy [WV84]. The other vacua are metastable.

A particular vacuum state can be parameterized by the *Chern-Simons number*, N_{CS}, which is a certain spatial integral over the gluon fields A^a_μ existing in the vacuum [Dia03], see chapter 6. Under the influence of the very large energy densities created in heavy-ion collisions, the vacuum may actually undergo a transition to another vacuum with a different N_{CS}. Perhaps the most interesting type of transitions which may occur are the very "large" transitions of the gauge fields (A^a_μ) which are parameterized by the so called *Winding numbers* and

are given by integers. A schematic diagram illustrating the potential energy of the gluon field of QCD is given in figure 1.7. Each vacuum state or minimum of

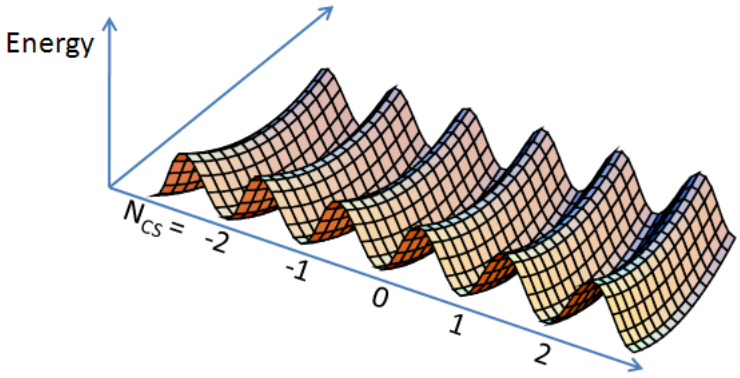

Figure 1.7: Potential energy of the gluon field

potential energy is given by a different N_{CS}. The potential energy (vertical axis) is seen to be periodic in one direction of functional space and oscillator like in all other directions (remaining axis). One very interesting feature of all non-zero N_{CS} states is that they violate the symmetry of parity (P-odd) in the strong interactions. This will be discussed in much greater detail in chapter 6.

1.4 Implications for Cosmology

Besides relativistic heavy ion collisions, the phenomena of the QGP and vacuum transitions discussed in the preceding sections may also occur in two other places: The early universe ($\approx 10^{-5} sec$ after the Big Bang), and in compact stars. Therefore, by studying relativistic heavy ion collisions we may also be learning about the rare form of matter created both in an early universe and in compact stars where energy densities are enormous.

1.4.1 Early Universe

Just after the Big Bang the Universe exhibited its largest number of symmetries. As the Universe expanded and cooled many of these symmetries were broken one by one, each at its own characteristic temperature [YHM05]. One of the first phase transitions to take place after the inflationary period was the electroweak phase transition at $T \approx 200$ GeV. After this point the electromagnetic and weak force weak became *different* manifestations of a previously singular phenomenon. This is also the point where the present asymmetry between matter and anti-matter may have arisen and where the heaviest particles such as the Higgs boson, weak bosons($W^{\pm}, Z^0$), heavy quarks(t, b and c), and the heavy lepton(τ), would have decayed into lighter particles. Next, at around $T \approx 170$ MeV($\approx 10^5$ times hotter than the center of the Sun) the QCD phase transition took place. This is where chiral symmetry was spontaneously broken and quarks/gluons combined to form hadrons (*hadronization*). Numerous other transitions occurred latter on but are not of interest here. The stage of interest here is 200 GeV$> T >$170 MeV, and is where the QGP and metastable P-odd domains were supposed to exist.

1.4.2 Compact Stars

A QGP is also hypothesized to exist in the cores of neutron stars (a subset of compact stars) [YHM05]. The content of neutron star cores has great consequences on their structure, cooling rate, and rotation. Unlike the medium created in high energy heavy-ion collisions, neutron stars have very high baryon number. A chart of T versus baryon chemical potential, μ_B, is shown in figure 1.8. Relativistic heavy-ion collisions are supposed to reach into the upper-left of the plot where the temperature is high and the baryon chemical potential is low. Neutron stars exist in the lower-right region where the temperature is low but the baryon chemical

potential is high.

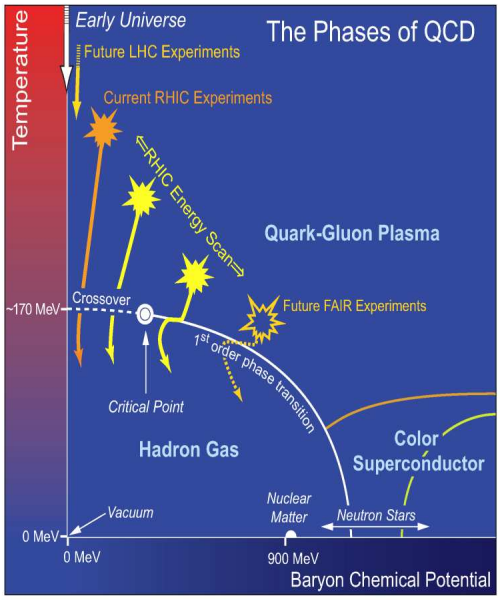

Figure 1.8: QCD Phase Diagram

1.5 Dissertation Outline

This dissertation is organized into seven chapters. The first chapter gives a very broad introduction to the physics of heavy-ion collisions. It focuses on two specific issues of QCD: the QGP and vacuum transitions. Chapter 2 introduces the Brookhaven accelerators built to study the physics of QCD under the extreme energy densities of high energy particle collisions. Chapter 3 introduces the detector at Brookhaven used in this thesis to study heavy-ion collisions. Chapter 4 introduces the concept of angular anisotropy and how different Fourier components of it may be used to search for the QGP and metastable P-odd vacua. Chapter 5 discusses the reconstruction of three weak decay particles(K^0_S, Λ, Ξ)–

some/all of which can be used to access both issues of interest. Chapters 6 and 7 are the analysis and results chapters. Chapter 6 discusses in more detail the concept of QCD vacua and a search for parity violation of the strong interactions at RHIC. Chapter 7 discusses a cumulative approach to measuring elliptic flow and its implications on the hydrodynamics of a possible QGP formed at RHIC.

CHAPTER 2

The Brookhaven Facility

The Brookhaven national laboratory was established in 1947 and is located in central Long Island New York. Heavy-ion beams at Brookhaven are linearly accelerated in five stages. From lowest to highest energy/nucleon the five stages are: the cesium sputter ion source, the tandem Van de Graaff, the booster, the AGS, and the relativistic heavy-ion collider (RHIC) which was completed in 2000. The five accelerators are linked in a chain such that the output of the previous accelerator is injected into the next accelerator for further acceleration. All components are shown schematically in figure 2.1. Also shown are the charge

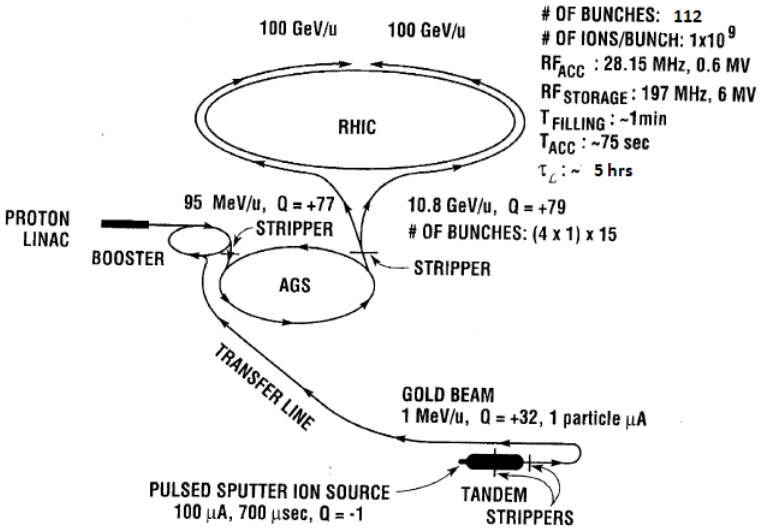

Figure 2.1: RHIC acceleration scenario for Au beams.

and kinetic energy states of Au ions at various locations. The charge state of the Au ions are seen to become increasingly positive as one goes up the accelerator chain. This is accomplished through the use of thin carbon stripping foils($\approx 15\mu g/cm^2$) [Ste01] which strip incident ions of some of their electrons as they pass through. The proton linac, also shown, is used for polarized proton beam running at RHIC. However, this is not used for heavy-ion acceleration and will not be discussed further.

2.1 Ion Extraction: The Start Of It All

Heavy-ions at Brookhaven originate at the cesium sputter source. The cesium sputter source was designed and developed chiefly by R. Middleton around 1974 [Mid83]. It operates via the bombardment (sputtering) of cesium ions on a target. The "sputtering" of cesium ions against the target liberate negative ions from the target. The freed target ions are then guided out of the chamber via an electrostatic field (similar to an electron gun). A schematic of the core components of the cesium sputter source is shown in figure 2.2. The cylindrical ionizer

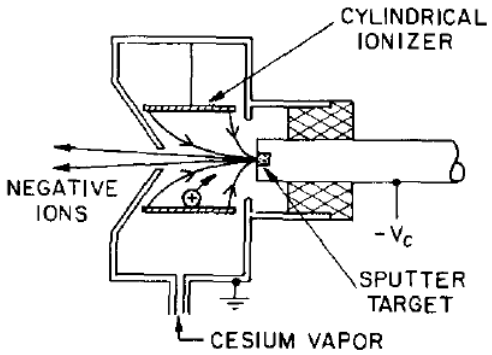

Figure 2.2: Cesium sputter source.

is used to ionize the cesium vapor ions to a positive state before they sputter the

target. In the diagram, the sputter target is held at a negative voltage while the outer shell is held at ground potential. There is thus an electric field pointing toward the sputter target which will kick the released negative target ions out of the source (to the left). An actual target holder used at Brookhaven into which solid Au may be packed is shown on the right in figure 2.3.

Figure 2.3: Empty target holder with a penny for scale.

2.2 Tandem Van de Graaff Accelerator

After exiting the source, the negative ions are next injected into a linear electro-static accelerator: the tandem Van de Graaff Accelerator. The electro-static field of a Van de Graff Accelerator is generated via the physical transport of charges (+ or -) on a conveyor belt from one region to another. The transport creates a region of depletion where charges were taken from and a region of surplus where charges were deposited. This single-stage accelerator is the simplest type of Van de Graff. A dual-stage or tandem Van de Graff is drawn in figure 2.4. One may conceptually think of a dual-stage Van de Graff as two single-stage Van de Graff's put together in tandem with their two joining regions set at the same potential. The joining region is given by the middle slice of figure 2.4 and at Brookhaven

is set to +14MV. Both ends are set to ground potential. Negative ions from the

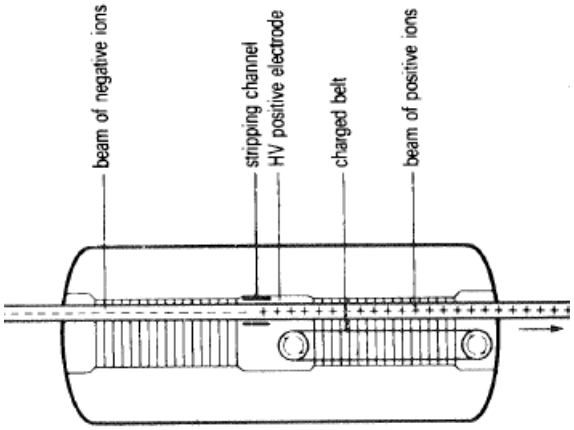

Figure 2.4: Dual-stage(tandem) Van de Graff accelerator.

source are input from the left and accelerated to the middle high voltage region. Upon entering the middle region they pass through their first carbon stripping foil ($2\mu g/cm^2$) [Ste01]. This results in a distribution of charge states of which 15% are in the desired +12e state. The resulting positive charges then receive further acceleration as they enter the second stage of the tandem where the electric field has switched sign. At the end of the tandem, the Au ions are at an energy of 1 MeV/nucleon or 197 MeV/nucleus. After the tandem, the ions pass through another carbon stripping foil, putting them into a distribution of charge states of which only the +32e state is transported to the Booster.

2.3 AGS Booster and AGS Accelerator

The next two types of accelerators used at Brookhaven are circular synchrotrons. Unlike Van de Graff accelerators, synchrotrons possess electromagnetic fields which change as a function of time (for any given point) such that the E field,

B field, and ion location are all kept in synchronization. The sections of a synchrotron which use a radio-frequency oscillating E field to impart energy into the ion are called *resonators*. Due to the wave-like oscillation of the E field along the length of the resonators at a given time, some sections will accelerate while other sections decelerate. Care must be taken to keep the beam bunches only in the accelerating regions. It is then clear that as the ions are accelerated to higher speeds, the frequency of the E fields in the resonators must also increase to keep the ions out of the decelerating regions. That is, the beam bunch locations must be kept in synchronization with the E field frequency.

Ions are kept in circularly shaped synchrotrons with the B fields created by dipole magnets. As the ions are boosted to higher and higher energies, the B fields must increase such that the ion's orbital radius remains constant, $R = p/(qB) = constant$. The dipole magnets are a dominant limitation on synchrotron performance. Typically what sets the ceiling for maximum attainable energy at a synchrotron is the dipole magnet's top field. They are also slower in response time than the E fields of the resonators. In practice, this typically translates into the B fields being ramped up at a set rate and the E fields following suit.

Formally, there are two types of synchrotrons: combined-function and separated-function. Combined-function machines use the same B field for transverse-focusing and orbit bending of the ion-beam. Both the "AGS booster" (simply called booster) and the "AGS" are combined-function machines. Separated-function machines are then ones which use different magnets for the two tasks just described. Within the combined-function class there are two further classifications for accelerators: weak-focusing and strong-focusing [Sch86]. Strong-focusing accelerators are also called alternating-gradient accelerators. The booster and the

AGS are both combined-machine alternating-gradient synchrotrons (AGS's). The AGS's use two types of dipole magnets and are drawn in figure 2.5. The first

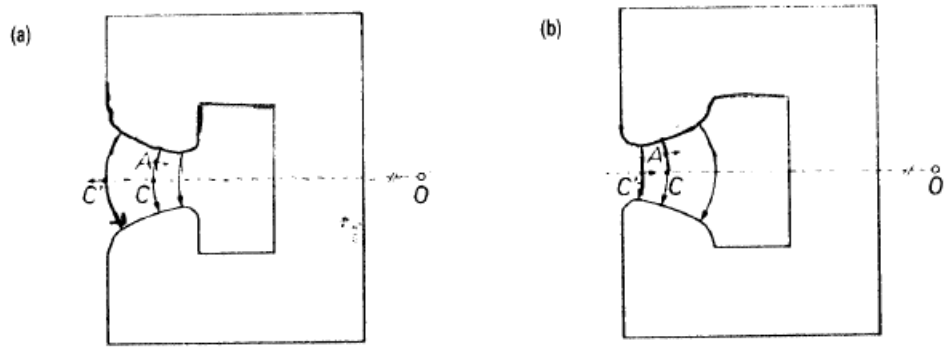

Figure 2.5: Two dipole magnets of opposite horizontal B-field components:(a) a D magnet; (b) an F magnet.

type (a) is called a D magnet since it defocuses a beam in the horizontal direction while it focuses in the vertical direction. The second type is an F magnet where the opposite is true. The gradient of the B field, $\partial B/\partial r$, is of one sign for 2.5a and is of the opposite sign for 2.5b. The AGS's achieve net focusing in both directions as well as orbit bending with the alternating configuration DFDFDF.... with appropriately chosen spacing in between. Weak-focusing accelerators on the other hand possess only one type of dipole B field gradient, D or F. Both the AGS and Booster at Brookhaven are of the strong-focusing type.

The Booster and AGS have a circumference of 201.78m and 807.12m, respectively [Bro01]. There are two more carbon stripping foils in the transfer lines after the booster and after the AGS which strip the Au ion to +77 and +79, respectively. Once in the +79 state, all electrons from the original Au ion have been removed. The AGS started up in 1960 while the booster started up later in 1991 to augment the capabilities of the AGS. Fixed-target heavy-ion collisions were conducted with the AGS until the start of RHIC in 2000.

2.4 RHIC Accelerator: The Last Boost

The relativistic heavy-ion collider (RHIC) was the first dedicated heavy-ion collider in the world. It is the last accelerator in the chain and gives the final boost of energy to Au ions after originating from the cesium sputter source. Unlike the AGS and Booster, RHIC is a dual-beam-pipe separated-function machine featuring superconducting magnets. Superconducting dipole magnets establish the beam orbit curvature while superconducting quadrapoles are used for beam focusing. Sextupoles are also used to correct for the slight defocusing nature of the dipoles. The superconducting magnets are cooled to < 4.6 K with liquid helium, allowing them to operate at higher fields [Hah03]. The RHIC ring is 3.8 km in circumference. Each beam-pipe possesses its own set of magnets. Beams circulate in opposite directions in the two beam-pipes and are brought into collision at six locations. RHIC is thus a *collider* and not a *fixed-target* experiment. Currently, there are two major experiments (STAR and PHENIX) occupying two of those locations (6 & 8 o'clock). Figure 2.6 shows the geographical layout of RHIC.

From figure 2.6 it is apparent that RHIC is not circular but instead made up of six arc sections and six straight sections. It is therefore clear that beam steering only takes place in the arc sections. Furthermore, ions gain energy–linearly accelerated–in only one of the straight sections (labeled by "rf AREA" at 4 o'clock in the figure). As with the booster and AGS, linear acceleration is done with resonating cavities driven by radio-frequency voltages. This region also shapes and maintains the bunch lengths. Table 2.1 lists important parameters for RHIC.

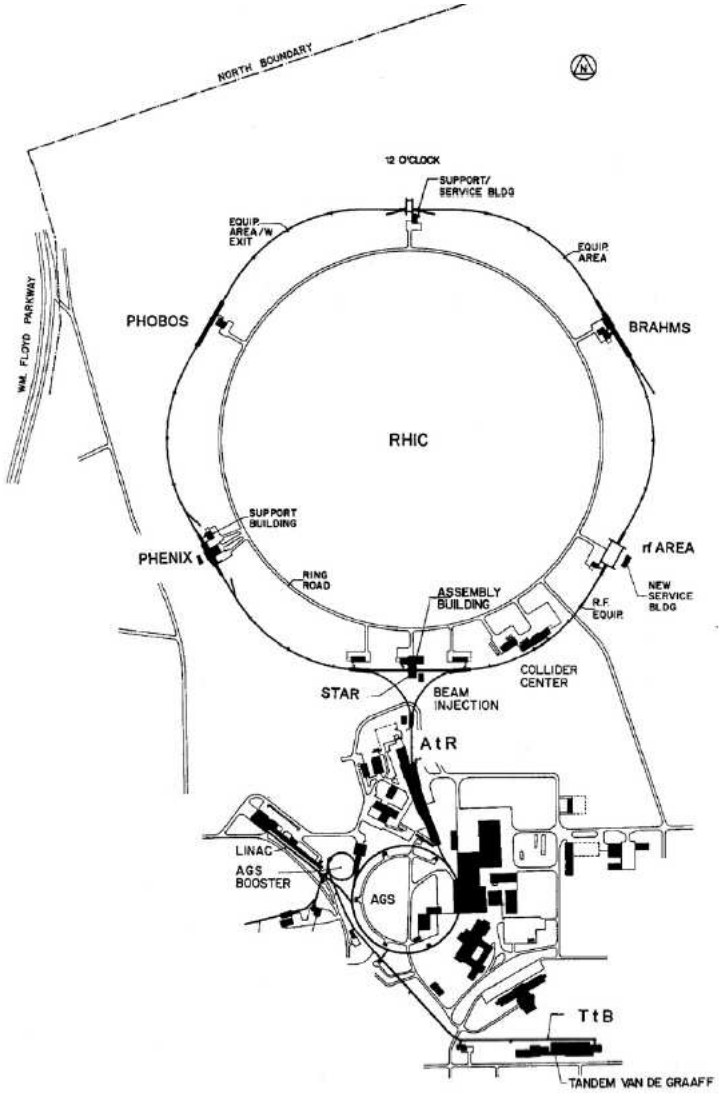

Figure 2.6: RHIC geographical layout.

Table 2.1: RHIC parameters

Kinetic energy, injection-top(each beam),	
Au	8.86-100 GeV/u
Protons	23.4-250 GeV
Luminosity, Au-Au @ 100GeV/u	$\sim 2 \times 10^{26} cm^{-2} s^{-1}$
No. of bunches/ring	112
No. of Au-ions/bunch	1×10^9
bunch length	1.52 m
Beam lifetime for Au @ $\gamma > 30$	$\sim$5 h
Circumference	3833.845 m
Beam separation in arc sections	90 cm
Number of crossing points	6
Magnetic rigidity, Bρ: @ injection	81.114 Tm
@ top energy	839.5 Tm
No. of dipoles(192/ring + 12 common)	396
No. of quadrupoles	492
Dipole field @ 100GeV/u, Au	3.458 T
Beam tube internal diameter	6.9 cm
Operating temperature via liquid He	< 4.6 K
Beam stored energy	$\sim$200 kJ

CHAPTER 3

The Solenoidal Tracker at RHIC

The detector located at the 6 o'clock interaction region in figure 2.6 is the Solenoid Tracker At RHIC (STAR). The STAR detector has full azimuthal acceptance making it possible to study a wide variety of azimuthal particle correlations. STAR's goal is to study QCD under high temperature and energy density. In particular, STAR focuses on signatures for QGP formation–a proposed 5^{th} state of matter. Data for the results in this dissertation were collected by the STAR detector.

3.1 STAR Layout and Sub-Systems

The STAR detector is analogous to an onion where the whole is composed of many layers (sub-detectors) centered axially on the beam line. The innermost layer is the Silicon Vertex Tracker (SVT) + Silicon Strip Detector (SSD). The SVT is a silicon drift detector whereas the SSD is a double-layered strip detector. The SVT plus SSD combined extend 23 cm transversely from the beam line [Arn03]. Beyond the SSD radius lies the Time Projection Chamber (TPC) used for particle tracking and identification. Beyond the TPC outer radius of 200 cm lies the Time Of Flight (TOF) detector used to extend particle identification out to higher momenta than can be done with the TPC alone. Beyond the TOF radius lies the Barrel Electro-Magnetic Calorimeter (BEMC) used to measure

electromagnetic showers from photons and electrons. Beyond the BEMC lies STAR's magnet system used to impart a curvature on TPC tracks to establish momentum measurements. Finally, beyond the magnetic system lies the Muon Tracking Detector (MTD) used for muon identification. (All of these detectors cover the entire 2π azimuth around the beam line–except the MTD.) Of these detectors, only the STAR magnet and TPC are relevant for this dissertation. They will be discussed further in the proceeding sections.

The main tracking detector at STAR is the TPC. Past its z-axis range of ± 210 cm from center [And03] lies several detectors: the End-Cap Electro-Magnetic Calorimeter (EEMC), the Forward TPC (FTPC), the Photon Multiplicity Detector (PMD), the Beam-Beam Counter (BBC), the Vertex Positioning Detector (VPD), the Forward Pion Detector (FPD), and the Zero Degree Calorimeter (ZDC). Of these detectors, only the ZDC is used for the analyses in this dissertation. It will be discussed further in section 3.2. The STAR detector with some of these sub-detectors is shown in figure 3.1.

3.2 STAR ZDC

To help decide which heavy-ion collision events are interesting and which are not, the STAR ZDC provides a minimally biased trigger (MinBias). The two ZDC's (ZDCwest, ZDCeast) are located in the forward direction on both sides of the interaction region just beyond the Dx magnets, 18 m from the TPC center. They are centered at $\theta = 0$ and subtend an angle of no more than .115° in θ [Ack03]. The ZDC's measure the energy and position of spectator neutrons liberated in a heavy-ion collision.

Spectator neutrons receive only a very tiny transverse kick during the collision

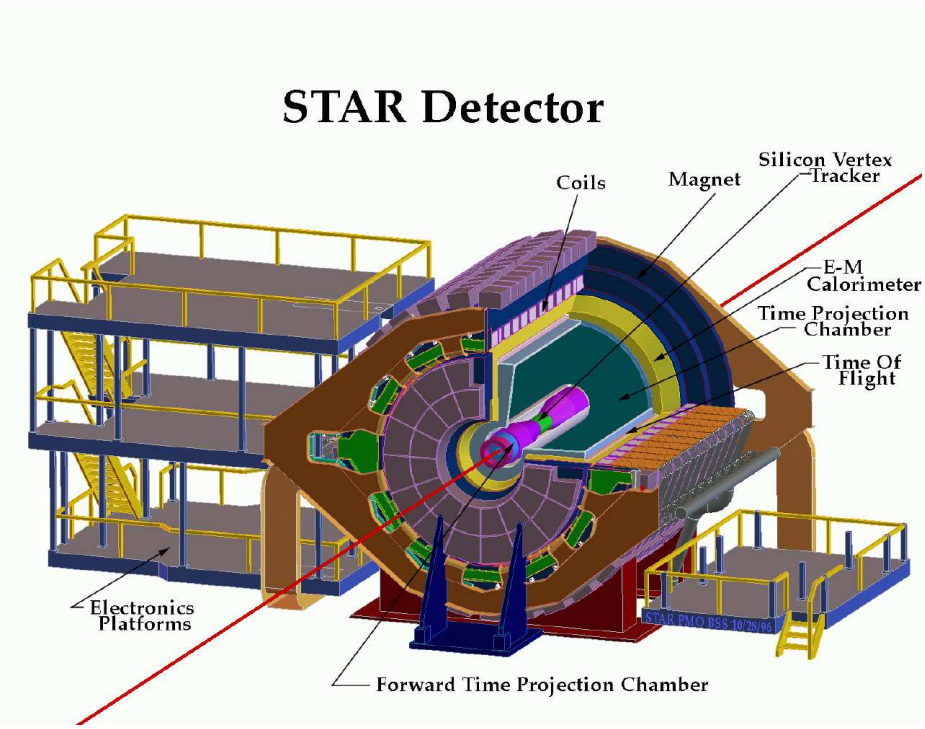

Figure 3.1: STAR detector.

while their longitudinal motion ($p_z \sim 100$ GeV/c) is mostly unchanged. Thus, to a high degree of approximation, their trajectories may be regarded as purely longitudinal. Furthermore, since the neutrons are uncharged, they are transparent to the Dx magnets and so simply pass straight through instead of being bent back into the arc sections of RHIC. Each ZDC is composed of three modules. Each module consists of an alternating series of tungsten plates and wavelength shifting fibers. The tungsten plates cause the neutrons to induce a shower of particles which radiate Cherenkov light. The Cherenkov light is captured in the proceeding layer of wavelength shifting fibers. This light is then routed to a PMT.

A minimum bias (MinBias) trigger is formed from the coincidence of ZDCwest and ZDCeast signals. Each ZDC must have a summed signal greater than $\sim 40\%$ that of a single neutron's energy [Bie03]. Comparison between ZDCwest and

ZDCeast signal timings also give an estimate of the interaction location. Most of the data presented in this dissertation uses this mimum bias trigger. Apart from a trigger, the ZDC's are also used to: monitor the beam for RHIC operation and verify centrality in heavy-ion collisions.

3.3 STAR TPC

Particle tracking at STAR is done through the Time Projection Chamber (TPC). It is a unique detector capable of digitizing 70 million voxels (three-dimensional pixels) of data per event via many channels of front-end electronics [Ack03]. The TPC is a barrel shaped detector centered on the beam-line. Its inner radius is $\sim$50 cm, its outer radius is $\sim$200 cm, and it measures $\sim$420 cm along z (beam-line). It is depicted in figure 3.2. The TPC is actually divided into two regions by a high-voltage central-membrane. While the central-membrane is kept at a high negative voltage, the two end planes are kept at ground. This clearly establishes an electric field pointing axially inward (opposite sign for both halves) with the exception of edge-effects. However, a purely axial field is desired. To attain this, the barrel outer shell is divided axially into 182 concentric field cage cylinders or rings (not shown in figure) [And03]. The ring at the middle is half on the west side ($z > 0$) and half on the east side ($z < 0$). This ring is at the same voltage as the central-membrane. The next set of rings, on either side the central ring, is set at a slightly lower voltage. This continues uniformly all the way to the end planes where the rings eventually reach the ground potential of the end plane. This is done with a chain of 183 2 MΩ resistors. The gradient of voltages across the rings help reduce edge effects and produce a purely axial field in the central volume of the TPC.

In addition to this electric field, an axial magnetic field is also applied to the

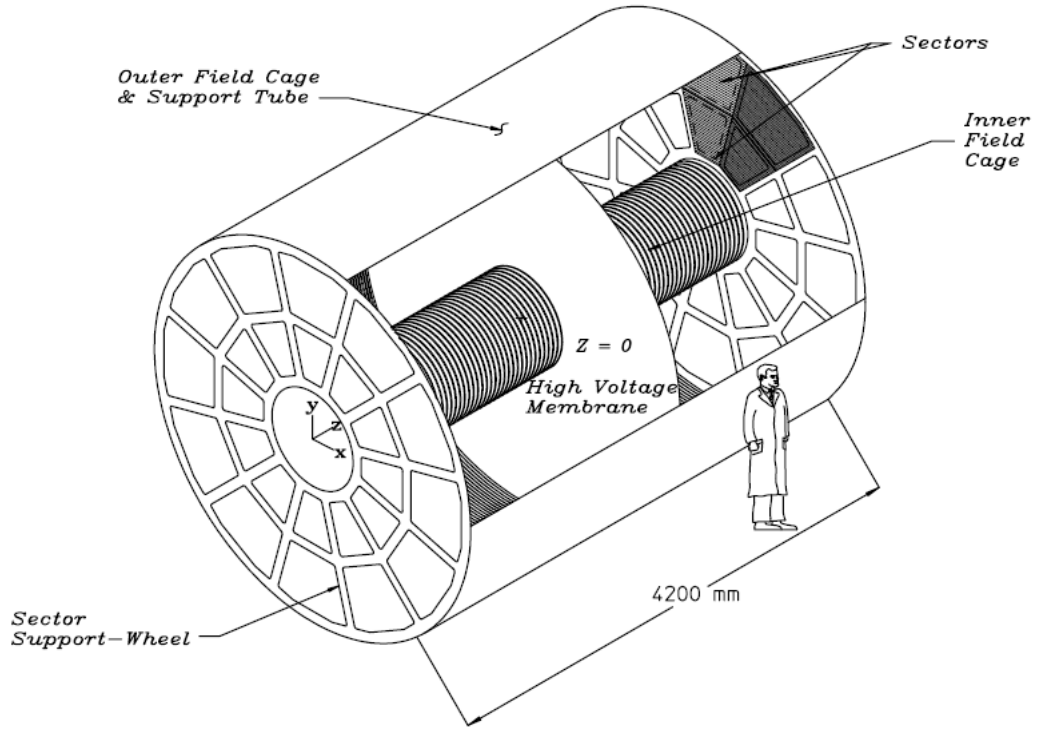

Figure 3.2: STAR detector.

TPC volume. The magnetic field is used to impart an azimuthal bend in the tracks. The radius of curvature at which a track bends is known to be directly proportional to its transverse momentum. The magnetic field is therefore used to identify a track's transverse momentum. The magnetic field is established through a set of concentric current-carrying rings outside the TPC. The rings have a cross-section of 53.9 mm x 47.5 mm and are made of aluminum [Ber03]. They also have a small hole bored in their middle region for the passage of cooling water. The maximum field attained in the TPC center is .5 T which corresponds to roughly 4500 A of current in the rings. This, with the resistivity and length of aluminum used, requires the passing water to transport $\sim$3.5 MW of thermal power. Just as for the electric field, the magnetic field must also be purely axial.

This is obtained with the help of trim coils and an outer steel yoke around the entire barrel. The trim coils introduce another B field designed to counter off-axis components near the ends of the main coils. The steel yoke serves to steer the outer return field lines and thus keep the entire B field region more contained.

The inner volume of the TPC is filled with 90% argon and 10% methane (P10 gas). A charged particle traversing a region purely filled with argon will cause excitation and ionization of the argon atoms. Excited argon atoms will then typically relax back down to a lower energy state via photon emission. If left unchecked, the photons emitted in this process will strike metalic surfaces in the TPC and release electrons through the photoelectric effect [Sau77]. This is very undesirable since it is the freed electrons in the ionization process which are recorded. A complex polyatomic molecule like methane is then inserted to quench or absorb the photons from the excitation process.

Freed electrons from the ionization process will drift toward the end planes where their signal is captured and recorded. With the applied electric field, the electrons drift at a rate of 5.45 cm/μsec toward the end planes. The freed positive ions will drift toward the central-membrane where they are absorbed but not recorded.

The end planes are divided into 12 inner and outer sectors. Each sector is composed of four planes. From smallest to highest $|z|$ (z=0 represents TPC center) they are: the gated grid, the shield grid, the anode grid, and the pad plane. They are shown in figure 3.3.

The gated grid acts as a shutter for the drifting electrons. In an 'open' configuration, the gated grid is transparent to the passage of drift electrons. In this configuration, all of the wires are biased to the same voltage which is typically 110 V. In a 'closed' configuration the wire voltages alternate $\pm$75 V from 110 V.

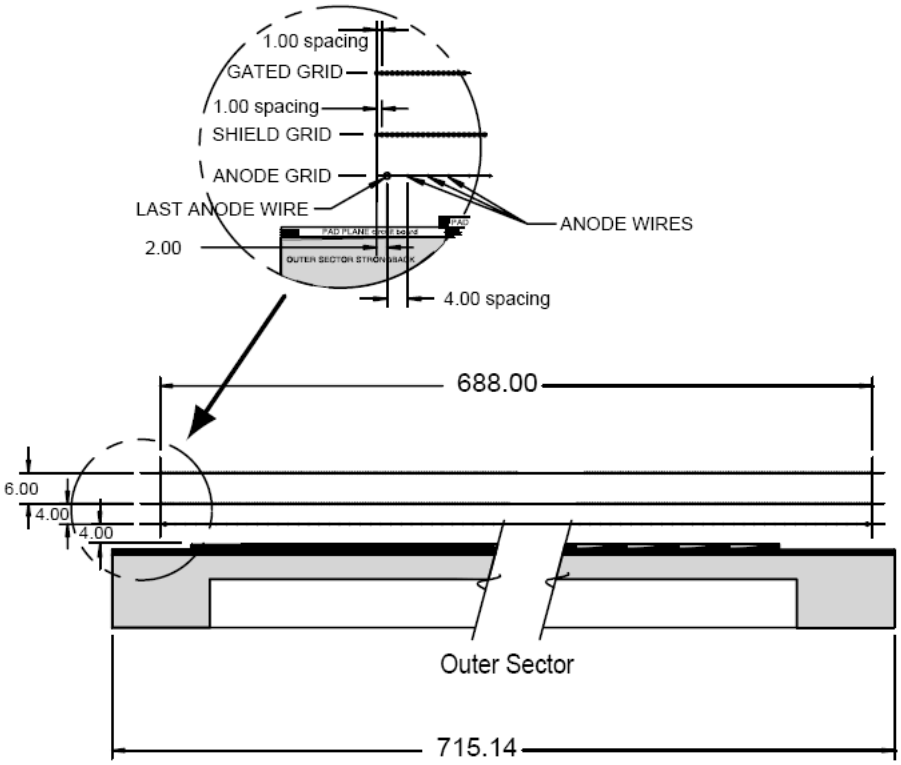

Figure 3.3: STAR TPC.

In this configuration, a transverse electric field is generated across the wires in the plane of the gated grid. Drift electrons will no longer pass straight through the wire gaps but crash into the wires instead. The gating grid is opened when an event is triggered on and closed otherwise.

Just beyond the gated grid lies the shield grid or ground grid. As its name implies, the ground grid is set to ground potential. Its primary purpose is to separate the drift region from the next region of the discussion–the MWPC avalanche region–by terminating its field lines. The avalanche region contains anode wires spaced 4 mm apart. The inner and outer sector anode wires are nominally set to 1170 V and 1390 V, respectively. The wires are aligned roughly in the azimuthal direction.

Once in close proximity to the anode wires, drift electrons undergo rapid acceleration toward the anode wires and cause an avalanche of ionization. The electrons from the avalanche are pulled toward the anode wires. Their exact hit position along an anode wire determines one hit coordinate. The second coordinate is determined from the pad in the pad plane which receives an induced signal from the avalanche. The third coordinate is determined from the drift time of the drift electrons and is where the acronym TPC gets its T. The three coordinates give the location of a particular ionization event within the TPC volume. As a charged particle ionizes not just in one spot but everywhere along its trajectory, ionization will likewise be left along the entire trajectory. One is thus left with an array of points in the TPC volume which can be put together to reconstruct the particle's trajectory, i.e. P_x, P_y, P_z. The azimuthal angle $\phi = \tan^{-1}(P_y/P_x)$ is of great importance in the analyses of this dissertation. The transverse momentum uncertainty ($\Delta p_t/p_t$) in the TPC is found to be on the order of a few % [And03]. This is estimated to correspond to $\delta\phi < 2^\circ$.

Another interesting feature which may be obtained from the drift electrons is the energy loss per unit length (dE/dx) of the ionizing particle. Energy loss of a charged particle in a TPC can occur elastically as well as inelastically but is found to primarily occur through inelastic collisions with shell electrons of the P10 gas [Leo94]. It may be mathematically modeled by the Bethe-Bloch formula with a density effect correction δ and the shell correction C:

$$-\frac{dE}{dx} = 2\pi N_a r_e^2 m_e c^2 \rho \frac{Z}{A}\frac{z^2}{\beta^2}\left[\ln\left(\frac{2m_e\gamma^2 v^2 W_{max}}{I^2}\right) - 2\beta^2 - \delta - 2\frac{C}{Z}\right] \qquad (3.1)$$

where: $2\pi N_a r_e^2 m_e c^2 = .1535$ MeVcm^2/g, r_e: classical electron radius $= 2.817 \times 10^{-13} cm$, m_e: electron mass, N_a: Avogadro's number, I: mean excitation potential, Z: atomic number of absorbing material, A: atomic weight of absorbing material, ρ: density of absorbing material, z: charge of incident particle in units

of e, β: v/c of incident particle, γ: $1/\sqrt{1-\beta^2}$, δ: density correction, C: shell correction, W_{max}: maximum energy transfer in a single collision.

From the formula it is clear that the energy loss of an incident particle depends on its charge and velocity. Thus, for a given momentum, different particles (protons, electrons, pions, kaons) will lose different amounts of energy. This feature is exploited at STAR as a means of particle identification. Figure 3.4 shows a STAR dE/dx versus momentum measurement. One can clearly identify different particle bands. For high momentum all of the particle bands merge into one band. At this point one can no longer clearly identify particles based on their dE/dx. Table 3.1 summarizes key parameters for the STAR TPC detector.

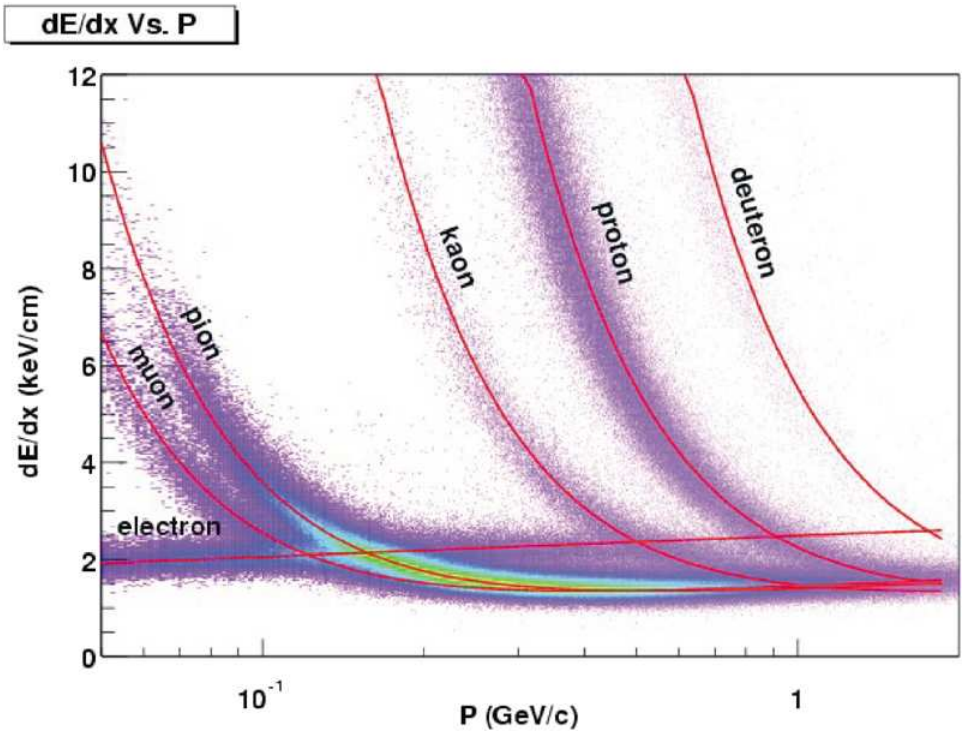

Figure 3.4: dE/dx versus momentum.

Table 3.1: TPC parameters

Item	Dimension	Comment
Length of TPC	420 cm	Two halves
Outer diameter	400 cm	Of drift volume
Inner diameter	100 cm	Of drift volume
Cathode	400 cm diameter	Central membrane
Cathode potential	-28 kV	Central membrane
Drift gas	P10	90% Ar, 10% CH_4
Pressure	Atmospheric +2 mbar	Regulated
Drift velocity	5.45 cm/μsec	Typical
Transverse diffusion(σ)	230 μm/$\sqrt{cm}$	140 V/cm and .5 T
Longitudinal diffusion(σ)	360 μm/$\sqrt{cm}$	140 V/cm
Number of anode sectors	24	12 per end
Dead space	3 mm	Between sectors
Wire diameter	20, 75 μm	Anodes, others
Anode wire to pads	2 mm, 4 mm	inner, outer sector
Anode voltage	1170 V, 1390 V	inner, outer sector
Number of pads	136,608	
Sampling rate	9.4 MHz	
Sampling depth	512 time buckets	380 time buckets typical
Magnetic field	0, $\pm$.25 T, $\pm$.5 T	Solenoidal

CHAPTER 4

Flow

In a heavy-ion collision, the plane formed by the impact parameter and the beam-line (z-axis) is called the *reaction plane*. Of the numerous types of particle correlations which may exist, the sub-group of correlations which depend on the reaction plane orientation is called *flow* while the rest is called *non-flow*. However, since the impact parameter is not experimentally observable neither is the reaction plane. Instead, an approximation to the reaction plane, the *event plane*, may be inferred from the particle distribution itself. This chapter gives an introduction into flow analyses.

4.1 Fourier Decomposition of Particle Distributions

To mathematically characterize flow, a Fourier series of the particle distribution may be used [PV98]:

$$E\frac{d^3N}{d^3p} = \frac{1}{2\pi}\frac{d^2N}{p_t dp_t dy}\left(1 + \sum_{n=1}^{\infty}\left(2a_n \sin[n(\phi - \Psi_r)] + 2v_n \cos[n(\phi - \Psi_r)]\right)\right) \quad (4.1)$$

where E is the collision center of mass energy, N is the number of particles, p is momentum, p_t is transverse momentum, y is rapidity, and a_n and v_n are the Fourier coefficients of the azimuthal modulation to the particle distribution in the transverse plane ($\perp$ beam-line). E is inserted to make the distribution invariant to Lorentz transformations. The distribution is also called an *invariant*

multiplicity distribution. The sine terms are sensitive to asymmetries across the reaction-plane and are normally excluded from the sum above as their coefficients are predicted to be much smaller than the cosine coefficients. They are included here since the first harmonic sine term is of interest in chapter 6.

The factor of 2 in the sum of equation 4.1 is inserted to give the Fourier coefficients, a_n and v_n, the simple interpretation, $\langle \sin[n(\phi - \Psi_r)] \rangle$ and $\langle \cos[n(\phi - \Psi_r)] \rangle$, respectively. Experimentally, it is not $\langle \sin[n(\phi - \Psi_r)] \rangle$ and $\langle \cos[n(\phi - \Psi_r)] \rangle$ which are measured, but rather $\langle \sin[n(\phi - \Psi_m)] \rangle$ and $\langle \cos[n(\phi - \Psi_m)] \rangle$, where Ψ_m is the m^{th} order event plane defined by the following equation.

$$\Psi_m = \left(\tan^{-1} \frac{\sum_i w_i \sin(m\phi_i)}{\sum_i w_i \cos(m\phi_i)} \right) / m \tag{4.2}$$

The sum goes over all particles i used for the event plane determination in an event. w_i is a weight which may be used to increase reaction plane resolution. The weights are typically made as a function of the p_t and η of the particle. From equation 4.2 it is evident that the reaction plane can be estimated in m different ways. Each is an independent estimation of the reaction plane which is determined from the m^{th} harmonic flow itself. In order to achieve the greatest accuracy in a flow measurement one should generally choose the event plane harmonic identical to the flow harmonic (m=n).

The reaction plane resolution for m=n case is given by

$$\langle \cos\left[n(\Psi_n - \Psi_r)\right] \rangle \tag{4.3}$$

This quantity may be determined through the correlation of calculated event planes from two different sub-sets of particles (sub-events), $\left\langle \cos[n(\Psi_n^a - \Psi_n^b)] \right\rangle$ [PV98], where Ψ_n^a and Ψ_n^b are two separate estimates of the reaction plane coming from two distinct and equally large sub-events of particles. The reaction plane

resolution in the TPC for $\sqrt{s_{NN}} = 200$ GeV Au+Au MinBias collisions for n=2 is shown in figure 4.1 as a function of centrality.

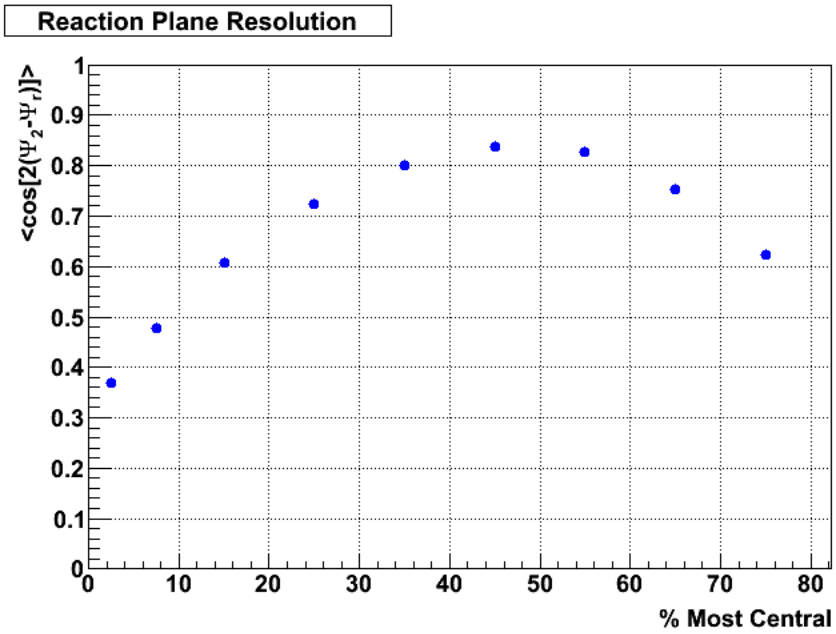

Figure 4.1: TPC reaction-plane resolution (n=2) for 200 GeV Au+Au MinBias collisions.

The physics pertaining to two Fourier coefficients are studied in this dissertation: a_1 and v_2. They are introduced in the proceeding subsections.

4.1.1 $\langle \sin(\phi - \Psi_r) \rangle$

The a_1 Fourier coefficient is a measure of asymmetries across the reaction plane. a_1 is therefore P-odd as the operation of parity ($\vec{x} \to -\vec{x}$) changes $a_1 \to -a_1$ (this is in general true for all a_n). Thus a_1 may be used as a measure of parity violation in heavy-ion collisions. a_1 may also be different for positively and negatively charged particles and so a_1^+ may be measured separately from a_1^-. In particular a_1^+ may be of a different sign than a_1^-. This particular possibility is the subject

of chapter 6 and has the simple interpretation of charge-separation with respect to (w.r.t.) the reaction plane.

4.1.2 $\langle \cos 2 (\phi - \Psi_r) \rangle$

The most commonly studied Fourier coefficient at STAR is v_2: elliptic flow. It is essentially a measure of the excess number of particles flowing either in the reaction plane (positive v_2) or out of the reaction plane (negative v_2). Elliptic flow is most commonly believed to develop from the initial spatial eccentricity of the overlap region in non-central heavy-ion collisions. The spatial anisotropy causes pressure gradients which transform this spatial anisotropy into the momentum anisotropy which v_2 measures. Elliptic flow has implications on the degree of thermalization and deconfinement established in a collision. Chapter 7 presents measurements of v_2 for various particle types.

CHAPTER 5

Reconstruction of Weak Decays

Heavy-ion collisions produce many kinds of rare particles, some of which decay into daughter particles before reaching the STAR TPC. The majority of particles that reach the TPC are one of four types: pions, protons, electrons, and kaons. Muons, deuterons and even alpha particles may also be seen directly in the TPC but to a much smaller degree. A variety of those which decay before reaching the TPC can be topologically reconstructed from their daughters. This is the subject of this chapter. Only weak decays are considered here since they can be more cleanly identified than strong (resonance) decays.

5.1 Topological Reconstruction of Weak Decays

The essence of topological reconstruction of particles is the extrapolation or tracing-back of TPC tracks to points closer to the primary vertex (typically with $r < r_{inner}$, where r_{inner} is the TPC inner radius). Daughter tracks of a parent particle will be seen to merge at one common *secondary vertex*. The 4-vector momentum of both daughters may be combined at this point to reconstruct the 4-vector momentum of the parent particle.

$$(E_{parent}, \mathbf{P}_{parent}) = (E_{daughter1}, \mathbf{P}_{daughter1}) + (E_{daughter2}, \mathbf{P}_{daughter2}) \qquad (5.1)$$

For particles undergoing a series of decays, one may do a series of reconstructions: granddaughters with granddaughters, daughters with daughters, etc. An Ω^- for instance undergoes the following decay series: $\Omega^- \rightarrow \Lambda + K^- \rightarrow p^+ + \pi^- + K^-$. The first reconstructed parent is the Λ. The second reconstructed parent is the Ω^-.

In experiment however, one must deal with detector limitations and track uncertainties. Daughter tracks will generally not always merge but instead come to some distance of closest approach (DCA), specifically a daughter-daughter DCA. Figure 5.1 illustrates two TPC tracks and their extrapolation to regions closer to a point called the primary vertex. The primary vertex is the point where a significant number of tracks are seen to merge and is taken to be the collision point. It is represented by the cross in figure 5.1. The dashed red track represents daughter1 of a certain parent particle. The dashed black track then represents daughter2 of the same parent. The curvature of these tracks is due to the TPC magnetic field which is out of the page. The blue spider-web like lines represent the TPC sector boundaries. The blue blocks at the bottom of the figure represent the TPC pads. Also illustrated is the parent decay length (shown as a thick blue line) and 3 different DCA's: daughter-daughter DCA, daughter-primary DCA, and parent-primary DCA. All together, these lengths provide a powerful set of geometrical cuts which can significantly reduce combinatoric backgrounds in particle reconstruction. The following four subsections describe the reconstruction of 4 different particles. The data come from STAR's 2007 run of 200 GeV Au+Au collisions. The trigger setup is Minimum-Bias. The centrality spans the range 10-40% (mid-central). 18.5M events were used.

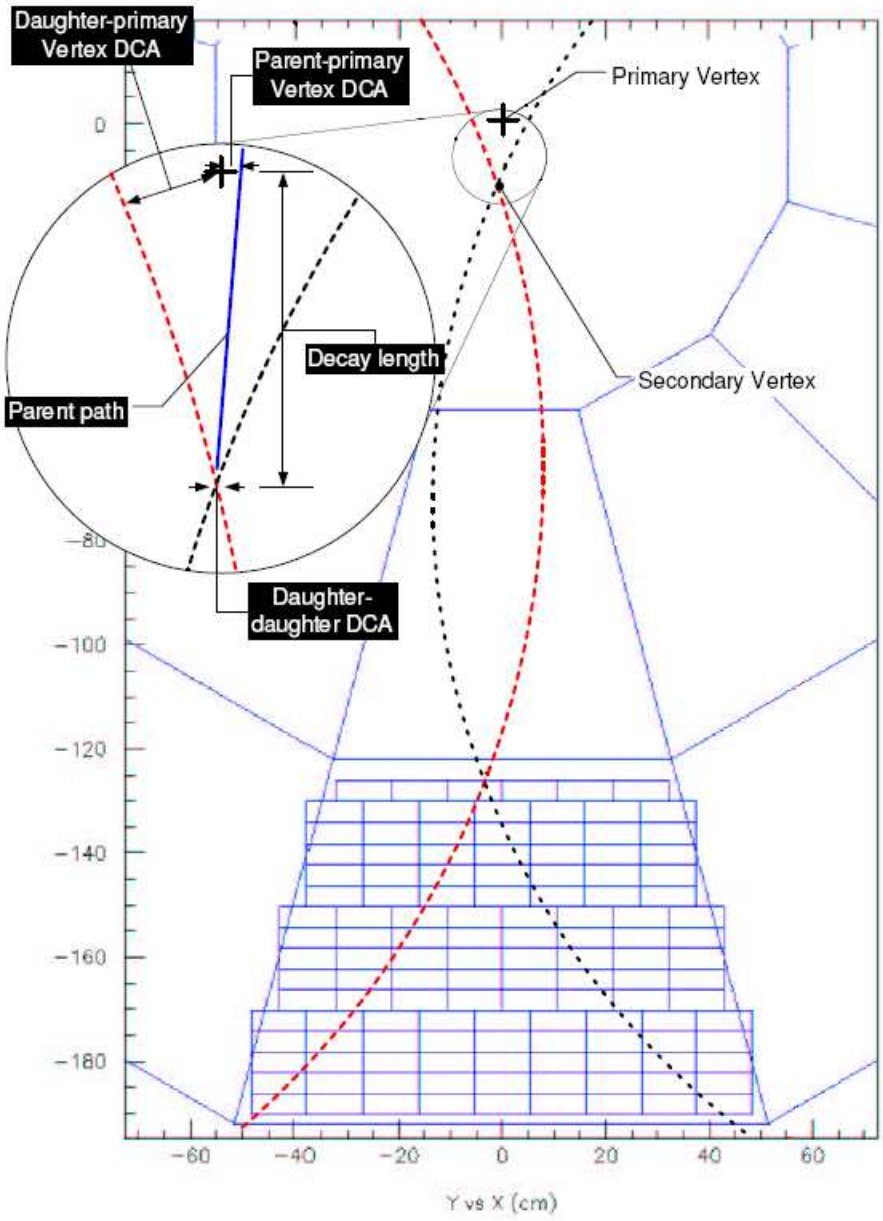

Figure 5.1: TPC track topology. Taken from [Sor03]

5.1.1 K^0_S Reconstruction

K^0_S's ($\frac{\bar{d}s+d\bar{s}}{\sqrt{2}}$) are reconstructed from its two charged pion decay channel, $K^0_S \rightarrow \pi^+ + \pi^-$, with a branching ratio of 69.2%. Table 5.1 lists key parameters and

geometrical cuts used for K^0_S reconstruction. A figure of the invariant mass dis-

Table 5.1: K^0_S parameters

mass	497.6 MeV
mean decay length ($c\tau$)	2.68 cm
K^0_S-primary vertex DCA cut	< 1 cm
pion dE/dx cut	$\|\sigma\| < 3$
pion pt cut	$> .15$ GeV/c
pion-primary vertex DCA cut	> 1.3 cm
K^0_S decay length cut	> 2 cm
pion-pion DCA cut	$< .5$ cm

tribution for the reconstruction of K^0_S with the parameters listed in table 5.1 is shown in figure 5.2. The K^0_S peak is fit with a Breit-Wigner function. A Gaussian

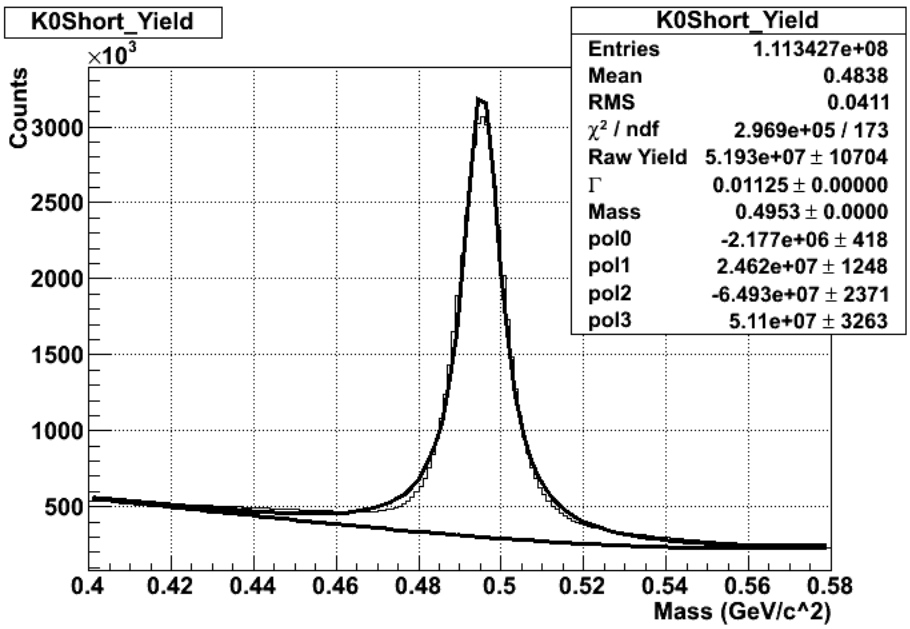

Figure 5.2: K^0_S invariant mass distribution.

fit was also attempted but resulted in a worse fit. The combinatoric background

underneath the peak is fit with a polynomial.

5.1.2 Λ Reconstruction

Λ's (uds) are reconstructed through the decay channel $\Lambda \rightarrow \pi^- + p^+$, with a branching ratio of 63.9%. Table 5.2 lists key parameters and geometrical cuts used for Λ reconstruction. A plot of the invariant mass distribution for the

Table 5.2: Lambda parameters

mass	1115.7 MeV
mean decay length ($c\tau$)	7.89 cm
Λ-primary vertex DCA cut	< 3 cm
pion, proton dE/dx cut	$\lvert\sigma\rvert < 3$
pion, proton pt cut	$> .15$ GeV/c
pion-primary vertex DCA cut	> 2.5 cm
proton-primary vertex DCA cut	> 1.5 cm
Λ decay length cut	> 5 cm
pion-proton DCA cut	$< .5$ cm

reconstruction of Λ and $\bar{\Lambda}$ is shown in figure 5.3. The Λ peak is fit with a Breit-Wigner function. A Gaussian fit was also attempted but resulted in a worse fit. The combinatoric background underneath the peak is fit with a polynomial.

5.1.3 Ξ Reconstruction

Ξ's (ssd) are reconstructed through the decay channel $\Xi \rightarrow \Lambda + \pi^- \rightarrow 2\pi^- + p^+$, with a branching ratio of 99.887%×63.9%=63.82%. Table 5.3 lists key parameters and geometrical cuts used for Ξ. The Λ daughters are reconstructed according to table 5.2. A plot of the invariant mass distribution for the reconstruction of Ξ^-

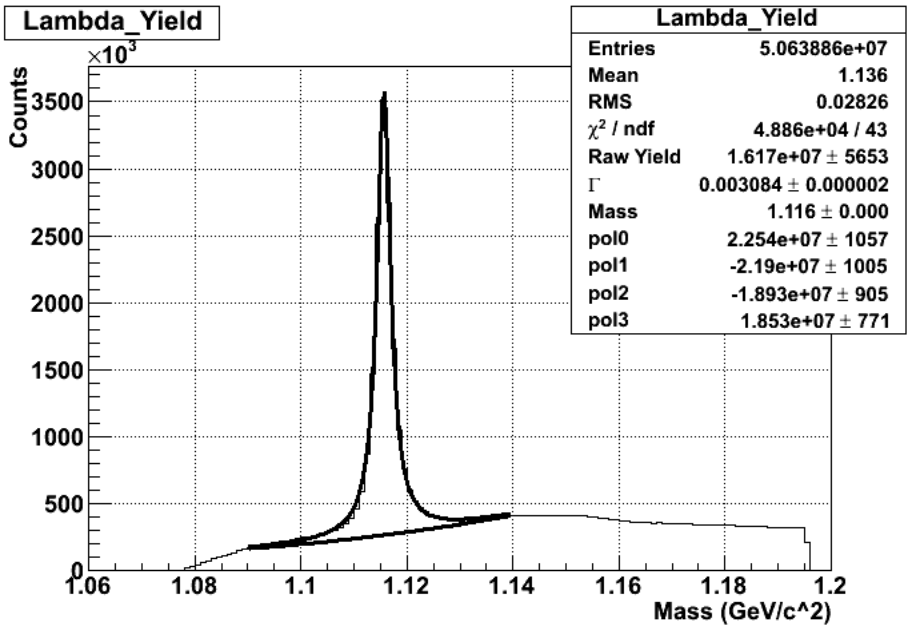

Figure 5.3: Λ+$\bar{\Lambda}$ invariant mass distribution.

Table 5.3: Cascade parameters

mass	1321.71 MeV
mean decay length ($c\tau$)	4.91 cm
Ξ-primary vertex DCA cut	< 1 cm
$\cos(\phi_\Xi - \phi_\Lambda)$	$> .9$
pion dE/dx cut	$\|\sigma\| < 3$
pion pt cut	$> .15$ GeV/c
pion-primary vertex DCA cut	> 1 cm
Lambda-primary vertex DCA cut	$> .1$ cm
Λ mass	1.105<mass<1.125
Λ-pion DCA cut	$< .64$ cm

and Ξ^+ is shown in figure 5.4. The Ξ peak is fit with a Gaussian function. The combinatoric background underneath the peak is fit with a polynomial.

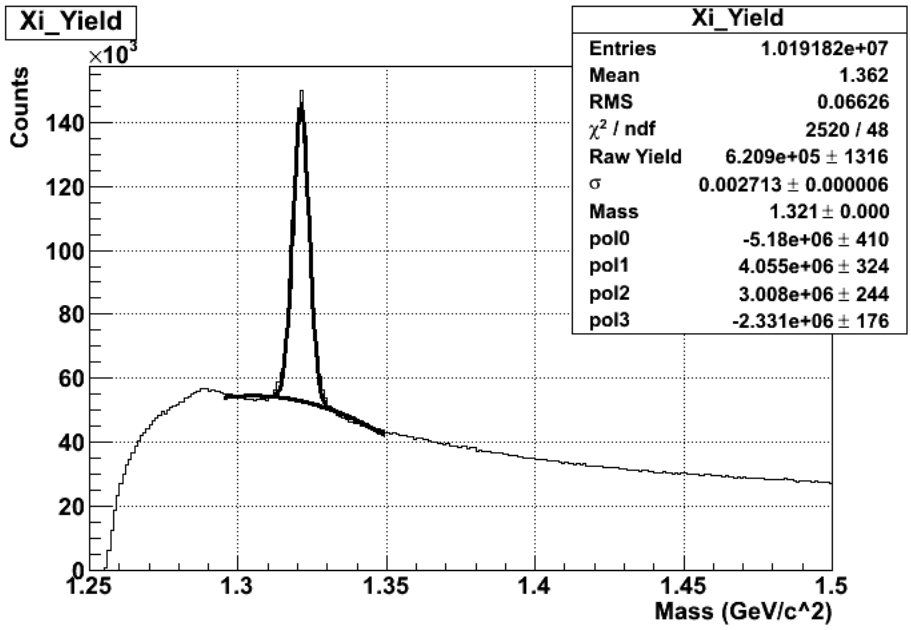

Figure 5.4: $\Xi^- + \Xi^+$ invariant mass distribution.

5.1.4 Ω Reconstruction

Ω's (sss) are reconstructed through the decay channel $\Omega \to \Lambda + K^- \to K^- + \pi^- + p^+$, with a branching ratio of 67.8%×63.9%=43.33%. Table 5.4 lists key parameters and geometrical cuts used for Ω. The Λ daughters are reconstructed according to table 5.2. A plot of the invariant mass distribution for the reconstruction of Ω^- and Ω^+ is shown in figure 5.5. The Ω peak is fit with a Gaussian function. The combinatoric background underneath the peak is fit with a polynomial.

Table 5.4: Omega parameters

mass	1672.45 MeV
mean decay length ($c\tau$)	2.46 cm
Ω-primary vertex DCA cut	< 1 cm
$\cos(\phi_\Omega - \phi_\Lambda)$	$> .9$
kaon dE/dx cut	$\lvert\sigma\rvert < 3$
kaon pt cut	$> .15$ GeV/c
kaon-primary vertex DCA cut	$> .1$ cm
Lambda-primary vertex DCA cut	$> .1$ cm
Λ mass	1.105<mass<1.125
Λ-kaon DCA cut	$< .64$ cm

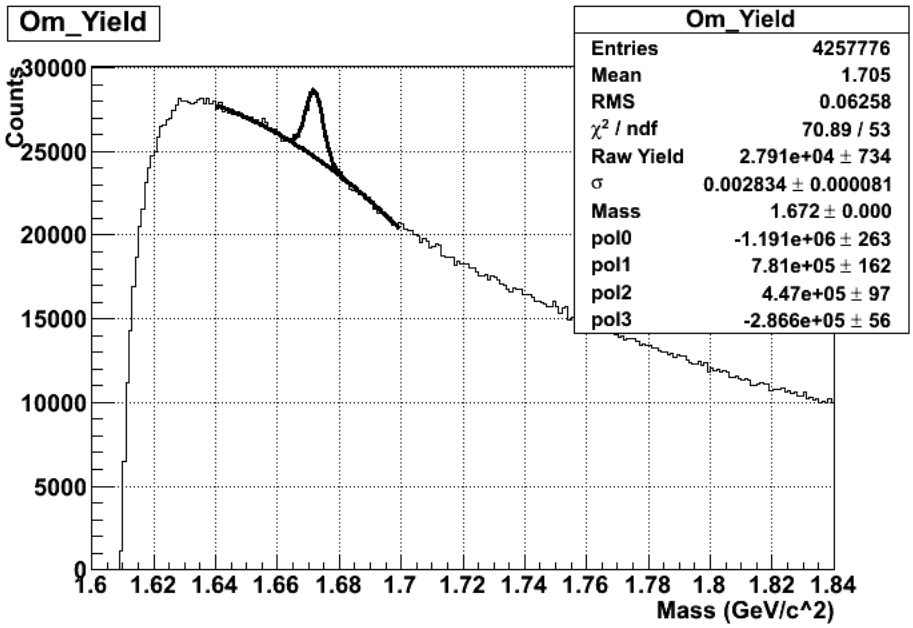

Figure 5.5: $\Omega^- + \Omega^+$ invariant mass distribution.

CHAPTER 6

Parity Violation in the Strong Interactions

Chapter 1 gave a brief introduction to the idea of vacuum transitions in QCD. This chapter extends the concept of vacuum transitions and shows how they can lead to parity violation in the strong interactions–something which has never before been observed in experiment.

6.1 Theoretical Introduction

Relativistic heavy-ion collisions provide a unique opportunity to realize the effects of vacuum transitions due to their enormous energy densities. Before the idea of a vacuum transition is discussed further, the idea of the QCD vacuum itself must be discussed. As mentioned in the first chapter, the QCD vacuum is not to be thought of as the void of everything, but rather a state of constantly fluctuating quark and gluon fields. At a given instant of time (e.g. the instant of a heavy-ion collision), the gluon fields will exhibit a certain configuration which need not be the same at the next instant of time. The structure of the QCD vacuum is governed by the mathematics of Topology. Mathematically, the spatial part of the QCD vacuum configuration at time t may be represented by the Chern-Simons number, $N_{CS}(t)$ [Dia03].

$$N_{CS}(t) = \frac{g^2}{16\pi^2} \int d^3x \epsilon^{ijk} \left(A_i^a \partial_j A_k^a + \frac{1}{3} \epsilon^{abc} A_i^a A_j^b A_k^c \right) \tag{6.1}$$

Here A_i^a, represents the gluon gauge fields of the vacuum and are functions of time and space. Indices (i,j,k) and (a,b,c) represent the spatial and color component, respectively. The more historical Pontryagin index or topological charge, ν, is the difference of Chern-Simons number at temporal infinity and negative infinity.

$$\nu = N_{CS}\left(+\infty\right) - N_{CS}\left(-\infty\right) \tag{6.2}$$

That is, ν takes into account the full evolution of N_{CS} over time. It will be useful later on to re-express ν in terms of the gluon field strength tensor ($F_{\mu\nu}^a$) and its dual ($\tilde{F}_{\mu\nu}^a$). See appendix A for a description of the field strength tensors.

$$\nu = \frac{g^2}{32\pi^2}\int d^4x F_{\mu\nu}^a \tilde{F}_{\mu\nu}^a \tag{6.3}$$

The gauge fields are assumed to die off sufficiently fast with space and time such that the integral is effectively only taken over the space-time collision region (see gauge field solution in Appendix A).

Now we come to the subject of vacuum transitions, $\frac{dN_{CS}(t)}{dt} \neq 0$. The QCD Lagrangian is invariant under distinct SU(3) gauge transformations for each space-time point. Fluctuations of the QCD vacuum can be understood as spontaneous gauge field transformations. A general gauge transformation g(x) (not the coupling constant g) in SU(3) is a function of space-time and is given by [Col85]:

$$g\left(x\right) = e^{i\lambda^a(x)T^a} \tag{6.4}$$

where $\lambda^a(x)$ is the free parameter of the transformation and T^a is an SU(3) generator (3x3 matrices). The gauge fields themselves transform as

$$A_\mu^a(x) \rightarrow g(x)A_\mu^a(x)g^{-1}(x) + g(x)\partial_\mu g^{-1}(x) \tag{6.5}$$

Given this transformation of the gauge fields it is not very apparent how our parameter describing the vacuum, N_{CS}, changes. We may nonetheless give a

very qualitative distinction between two types of transformations. The most probable transformations are small ones which incur only a very small change in N_{CS}. The less probable transformations, which are the ones of interest here, change the gauge fields by a large amount and can change N_{CS} and ν by an *integer* value. These are to be understood as vacuum transitions, i.e. a transition from one local minimum of energy to another local minimum. We will henceforth only refer to ν in talk of transitions but it is understood that N_{CS} changes by the same values as well.

An actual solution of the gauge fields to a transition of 1 unit was shown by 't Hooft and is given in appendix A. The solutions are localized in space and time. Thus, this is a "local" phenomenon, i.e. each space-time point can undergo an independent transition. The many vacua (minima) of QCD are shown schematically in figure 6.1. A transition which occurs by tunneling through the

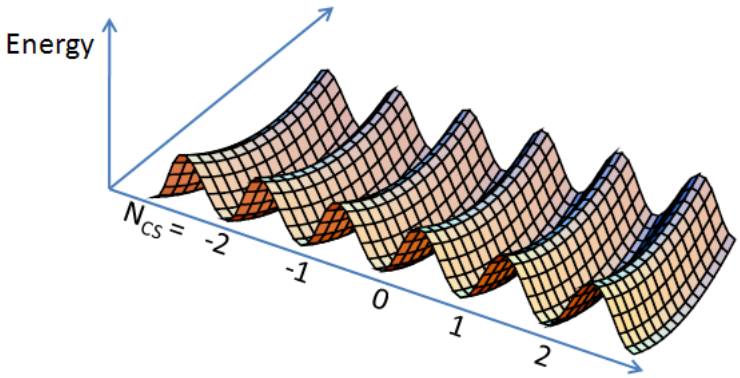

Figure 6.1: Potential energy of the gluon field. Figure adapted from [Dia03].

potential energy barrier is called an *instanton*. A transition which "goes over the top" is called a *sphaleron*. At very large energy densities such as those achieved at RHIC, 't Hooft predicts that instanton rates are heavily suppressed [Hoo76]. However, sphaleron rates are not suppressed and are predicted to dramatically

increase the total vacuum transition rate at RHIC [KMW08].

Although there are many vacua in QCD, there is still one which is unique. The unique vacuum is called the *true vacuum* and represents the gluon configuration with the lowest energy density *globally*. For this state, $\nu = 0$ [WV84]. Instantons and sphalerons, which change ν to non-zero values by an integer, represent transitions to or from "false" vacua.

6.1.1 Axial Anomaly

The axial vector current in QCD represents the flow of net handedness (left-handed - right-handed particles).

$$j^5_\mu = \bar{\psi}\gamma_\mu\gamma^5\psi \tag{6.6}$$

Its divergence or non-conservation is given by the axial or Adler-Bell-Jackiw anomaly. In the chiral limit, i.e. $m_{quarks} = 0$, the axial anomaly reads:

$$\partial^\mu j^5_\mu = -\frac{N_f g^2}{16\pi^2} F^a_{\mu\nu}\tilde{F}^a_{\mu\nu} \tag{6.7}$$

The axial anomaly is apparently related to the topological charge of equation 6.3 and therefore provides us with a profound interpretation of transitions to non-zero ν. Apparently, fluctuations of ν causes fluctuations in the net number of left/right handed quarks. The net number of left/right handed quarks (N_L/N_R) as a function of time is given by

$$N_L(t) - N_R(t) = -\int_{-\infty}^{t} dt \int d^3x \frac{N_f g^2}{16\pi^2} F^a_{\mu\nu}\tilde{F}^a_{\mu\nu} \tag{6.8}$$

This expression can be rewritten in terms of the topological charge: Inserting equation 6.3 into 6.8 we obtain

$$N_L(t) - N_R(t) = 2N_f(\nu_t - \nu_{t_0}) = 2N_f\nu_t \tag{6.9}$$

where N_f is the number of fermion flavors and ν_{t_0} is absorbed into ν_t (shifted). This equation shows that as the vacuum fluctuates to metastable states the net handedness of the system will also fluctuate. It also says that for a given state, say, positive ν, there is a preference in nature of left handed quarks over right handed quarks and vice versa for negative ν. **This is parity violation of the strong interactions!**

It should be stressed that this is not a "global" phenomenon, but rather a "local" one, i.e. the vacuum transitions are localized in space and time. Each space-time point may undergo independent and opposite transitions ($\Delta\nu = +1$ or $\Delta\nu = -1$). Integration of this effect over very large space-time volumes will average to zero. We call this type of parity violation a local parity violation.

This formalism is not strictly for QCD, but also carries over into Electro-Weak theory. An axial anomaly exists there too, but this time the quantity which is not conserved is baryon plus lepton (B + L) number. With this axial anomaly it is possible for anti-baryons to convert into leptons. The violation of baryon plus lepton number conservation could possibly explain the dominance of matter over anti-matter in the universe. In fact, the original idea to study symmetry breaking through the axial anomalies was due to 't Hooft [Hoo76].

6.1.2 The Chiral Magnetic Effect

At STAR we cannot directly observe the chirality (left or right-handedness) of particles. In order to indirectly observe this, a mechanism is needed to convert the chirality asymmetry into another type of asymmetry. *The Chiral Magnetic Effect*, proposed by Dmitri Kharzeev et al. [KMW08], is one such mechanism. The Chiral Magnetic Effect is generated by the interplay of the chirality asymmetry and the background magnetic field created in non-central heavy-ion collisions.

The existence of the background magnetic field is illustrated in figure 6.2. The

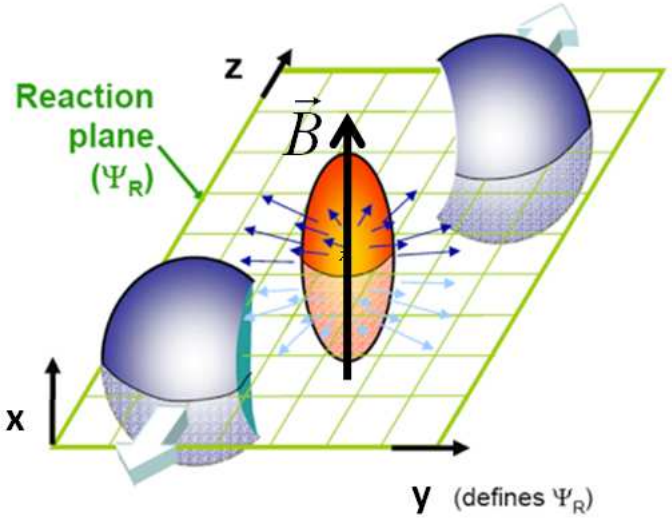

Figure 6.2: A non-central heavy-ion collision showing the magnetic field

green grid represents the reaction plane. The oval orange/red zone represents the collision participants while the blue partial spheres represent the spectators. The spectators are highly charged and are moving at speeds close to that of light. For a mid-central collision with the impact parameter $b \sim .8$ times the radius of the Gold nucleus, each blue partial sphere will contain on average half of the Gold nucleus' charge, +39.5e. They clearly constitute an ordinary electromagnetic current. This would of course produce a magnetic field at the center of the collision region which is perpendicular to the current. As one travels away from the center transverse components to the field will appear. All transverse components are ignored in this analysis. The B field in the entire interaction region is taken to be that at the center of the collision and is given by the black arrow. The magnetic field of both spectator nuclei interfere constructively. The participant region also contributes to the magnetic field as it is charged and contains orbital angular momentum as well.

A calculation of the magnetic field versus the proper time after the instant of collision, τ, is shown in figure 6.3 [KMW08]. The center of mass energy is 200 GeV per nucleon pair; the highest heavy-ion energy at RHIC. Calculations for three different impact parameters are shown. The units used are 'natural units'

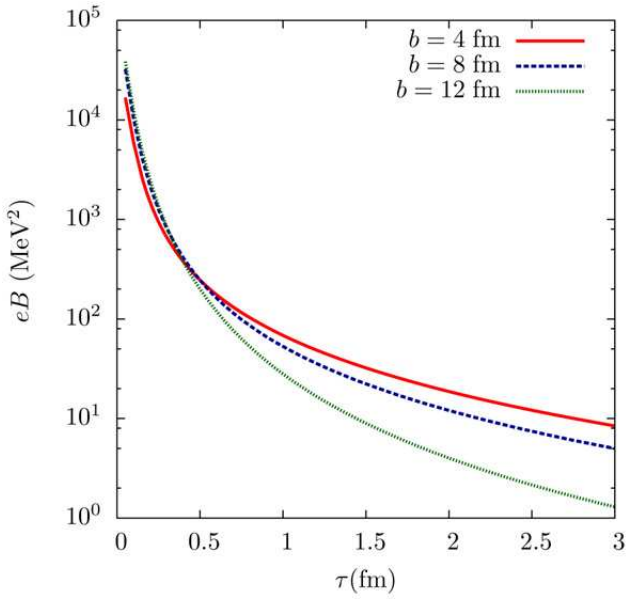

Figure 6.3: Background magnetic field for $\sqrt{s_{NN}} = 200$ GeV collisions at three different impact parameters. Figure taken from [KMW08].

where $c = \hbar = q = 1$. To convert the y-axis to more familiar units of Tesla we must express a Tesla in terms of its fundamental units (kg,m,sec,C), factor out two powers of Joules, and group the remaining units into $q\hbar c^2$ which is not equal to 1 in SI units. We find:

$$(MeV)^2 = \frac{1}{f^2 q\hbar c^2}(Tesla) \approx 1.7 \times 10^{10} Tesla \tag{6.10}$$

where f is number of MeV in a Joule, q is the electron charge, $\hbar$ is Plank's constant over 2π, and c is the speed of light. Therefore, at $\tau = .25$ the magnetic field reaches $\sim$ 17 trillion Tesla! Clearly the magnetic fields created in non-central

heavy-ion collisions are enormous but decrease very rapidly with time. To put this in perspective, the largest macroscopic magnetic field created by man in condensed matter experiments only reaches ~ 16 Tesla.

We now consider how this magnetic field will interact with the quark-gluon plasma created in the collision. Since gluons are not electrically charged they will not interact with the magnetic field B. Of course quarks are charged and are also quantum mechanical objects. Their energy levels in a magnetic field will be governed by the *Landau levels* plus the spin B field coupling [LL77].

$$E = (n + \frac{1}{2})\hbar\omega_H + p_x^2/2m - \frac{q\hbar}{mc}\vec{\sigma} \cdot \vec{B} \tag{6.11}$$

B is the magnetic field. q and m are the quark charge and mass, respectively. The first term represents the Landau levels ($\omega_H = |q|B/mc$ is the harmonic oscillator frequency). The second term is the energy from the x-component of momentum which can take on any value. The third term is the spin B field coupling ($\vec{\sigma} \cdot \vec{B} = +B/2, -B/2$). The first and third term depend linearly on the B field. Thus for very large magnetic fields all particles will be found in the lowest Landau level, n=0. This corresponds to motion either parallel or anti-parallel to the field (wave function given in Appendix B). Furthermore, positive quarks will have their spin parallel with the field while negative quarks will have their spin anti-parallel to the field. The same thing can be said about electrons (nucleons) in a magnetic field where the sign of the Bohr magneton (nuclear magneton) depends on the sign of the particle's charge.

For the following discussion we work in the chiral limit where quarks are massless and helicity = chirality. If the B field points in the positive x-direction: positive left-handed fermions and negative right-handed fermions will travel in the positive x-direction. At the same time negative left-handed fermions and positive right-handed fermions will travel in the negative x-direction. Now we

invoke the helicity change of the system which comes from the axial anomaly. After a vacuum transition has occurred we have more right handed than left-handed fermions (for the case $\nu_t = -1$). The helicity change of a particle will occur through the momentum reversal channel rather than the spin-flip channel as spin-flip is energetically suppressed with such large magnetic fields. This idea is illustrated in figure 6.4. As we can see from figure 6.4, the Chiral Magnetic Effect

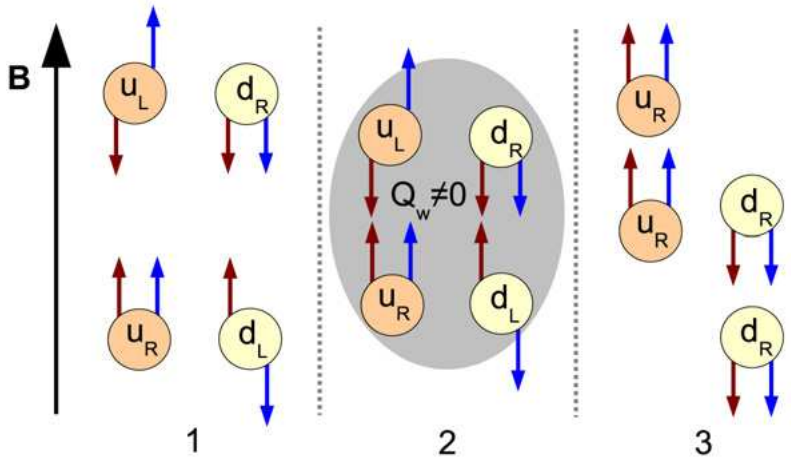

Figure 6.4: The Chiral Magnetic Effect. u and d stand for up and down quarks. L and R denote the handedness. Blue arrows (arrow on right side of quark) denote the spin direction. Red arrows (arrow on left side of quark) denote the momentum direction. In 1 we have the situation before a P-odd vacuum transition. In 2 we have the onset of a vacuum transition with $Q_w = \nu_t = -1$. In 3 we have the final configuration showing a helicity preference and charge separation. Figure taken from [KMW08].

shows that there will be charge separation relative to the plane perpendicular to the B field. This plane is the reaction-plane, so this is also **charge separation relative to the reaction-plane**. That is, a surplus of positive charges on one side of the reaction-plane and a surplus of negative charges on the other side (a

dipole moment). If we have instead a vacuum transition with $\nu_t = +1$, then the situation is just reversed. Positive and negative transitions are equally probable. Thus, the dipole moment may fluctuate from event to event.

It has been shown that the interplay of the magnetic field with the chirality asymmetry could be transformed into a charge asymmetry with respect to the reaction-plane. This we call out-of-plane charge separation. It is predicted that this effect will be too small to observe in a single collision event. Moreover, the dipole moment of this effect fluctuates from event to event. Because of this we must use multi-particle correlation techniques to study this effect in experiment.

6.2 Looking for The Chiral Magnetic Effect at STAR

The correlation functions proposed by Sergei Voloshin to measure out-of-plane charge separation with respect to the reaction-plane are [Vol04]:

$$\left\langle \cos(\phi_a^{\pm} + \phi_b^{\pm} - 2\phi_c) \right\rangle \tag{6.12}$$

$$\left\langle \cos(\phi_a^{\mp} + \phi_b^{\pm} - 2\phi_c) \right\rangle \tag{6.13}$$

ϕ is the azimuthal angle of TPC tracks a, b, and c. The charge of particle a is equal to the charge of particle b in equation 6.12. We call these *same-sign* correlations. The charge of particle a is opposite to the charge of particle b in equation 6.13. We call these *opposite-sign* correlations. In both equations particle c includes both types of charge. In this dissertation a variation of these functions is used which is qualitatively equivalent.

$$\left\langle \cos(\phi_a^{\pm} + \phi_b^{\pm} - 2\Psi_2) \right\rangle \tag{6.14}$$

$$\left\langle \cos(\phi_a^{\mp} + \phi_b^{\pm} - 2\Psi_2) \right\rangle \tag{6.15}$$

Ψ_2 is the 2^{nd} order event-plane determined through equation 4.2. It is determined from the same pool of particles which ϕ_c drew from. To further understand this correlation function we decompose the correlation into two other correlations using a trigonometric identity (opposite-sign taken for simplicity).

$$\begin{aligned} \left\langle \cos(\phi_a^{\mp} + \phi_b^{\pm} - 2\Psi_2) \right\rangle &= \left\langle \cos(\phi_a^{\mp} - \Psi_2) \cos(\phi_b^{\pm} - \Psi_2) \right\rangle \\ &- \left\langle \sin(\phi_a^{\mp} - \Psi_2) \sin(\phi_b^{\pm} - \Psi_2) \right\rangle \end{aligned} \tag{6.16}$$

If particles a and b are only correlated through the event-plane the average of the product equals the product of the averages. We may then relate the averages obtained to the Fourier coefficients of equation 4.1 and obtain

$$\left\langle \cos(\phi_a^{\mp} - \Psi_2) \cos(\phi_b^{\pm} - \Psi_2) \right\rangle = v_1^{\mp} v_1^{\pm} + NF + B_{cc} \tag{6.17}$$

$$\left\langle \sin(\phi_a^{\mp} - \Psi_2) \sin(\phi_b^{\pm} - \Psi_2) \right\rangle = a_1^{\mp} a_1^{\pm} + NF + B_{ss} \tag{6.18}$$

, where $v_1^{\pm}$ is the directed flow of positive or negative particles. $a_1^{\pm}$ are the coefficients which are directly sensitive to the Chiral Magnetic Effect. With pure charge separation we expect $a_1^{\mp} a_1^{\pm} < 0$. NF is the pure non-flow contribution, which by definition is the same for both $\langle \cos(\phi_a - \Psi_2) \rangle$ and $\langle \sin(\phi_a - \Psi_2) \rangle$. B_{cc} and B_{ss} are possible background contributions for the cos()cos() and sin()sin() parts, respectively. They represent instances where the correlation is a convolution of flow and non-flow, e.g. a flowing cluster. They may in principle be different, however the correlations of equations 6.14 and 6.15 measured in popular heavy-ion collision models like HIJING, MEVSIM, and URQMD do not show a "P-odd" signal [Abe09]. For the time being we will assume that there are no other backgrounds which will cause a "P-odd" signal, i.e. $B_{cc} = B_{ss}$. In this light we may regard the $\langle \cos() \cos() \rangle$ part of equation 6.16 as the "baseline" for the part which is directly sensitive to the Chiral Magnetic Effect, $\langle \sin() \sin() \rangle$.

Rewriting equations 6.14 and 6.15 with $B_{cc} = B_{ss}$ gives

$$\left\langle \cos(\phi_a^{\pm} + \phi_b^{\pm} - 2\Psi_2) \right\rangle = v_1^{\pm} v_1^{\pm} - a_1^{\pm} a_1^{\pm} \tag{6.19}$$

$$\left\langle \cos(\phi_a^{\mp} + \phi_b^{\pm} - 2\Psi_2) \right\rangle = v_1^{\mp} v_1^{\pm} - a_1^{\mp} a_1^{\pm} \tag{6.20}$$

6.3 Acceptance Corrections

Poor detector acceptance may introduce artificial "correlations" into equations 6.14 and 6.15. Non-uniform acceptance may be characterized by

$$c_n = \langle cos(n\phi) \rangle \neq 0 \tag{6.21}$$

$$s_n = \langle sin(n\phi) \rangle \neq 0 \tag{6.22}$$

The averages go over all particles in an event and all events (all reaction-plane orientations). It has been shown that acceptance corrections can be one of three types [SV08]. Only the dominate of the three corrections, *recentering*, is used in this chapter. To illustrate the process of recentering we first decompose the three point correlation function into single point functions using trigonometric identities.

$$\begin{aligned} &\langle \cos(\phi_a + \phi_b - 2\Psi_2) \rangle \\ &= \langle [\cos(\phi_a)\cos(\phi_b) - \sin(\phi_a)\sin(\phi_b)] \cos(-2\Psi_2) \rangle \\ &- \langle [\sin(\phi_a)\cos(\phi_b) + \sin(\phi_b)\cos(\phi_a)] \sin(-2\Psi_2) \rangle \end{aligned} \tag{6.23}$$

To apply the recentering acceptance correction to this quantity we simply make the following replacements

$$\begin{aligned} \cos(\phi) &\rightarrow \cos(\phi) - \langle\cos(\phi)\rangle \\ \sin(\phi) &\rightarrow \sin(\phi) - \langle\sin(\phi)\rangle \\ \cos(2\Psi_2) &\rightarrow \cos(2\Psi_2) - \langle\cos(2\Psi_2)\rangle \\ \sin(2\Psi_2) &\rightarrow \sin(2\Psi_2) - \langle\sin(2\Psi_2)\rangle \end{aligned} \tag{6.24}$$

Here the averages are done over all particles in all events. With this correction a particle's measured ϕ angle is effectively shifted by a certain amount depending on a detector's acceptance. The re-centering approach to acceptance corrections is used in all of the results of this chapter. Separate shifts are measured for each centrality class and RHIC run-number to improve the performance of this technique. A demonstration of how recentering affects the event-plane distribution is shown in figure 6.5. The distribution for a large number of events has to be flat since all possible reaction-plane orientations will be sampled.

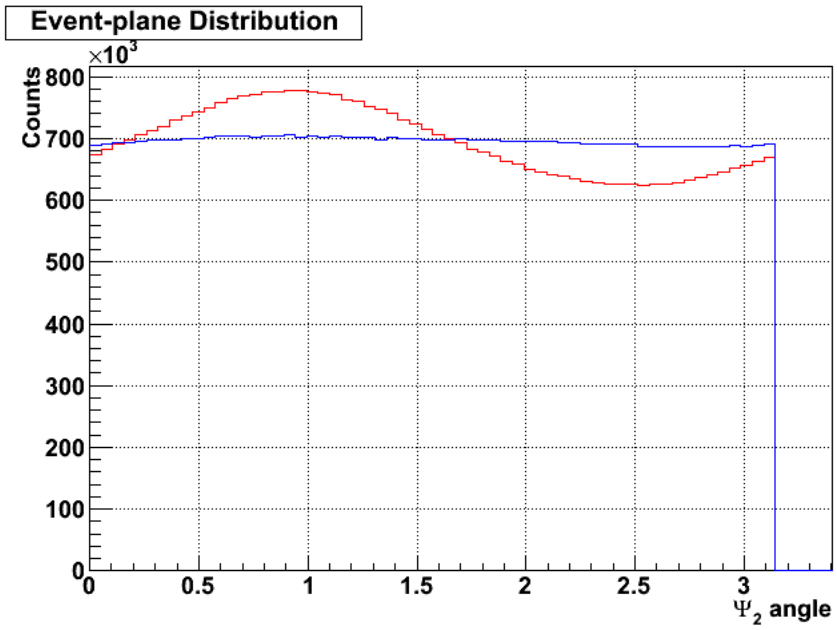

Figure 6.5: Flattening of the event-plane distribution with recentering (0-80% centrality). Red shows the distribution before acceptance corrections. Blue shows the distribution after corrections.

6.3.1 Expectations

Through the axial anomaly of QCD we could have a sphaleron vacuum transition in RHIC heavy-ion collisions. In the region of the sphaleron, the number of left-handed quarks minus right-handed quarks is not conserved. Figure 6.4 shows that this may **effectively** be regarded as **back-to-back quark anti-quark emission from the sphaleron**.

In terms of the detected hadrons in an event, we must have at least two like-charge hadrons which underwent the Chiral Magnetic Effect in order to have a non-zero same-sign correlation. If only one hadron underwent the effect the signal will be null since the other sine in equation 6.16 is uncorrelated. Two same-charge hadrons may in turn correspond to one or more back-to-back quark anti-quark

pairs emitted from the sphaleron(s). Hadron formation mechanisms (e.g. quark fragmentation or coalescence) need to be specified in order to determine this. For the opposite-sign correlations, we must have at least one pair of oppositely charged hadrons which underwent the Chiral Magnetic Effect in order to have a non-zero opposite-sign correlation. Again, hadron formation mechanisms need to be specified to assess how this corresponds to the number of oppositely charged quarks produced from the sphaleron.

For events with out-of-plane charge separation the following will be true on average: $a_1^+ = -a_1^-$. Therefore we expect $a_1^\pm a_1^\pm > 0$ and $a_1^\mp a_1^\pm < 0$. If $v_1^\pm v_1^\pm \approx v_1^\mp v_1^\pm = v_1^2$ makes a negligible contribution, then we expect $\left\langle \cos(\phi_a^\pm + \phi_b^\pm - 2\Psi_2) \right\rangle < 0$ (same-sign correlations). Likewise, we expect $\left\langle \cos(\phi_a^\mp + \phi_b^\pm - 2\Psi_2) \right\rangle > 0$ (opposite-sign correlations).

6.4 Results

6.4.1 Charged Hadrons

The same-sign and opposite sign correlations versus collision centrality for all charged hadrons detected in the TPC are shown in figure 6.6. Dataset and track parameters are displayed in table 6.1.

Several features of this plot need to be pointed out. The correlation magnitudes are very small, $\sim 10^{-4}$, but the statistical errors are even smaller (smaller than data-point size). We may now assess whether the v_1^2 term of equations 6.19 and 6.20 is negligible. A previous STAR publication [Abe08b] shows that $v_1^2 \sim 10^{-6}$ for particles in the TPC. This is 2 orders of magnitude smaller than the observed signal and is therefore negligible.

We see that the same-sign correlations are always negative. The opposite-sign

Table 6.1: Track cuts

Dataset	200 GeV Au+Au (MinBias 2007)
# Events	42 M
Track p_t	$>$ .15 GeV/c and $<$ 2 GeV/c
Track $\|\eta\|$	< 1
Primary-vertex dca	< 3 cm
Track nHits	> 15
nHits/nHitsMax	$> .52$

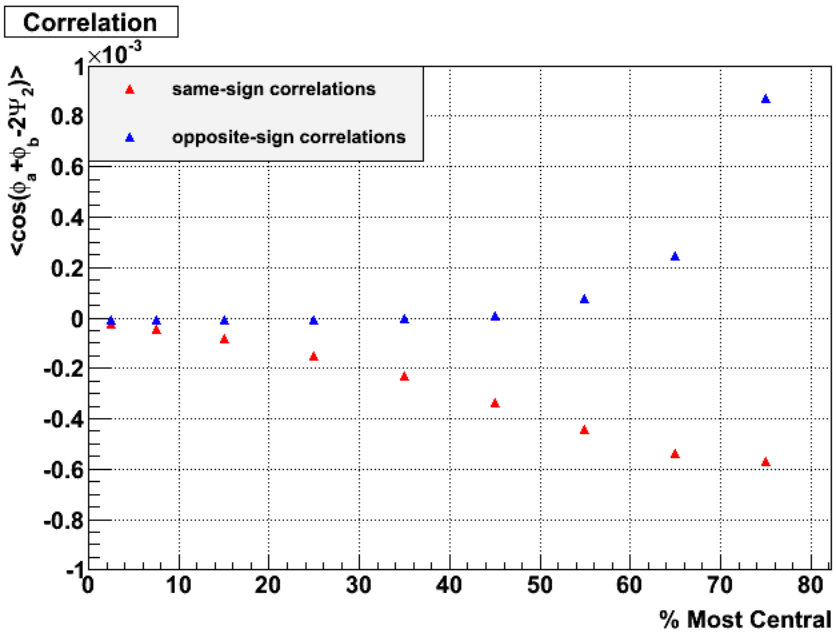

Figure 6.6: Correlation functions versus centrality. Statistical errors only.

correlations are slightly negative in central and mid-central collisions and turn positive in peripheral collisions. This feature is generally in qualitative agreement with our expectations of dynamical out-of-plane charge separation. The absolute magnitudes of either correlation increases as one goes to more peripheral collisions. The explanation for this could be a superposition of two separate

explanations. The first is that the background magnetic field produced by the spectators will be larger for more peripheral collisions which will allow for a more pronounced P-odd effect. The second is that the number of particles coming from other P-even physics processes will decrease, providing for less dilution as we go to more peripheral collisions.

Another feature of figure 6.6 is that the opposite-sign correlations are suppressed relative to the same-sign correlations in all but the most peripheral bin. This may be due to in-medium scattering. As the Chiral Magnetic Effect is a "local" phenomenon, the sphaleron could be spatially located anywhere within the nucleus-nucleus collision region. It is therefore statistically very likely that either the quark or anti-quark in a back-to-back emission will have to traverse a larger path length through the medium than the other. The number of scattering events which a particle experiences depends upon its mean free path and path length. Therefore, the particle that traverses the larger path length will scatter more and break more of the original back-to-back correlation. This would lead to a suppression of opposite-sign correlations.

Also, by virtue of the track cut: primary-vertex dca < 3 cm we can be assured that the majority the correlations present will be due to the strong interactions. Tracks with very large primary-vertex dca are typically products of weak-decays and are cut out of this analysis.

Figure 6.7 now shows the correlation average split up into its $\langle \cos() \cos() \rangle$ and $\langle \sin() \sin() \rangle$ parts. We see that in all cases the sine parts are smaller in magnitude than the cosine parts. This is still consistent with the idea of dynamical out-of-plane charge separation if–as we already assumed–$B_{cc} = B_{ss}$ in equations 6.17 and 6.18. That is, the background contamination for both sine and cosine parts is given by the cosine part alone. We observe the sine parts to deviate from the

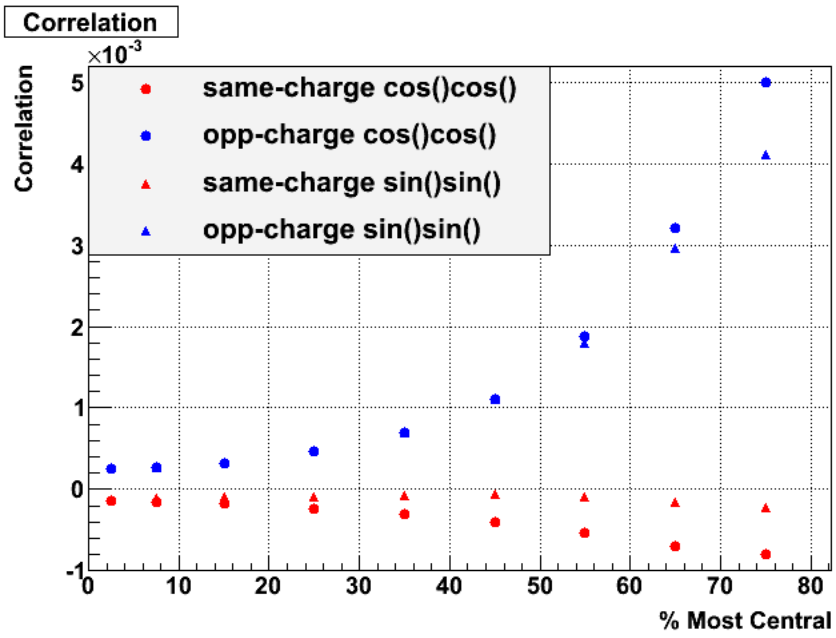

Figure 6.7: $\langle \cos(\phi_a - \Psi_2) \cos(\phi_b - \Psi_2) \rangle$ and $\langle \sin(\phi_a - \Psi_2) \sin(\phi_b - \Psi_2) \rangle$ shown separately. Statistical errors only.

cosine parts in a manner which is expected by dynamical out-of-plane charge separation.

Figure 6.6 is a higher statistics version of the flagship result of a very recently published PRL [Abe09]. There, the correlation was also measured in Cu+Cu collisions and yielded a similar signal. Presented in this publication is also the result of the correlation functions measured in several heavy-ion physics models: HIJING, MEVSIM, and URQMD. These models do not contain the parity violation effect we are looking for and thus serve as a reasonable background check. Figure 6.8 is taken directly from this publication. The x-axis of figure 6.8 is backwards relative to figure 6.6. The colored wavy bands represent an estimate of the systematic errors. The thick lines represent the reaction-plane independent background from HIJING ($\langle \cos(\phi_a - \phi_b) \rangle$). What is apparent from figure 6.8 is that

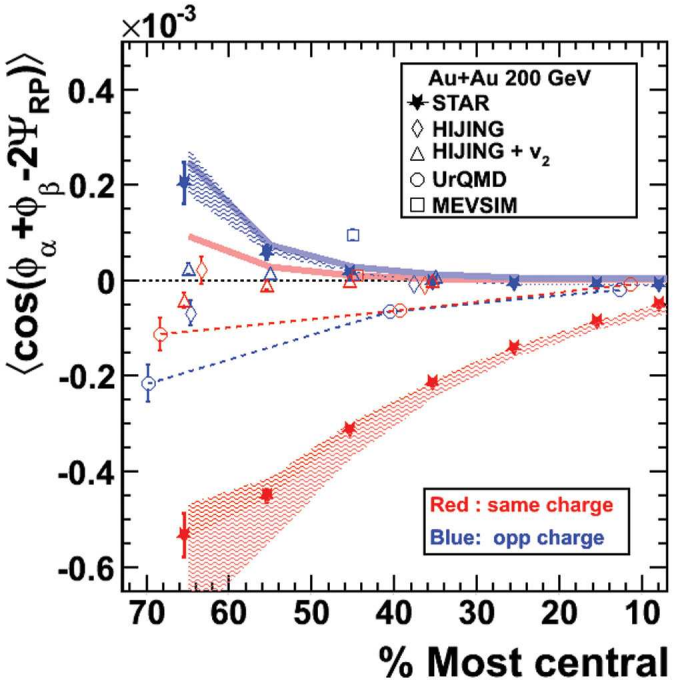

Figure 6.8: Heavy-ion model comparisons with real data. Plot taken from [Abe09].

no model simultaneously reproduces both the qualitative and quantitative results of both opposite-sign and same-sign correlations from the real data. Moreover, only one model (HIJING+v_2) can even generate the correlations for same-sign and opposite-sign charges with a sign consistent with data despite very different magnitudes. All in all, this was taken as evidence for the discovery of local parity violation in strong interactions.

The correlations are now shown with respect to the longitudinal variable: $\theta = 2\tan^{-1}(e^{-\eta})$. η is the pseudorapidity of a particle. The θ's of the two particles are combined in two ways ($\Delta\theta$ and $\langle\theta\rangle$) and the correlation plotted against each.

Figure 6.9 shows the correlations as a function of $|\theta_a - \theta_b|$. The opposite-sign

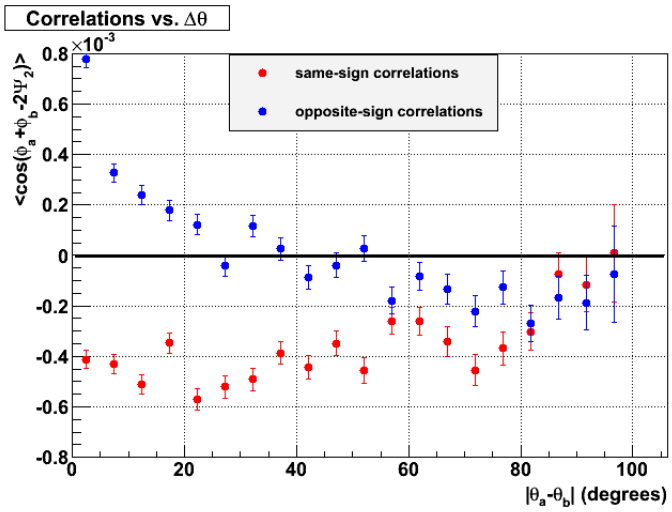

Figure 6.9: Correlations versus $|\theta_a - \theta_b|$. 50-80% centrality. Statistical errors only.

correlations are peaked at low relative θ. From our expectations of back-to-back quark anti-quark emission this would seem to suggest that the *emission axis* would be preferentially aligned perpendicular to the beam-line ($\eta = 0$). For the same-sign correlations we see a rather broad trend. From our expectations, this would seem to suggest that like-charge particles from a particular sphaleron decay are emitted with a rather broad range in relative θ.

The correlations versus $(\theta_a + \theta_b)/2$ (average θ) are shown in figure 6.10. Any asymmetries across $\theta = 90°$ seen here must be caused by detector inefficiencies. The role of same-sign correlations against average θ in evaluating our expectations is that of opposite-sign correlations against $\Delta\theta$. That is, both types assess the emission axis distribution (neglecting multiple scattering in the medium). However, the same-sign results of figure 6.10 are inconsistent with the opposite-sign results of figure 6.9. Inclusion of multiple scattering in the medium may explain why the same-sign results of figure 6.10 are flat but the same reasoning–if not more so–should apply to the opposite-sign results of figure 6.9.

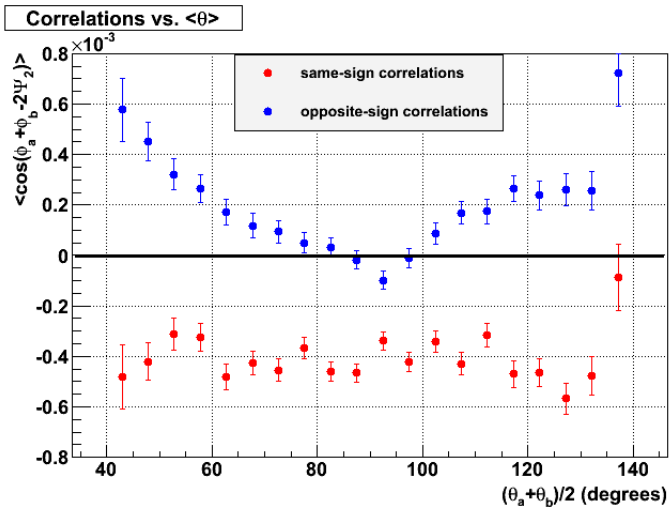

Figure 6.10: Correlations versus $\langle\theta\rangle$. 50-80% centrality. Statistical errors only.

For the opposite-sign correlations in figure 6.10 we expect $\langle\theta\rangle \approx 0$ since they are back-to-back (before scattering). Thus, we should expect the distribution to be sharply peaked at $\langle\theta\rangle = 0$. Scattering would again tend to flatten the distribution. However, what we see is distinctly not peaked at zero nor flat!

6.4.2 $\Xi^{\pm}$ Results

Topologically reconstructed Ξ's present an interesting possibility of displaying the Chiral Magnetic Effect. The valence quarks of Ξ are all of like charge (ssd). In principle it is possible for all three of its quarks to participate in the Chiral Magnetic Effect and later coalesce to form a Ξ. If this is the case, Ξ^{+}'s would flow to the opposite side of the reaction-plane than Ξ^{-}'s (charge separation again). This effect can be measured with equations 6.14 and 6.15 by replacing particle a and particle b with Ξ's. However, the number of Ξ's per event is far too low ($<<$ 1 per event) to correlate Ξ^{+}'s with other Ξ^{-}'s. Instead we correlate Ξ's with the rest of the charged hadrons in the event. That is, we only replace particle a

and measure $\langle\cos(\phi_\Xi + \phi_b - 2\Psi_2)\rangle$ for both charge combinations as before.

The results are shown in figure 6.11 with a total sample size of $\sim$ 1.2M Ξ's. Reconstruction of Ξ's are done with the cuts outlined in chapter 5. Overall, these

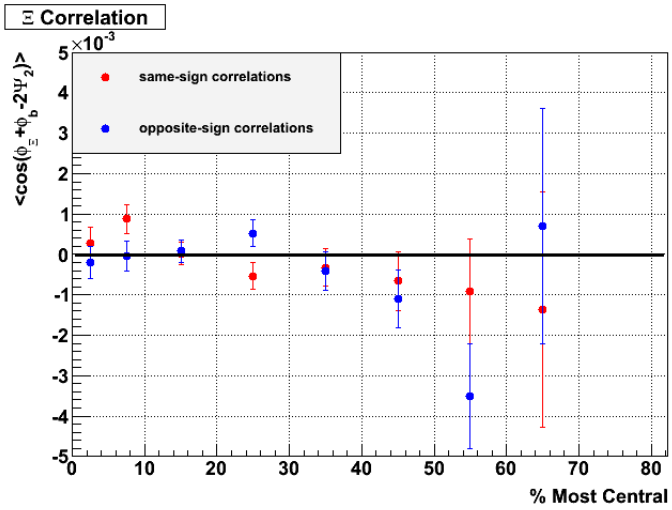

Figure 6.11: Ξ correlations versus centrality. Statistical errors only.

results are consistent with zero. Only at 25% centrality do both correlations differ from zero non-statistically. At no other centrality bin is this behavior repeated. In order to make a more statistically significant statement here, it is estimated that a factor of four more Ξ's are needed.

6.5 Modulated Sign Correlations of $\langle\cos(\phi_a + \phi_b - 2\Psi_2)\rangle$

The correlation function $\langle\cos(\phi_a + \phi_b - 2\Psi_2)\rangle$ is a correlation of two particles with respect to the event-plane. This section seeks to understand how much of the signal in figure 6.6 is by virtue of the two particles being on the same or opposite side of the event-plane independent of the precise angle they are apart from each other and the event-plane. We call this piece of the correlation function *sign correlations*. Again, the main prediction of the Chiral Magnetic

Effect is out-of-plane charge separation, which sign correlations are still sensitive to.

To see the sign correlations mathematically we rewrite the right hand side of equation 6.16 (dropping the charge superscripts).

$$\begin{aligned}\langle\cos(\phi_a - \Psi_2)\cos(\phi_b - \Psi_2)\rangle - \langle\sin(\phi_a - \Psi_2)\sin(\phi_b - \Psi_2)\rangle \\ = \langle S_a S_b M_a M_b\rangle_{in-plane} - \langle S_a S_b M_a M_b\rangle_{out-plane}\end{aligned} \tag{6.25}$$

Here "in-plane" refers to the $\langle\cos()\cos()\rangle$ part of the correlation since it is most sensitive to particles near the event-plane. "Out-plane" refers to the $\langle\sin()\sin()\rangle$ part of the correlation since it is most sensitive to particles near the perpendicular to the event-plane. S is the sign ($\pm$) of an individual cosine(sine) for the in-plane(out-plane) part. M is the absolute magnitude of an individual cosine(sine) for the in-plane(out-plane) part. Sign correlations result when we make two reductions to equation 6.25: $\langle SM\rangle = \langle S\rangle\langle M\rangle$ and $\langle M_a M_b\rangle = \langle M_a\rangle\langle M_b\rangle$. That is, we ignore the cases when the magnitudes are correlated to the signs and when the magnitudes are correlated with each other. The correlation is now given by

$$\left[\langle S_a S_b\rangle\langle M\rangle^2\right]_{in-plane} - \left[\langle S_a S_b\rangle\langle M\rangle^2\right]_{out-plane} \tag{6.26}$$

This equation represents the sign correlations ($\langle S_a S_b\rangle$) modulated by the average magnitude squared ($\langle M\rangle^2$). They are modulated to allow for direct comparison with figure 6.6 later on. The sign correlations are now rewritten in terms of the $N_{\pm}^{T,B}$ and $N_{\pm}^{L,R}$: the observed number of positive/negative particles on top/bottom of the event-plane and left/right of the perpendicular to the event-

plane, respectively.

$$\begin{aligned}
\left\langle S_a^{\pm} S_b^{\pm} \right\rangle_{in-plane} &= \left\langle N_{\pm}^{L,R}(N_{\pm}^{L,R}-1) - 2N_{\pm}^{L} N_{\pm}^{R} \right\rangle \\
\left\langle S_a^{\pm} S_b^{\pm} \right\rangle_{out-plane} &= \left\langle N_{\pm}^{T,B}(N_{\pm}^{T,B}-1) - 2N_{\pm}^{T} N_{\pm}^{B} \right\rangle \\
\left\langle S_a^{\mp} S_b^{\pm} \right\rangle_{in-plane} &= \left\langle 2N_{+}^{L,R} N_{-}^{L,R} - 2N_{\pm}^{L} N_{\mp}^{R} \right\rangle \\
\left\langle S_a^{\mp} S_b^{\pm} \right\rangle_{out-plane} &= \left\langle 2N_{+}^{T,B} N_{-}^{T,B} - 2N_{\pm}^{T} N_{\mp}^{B} \right\rangle
\end{aligned} \tag{6.27}$$

The modulation factor $\langle M \rangle^2$ for events with radial and elliptic flow only is analytically given by

$$\begin{aligned}
\langle M \rangle^2_{in-plane} &= \left[\frac{2}{\pi} \left(1 + \frac{2v_2}{3} \right) \right]^2 \\
\langle M \rangle^2_{out-plane} &= \left[\frac{2}{\pi} \left(1 - \frac{2v_2}{3} \right) \right]^2
\end{aligned} \tag{6.28}$$

We investigate the sign correlations in two different modulation scenarios. First we consider the case when the particle $\phi - \Psi_2$ distribution is flat ($v_2 = 0$) and $\langle M \rangle^2_{in-plane} = \langle M \rangle^2_{out-plane} = \left[\frac{2}{\pi}\right]^2$. This type of modulated sign correlation (MSC) may be thought of as the full correlation function ($\langle \cos(\phi_a + \phi_b - 2\Psi_2) \rangle$) under the randomization of particle angles preserving only which side of the event-plane they belong to. The result for this type of modulated sign correlation is shown in figure 6.12. It is apparent that the full correlation (Eq. 6.25) is well reproduced by these simpler modulated sign correlations.

Second we consider the case when the particle $\phi - \Psi_2$ distribution contains radial + elliptic flow ($v_2 \neq 0$). The modulation factor will now be greater than $2/\pi$ for the "in-plane" part and less than $2/\pi$ for the "out-plane" part. This is the more realistic case since surprisingly large amounts of elliptic flow were indeed discovered at RHIC [Abe08a]. These results are shown in figure 6.13. The qualitative features of the full correlation are also reproduced by the MSCs under this modulation scheme (second type). Quantitatively however, we observe

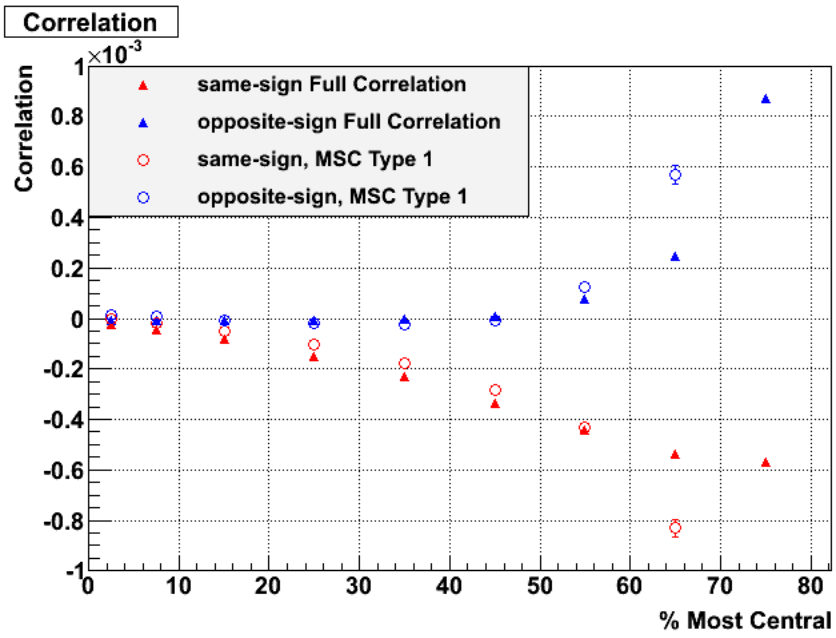

Figure 6.12: Full correlation function compared to modulated sign correlation (MSC) of the first type, $\langle M \rangle^2_{in-plane} = \langle M \rangle^2_{out-plane} = \left[\frac{2}{\pi}\right]^2$. "Full correlation" stands for the results of figure 6.6. MSC points not shown are out of scale. Statistical errors only.

that the opposite-sign MSCs are now much larger while the same-sign results changed marginally. The opposite-sign MSCs, therefore, are much more sensitive to elliptic flow than the same-sign MSCs.

It is surprising that the magnitude and shape of the main result in figure 6.6 can be reproduced so well within the scheme of just MSCs, i.e. $\langle S_a S_b M_a M_b \rangle \rightarrow \langle S_a S_b \rangle \langle M \rangle^2$. The basic agreement between the two is taken to imply that the main signal of figure 6.6 may equally well be analyzed within the scheme of MSCs. At this point in the analysis it is still possible that the signal of figure 6.6 is indeed caused by out-of-plane charge separation and therefore evidence for local parity violation of the strong interactions. We will test this possibility in

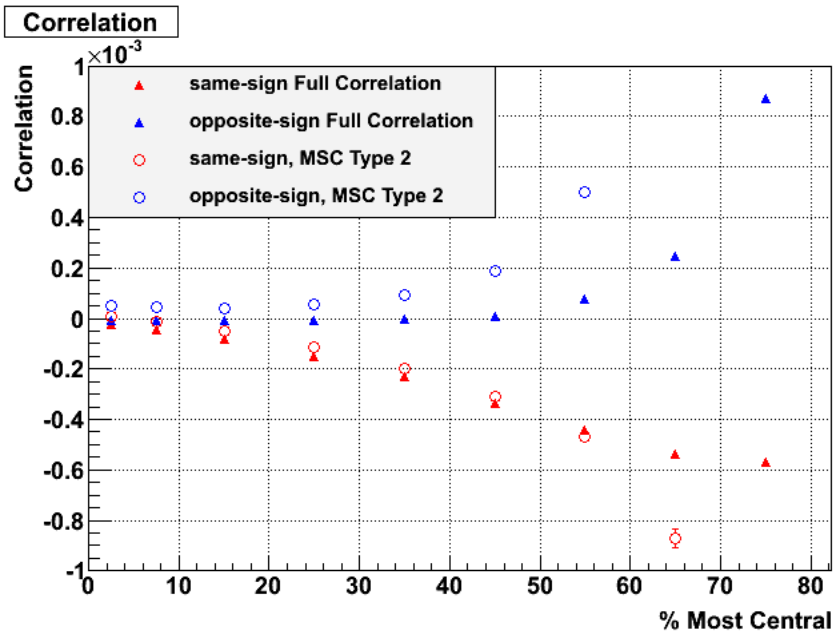

Figure 6.13: Full correlation function compared to modulated sign correlation (MSC) of the second type, $\langle M \rangle^2_{in-plane} > \frac{2}{\pi}^2$, $\langle M \rangle^2_{out-plane} < \frac{2}{\pi}^2$. "Full correlation" stands for the results of figure 6.6. MSC points not shown are out of scale. Statistical errors only.

the next section by simply counting units of charge separation in the events.

6.5.1 Correlation For Events With Zero Charge Separation

Units of out-of-plane charge separation and in-plane charge separation are respectively defined by

$$\Delta Q_{out} = |(N^T_+ - N^T_-) - (N^B_+ - N^B_-)| \quad (6.29)$$

$$\Delta Q_{in} = |(N^L_+ - N^L_-) - (N^R_+ - N^R_-)| \quad (6.30)$$

To state that figure 6.6 is solely caused by dynamical out-of-plane charge separation, it is a necessary condition that there be no signal over the subset of events with $\Delta Q_{out} = 0$. $\Delta Q_{out} = 0$ may be enforced in two ways: $(N^{T,B}_+ - N^{T,B}_-) = 0$,

or $(N_+^T - N_-^T) = (N_+^B - N_-^B)$. Here it is chosen to enforce it in the former way, $(N_+^{T,B} - N_-^{T,B}) = 0$ since it is the most transparent to handle statistically as we shall see shortly.

The full correlation function (Eq. 6.16) is a measure of in-plane correlations minus out-of-plane correlations. If those correlations come from charge separation ΔQ, then it is a measure of ΔQ_{in} correlations minus ΔQ_{out} correlations. In this light we must calculate the in-plane part of equation 6.26 in events with $\Delta Q_{in} = 0$ and the out-plane part in events with $\Delta Q_{out} = 0$ to be sure that the resulting correlations are not related to any type of charge separation.

It is shown in appendix C that this type of event-cut will introduce a trivial statistical bias to opposite-sign correlations but not same-sign correlations. In a purely statistical model with elliptic flow, the trivial opposite-sign "correlation" which is brought about from this event-cut is

$$\frac{\langle M \rangle^2_{in-plane} - \langle M \rangle^2_{out-plane}}{\langle N_+ \rangle} \tag{6.31}$$

As the statistical variances of the correlations in figure 6.6 are much much larger than the mean values it is expected that the simple subtraction of trivial correlations from observed correlations to be sufficient. The statistically corrected result of the MSCs of the second type over events with $\Delta Q = 0$ (zero charge separation) is shown in figure 6.14. Strikingly, we see the same qualitative signal in events with and without charge separation. It is also surprising that we see a much larger signal in peripheral collisions in events without charge separation. Although not visible from figure 6.14, for central and mid-central collisions we observe that the opposite-sign MSCs are negative for both event ensembles shown. However, this was also observed for the "Full" correlation of figure 6.6.

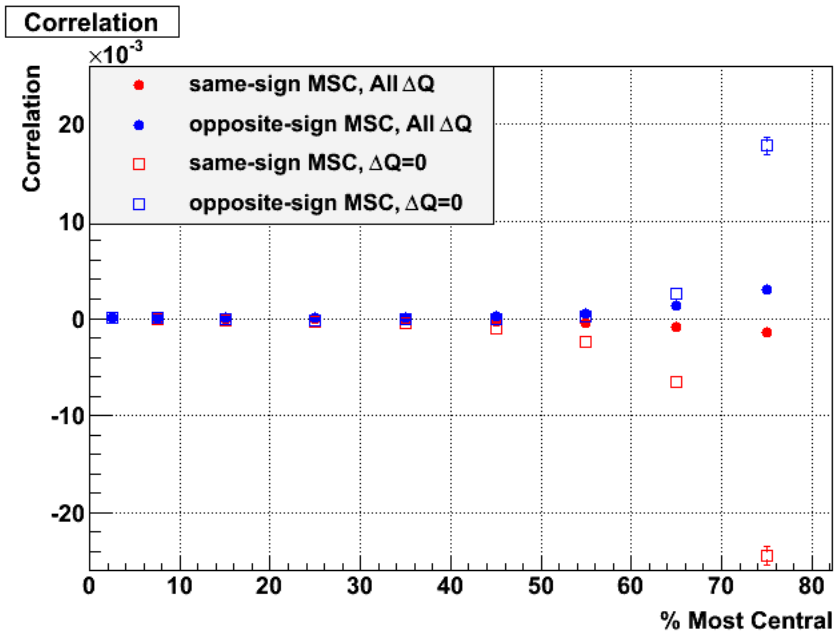

Figure 6.14: MSCs of the 2^{nd} type ($v_2 \neq 0$) over events with zero charge separation. Note the larger scale than before. Statistical errors only.

6.6 Discussion and Conclusions

The violation of parity in nature is a profoundly unintuitive concept. It implies that nature seemingly makes an arbitrary preference of handedness. Prior to 1956 parity conservation in all of physics was taken to be self-evident. Ample experimental evidence existed to demonstrate its conservation in strong and electromagnetic interactions but not for weak interactions. In 1956 Lee and Yang proposed that the then "$\theta - \tau$ puzzle" was solved by parity non-conservation in weak interactions [LY56]. They proposed that the θ particle was actually the same particle as the τ (now known as the charged Kaon) and that the weak decay of it sometimes violated parity by going into three pions and other times conserved parity by going into two pions.

In the same paper which resolved the "$\theta - \tau$ puzzle," Lee and Yang also

proposed an experiment to unequivocally prove the violation of parity in weak interactions. The experiment involved the observation of non-isotropic beta decays from a polarized Co-60 nucleus and was carried out later that year by C.S. Wu [Wu57]. Since then, many experiments have revealed parity violation of the weak interactions. The clearest indication of this is that in nature we only see left-handed neutrinos and no right-handed neutrinos.

The local violation of parity in **strong** interactions is allowed in the theory of QCD as well. Heavy-ion collisions at RHIC may *locally* violate parity in strong interactions through the axial anomaly of QCD. Whereas parity violation of the weak interactions was in the global sense, its violation in the strong interactions is only allowed in the local sense (microscopic domains). That is, in strong interactions we may violate parity in microscopic domains but integration over all domains yields no global preference in nature.

Local parity violation of the strong interactions can experimentally manifest itself as charge separation relative to the reaction plane driven by a very large magnetic field created in non-central collisions. A correlation function, $\langle\cos(\phi_a + \phi_b - 2\Psi_2)\rangle$, was shown to be directly sensitive to this effect and its measurements were presented in 200 GeV Au+Au collisions. The projection of the correlation against collision centrality is qualitatively in accord with theoretical predictions for dynamical out-of-plane charge separation. Moreover, physics processes in existing heavy-ion models which do not incorporate P-odd effects are unable to reproduce the signal seen in the real data. Cascades, although presenting an interesting possibility of undergoing the Chiral Magnetic Effect, are not observed to show the same signal due to statistical limitations. It is expected that with higher statistics a more conclusive statement can be said regarding cascades.

The correlation shown against $\langle\theta\rangle$ of the particle pairs was also presented. This revealed some inconsistencies with theoretical expectations. Sphaleron emission directs oppositely charged particles to be back-to-back which would result in the correlations being peaked at 90° or at least flat after multiple scattering takes place. What is found is that the opposite-sign correlations are neither peaked at 90° nor flat. Instead, the correlation peaks at each end of the theta range. One interpretation of this without invoking parity violation is that there exists an odd-number of charge neutral flowing clusters of particles in the events. It should be odd-numbered so that they only(1) or mostly(3,5...) appear on one side of the theta range per event. This process, if charge neutral, is completely orthogonal to the charge separation expected from the Chiral Magnetic Effect.

The correlation function was also studied in a simpler scheme where only modulated sign correlations across the event-plane were considered, MSCs. These correlations are still sensitive to the bulk observable of the Chiral Magnetic Effect. The signal remains much the same in this scheme. All of the features in the full correlation, which the heavy-ion models were not able to reproduce, are still present with MSCs. This is taken to imply that the observed signal also needs to be explained in this scheme just the same as it does in the full correlation scheme.

To finally assess whether the signal originates from events with non-zero units of charge separation, we did the inverse and calculated the MSCs over events with zero charge separation. If our signal was solely caused by dynamical out-of-plane charge separation then we should have seen a null result. A null result was not observed however. In fact, the signal became larger in magnitude. This appears to be evidence for a very significant P-even background which is larger in magnitude than a P-odd signal which may or may not exist. That is, $B_{cc} \neq B_{ss}$ in equations

6.17 and 6.18.

In light of the results obtained here, we do not see any convincing evidence for dynamical out-of-plane charge separation and local parity violation in the strong interactions at RHIC. The correlations shown in figure 6.6 do not appear to be solely or even mostly caused by dynamical out-of-plane charge separation.

We end on a hypothesis as to what else might be causing the signal. First note that for either $\langle \cos(\phi_a - \Psi_2) \cos(\phi_b - \Psi_2) \rangle$ or $\langle \sin(\phi_a - \Psi_2) \sin(\phi_b - \Psi_2) \rangle$, simple momentum conservation will force each to be negative ($N_{T,B}(N_{T,B}-1)-2N_T N_B < 0$ if $N_T = N_B = N/2$). For the same-sign correlations of figure 6.7 we do in fact see this. The reason why the cos()cos() part is larger in magnitude can be explained by elliptic flow. Elliptic flow will drive more particles in-plane where the cos()cos() is strongest. Therefore the momentum conservation correlations would be stronger there. This formalism is in principle also true for the opposite-sign correlations. However there we see positive and much stronger correlations. This cannot be explained by modulated momentum conservation. Charge neutral clusters can give positive correlations. They must also be flowing elliptically for the cos()cos() part to be larger than the sin()sin() part. To be consistent with figure 6.10 we must have an odd-number of these clusters typically occurring in an event, perhaps only 1. Summing this up, it is possible that the interplay of momentum conservation + particle clusters + v_2 could contribute significantly to the observed correlation shown in figure 6.6.

CHAPTER 7

Elliptic Flow

The geometrical source of elliptic flow, v_2, in heavy-ion collisions is the spatial eccentricity, ϵ, of the nuclear overlap region in the transverse plane. Through hydrodynamic rescattering this spatial eccentricity is converted into a momentum anisotropy over the evolution of the system. The underlying mechanisms for the conversion are the pressure gradients developed as a consequence of $\epsilon \neq 0$. The pressure vectors at the surface of region are generally pointed outward but greater in magnitude along the reaction plane. In principle this may translate into more particles emitted either along or out (squeeze-out) of the reaction plane. At RHIC energies, what is predominately found is a surplus of particles along the reaction plane and not the contrary, that is, positive v_2. Since the spatial eccentricity vanishes rapidly after the moment of the collision, any anisotropy resulting from it must reflect the physics which existed at the earliest moments of the collision.

This chapter presents measurements of v_2 for a variety of particles. Comparisons between these results and hydrodynamical calculations will also be presented. The degree of thermalization and deconfinement attained at RHIC will then be discussed.

7.1 The Event Plane Method

The most widespread method of measuring elliptic flow is the event plane method [PV98]. This method simply replaces the unobservable reaction plane angle with its approximated value: the event plane angle.

$$\Psi_m = \left(\tan^{-1} \frac{\sum_i w_i \sin(m\phi_i)}{\sum_i w_i \cos(m\phi_i)} \right) /m \tag{7.1}$$

The event plane angle is determined through the particle distributions themselves. Elliptic flow in this method is given by

$$v_2\{EP\} = \sum_i^N \cos 2(\phi_i - \Psi_m)/N \tag{7.2}$$

The sum goes over all particles of interest in all events: charged hadrons in a specific p_t bin, K_s^0's, etc. As mentioned in chapter 4, to achieve the greatest possible resolution on the flow harmonic under study, one should generally set the event plane harmonic equal to the flow harmonic. For elliptic flow, $\Psi_m \rightarrow \Psi_2$. Also, since the event plane is determined from the particles themselves, it is necessary to remove the particle corresponding to ϕ_i from the calculation of Ψ_m for each summed term in equation 7.2. This removes *auto-correlations*. Thus, we have a slightly different Ψ_m^i for each particle (ϕ_i) and equation 7.2 for m=2 should be rewritten as:

$$v_2\{EP\} = \sum_i^N \cos 2(\phi_i - \Psi_2^i)/N \tag{7.3}$$

The event plane method, while being very simple, suffers from all orders of non-flow contributions. That is, ϕ_i may be *directly* correlated to the particles constituting Ψ_2^i in the above equation. A technique of measuring v_2 with direct particle correlations removed is presented in the next section and is the technique used in this dissertation.

7.2 The Cumulant Method

Elliptic flow may be measured with many azimuthal correlation functions. The class of even-point (2,4,6,...) particle correlations used in v_2 cumulant analyses is given below in equation 7.4.

$$\left\langle e^{i2(\phi_1-\phi_2)}\right\rangle, \left\langle e^{i2(\phi_1+\phi_2-\phi_3-\phi_4)}\right\rangle, \left\langle e^{i2(\phi_1+\phi_2+\phi_3-\phi_4-\phi_5-\phi_6)}\right\rangle, ... \tag{7.4}$$

The averages are computed in 2 steps. First, one averages over all particles in an event to obtain an event average. Second, one averages the event averages over all events. The odd-point (1,3,5,...) particle correlations are given below in equation 7.5.

$$\left\langle e^{i2(\phi_1)}\right\rangle, \left\langle e^{i2(\pm\phi_1\mp\phi_2\mp\phi_3)}\right\rangle, \left\langle e^{i2(\pm\phi_1\pm\phi_2\mp\phi_3\mp\phi_4\mp\phi_5)}\right\rangle, ... \tag{7.5}$$

Unlike the even-point functions, all the odd-point functions vanish in the case of perfect azimuthal detector acceptance. In general, all the terms with an unequal amount of positive and negative signs in the above equations vanish in the case of perfect acceptance. Some even-point functions will also vanish for that reason, i.e. $\left\langle e^{i2(\phi_1+\phi_2)}\right\rangle$. The terms in equations 7.4 and 7.5 constitute the components of the cumulants.

To see their relation to elliptic flow, we consider the special case where the only correlations present are due to elliptic flow. In this case, the 2-particle correlation function may be rewritten as (considering the real parts only):

$$\left\langle e^{i2(\phi_1-\phi_2)}\right\rangle = \left\langle e^{i2(\phi_1-\Psi_r-\phi_2+\Psi_r)}\right\rangle = \left\langle e^{i2(\phi_1-\Psi_r)}\right\rangle \left\langle e^{-i2(\phi_2-\Psi_r)}\right\rangle = v_2^2 \tag{7.6}$$

Similarly, $\left\langle e^{i2(\phi_1+\phi_2-\phi_3-\phi_4)}\right\rangle = v_2^4$, and so on. The cumulants are constructed in the next two subsections.

7.2.1 Integrated Cumulant

The elliptic flow averaged over an entire range, such as p_t, is called the *integrated* elliptic flow. The integrated 2-particle cumulant is defined as [BDO01]:

$$\left\langle\left\langle e^{i2(\phi_1-\phi_2)}\right\rangle\right\rangle = \left\langle e^{i2(\phi_1-\phi_2)}\right\rangle - \left\langle e^{i2\phi_1}\right\rangle\left\langle e^{-i2\phi_2}\right\rangle \tag{7.7}$$

The double angle-brackets signify the cumulant. The 2-particle cumulant can be seen as the 2-particle correlations with 1-particle "correlations" (detector effects) subtracted off. The integrated v_2's relationship to the 2-particle cumulant may be seen from equation 7.6 and may be extracted with the following equation.

$$v_2 = \left\langle\left\langle e^{i2(\phi_1-\phi_2)}\right\rangle\right\rangle^{1/2} \tag{7.8}$$

This equation is only valid when the detectors acceptance is isotropic. STAR's acceptance is taken to be isotropic enough to use this equation. If a detectors acceptance is far from isotropic then the 2-particle cumulant is no longer purely a function of v_2 but also a function of v_1; a mixture of harmonics.

The integrated 4-particle cumulant for the case of perfect acceptance is defined as:

$$\begin{aligned}\left\langle\left\langle e^{i2(\phi_1+\phi_2-\phi_3-\phi_4)}\right\rangle\right\rangle &= \left\langle e^{i2(\phi_1+\phi_2-\phi_3-\phi_4)}\right\rangle \\ - \left\langle e^{i2(\phi_1-\phi_3)}\right\rangle\left\langle e^{i2(\phi_2-\phi_4)}\right\rangle &- \left\langle e^{i2(\phi_1-\phi_4)}\right\rangle\left\langle e^{i2(\phi_2-\phi_3)}\right\rangle\end{aligned} \tag{7.9}$$

The 4-particle cumulant can be understood as a 4-particle correlation with 2-particle correlations subtracted off. The subtraction removes "direct" correlations between particles 1 and 3, 2 and 4, 1 and 4, 2 and 3. Here "direct" correlations represent correlations not related to the reaction-plane. For instance, two daughters from a resonance decay are directly correlated through their opening angle. Thus, the 4-particle cumulant is not susceptible to 2-particle non-flow. That is

its virtue and advantage over the event plane method of the preceding section. In general, for an even integer n, the n-particle cumulant removes all *direct* n-2 particle correlations. However, statistical uncertainties get larger and larger with higher order cumulants.

Since particles 1-4 all come from the same pool of particles, equation 7.9 may be symmetrized:

$$\left\langle\left\langle e^{i2(\phi_1+\phi_2-\phi_3-\phi_4)}\right\rangle\right\rangle = \left\langle e^{i2(\phi_1+\phi_2-\phi_3-\phi_4)}\right\rangle - 2\left\langle e^{i2(\phi_1-\phi_3)}\right\rangle^2 \tag{7.10}$$

The 4-particle cumulant is related to v_2 through the following equation:

$$\left\langle\left\langle e^{i2(\phi_1+\phi_2-\phi_3-\phi_4)}\right\rangle\right\rangle = v_2^4 - 2(v_2^2)^2 = -v_2^4 \tag{7.11}$$

This relation is only valid for the case of isotropic acceptance. STAR's acceptance is taken to be isotropic enough to use this relation. The 4-particle cumulant expression itself must also be modified to account for imperfect acceptance. The full 4-particle cumulant for imperfect acceptance is given below (real parts only).

$$\begin{aligned}
\left\langle\left\langle e^{i2(\phi_1+\phi_2-\phi_3-\phi_4)}\right\rangle\right\rangle &= \left\langle e^{i2(\phi_1+\phi_2-\phi_3-\phi_4)}\right\rangle \\
&- 2\left\langle e^{i2(\phi_1-\phi_3)}\right\rangle\left\langle e^{i2(\phi_2-\phi_4)}\right\rangle \\
&- \left\langle e^{i2\phi_1}\right\rangle\left\langle e^{i2(\phi_2-\phi_3-\phi_4)}\right\rangle \\
&- \left\langle e^{i2\phi_2}\right\rangle\left\langle e^{i2(\phi_1-\phi_3-\phi_4)}\right\rangle \\
&- 2\left\langle e^{-i2\phi_3}\right\rangle\left\langle e^{i2(\phi_1+\phi_2-\phi_4)}\right\rangle \\
&- \left\langle e^{i2(\phi_1+\phi_2)}\right\rangle\left\langle e^{-i2(\phi_3+\phi_4)}\right\rangle \\
&+ 4\left\langle e^{i2\phi_1}\right\rangle\left\langle e^{-i2\phi_3}\right\rangle\left\langle e^{i2(\phi_2-\phi_4)}\right\rangle \\
&+ 4\left\langle e^{i2\phi_2}\right\rangle\left\langle e^{-i2\phi_3}\right\rangle\left\langle e^{i2(\phi_1-\phi_4)}\right\rangle \\
&+ 2\left\langle e^{i2\phi_1}\right\rangle\left\langle e^{i2\phi_2}\right\rangle\left\langle e^{-i2(\phi_3+\phi_4)}\right\rangle \\
&+ 2\left\langle e^{-i2\phi_3}\right\rangle\left\langle e^{-i2\phi_4}\right\rangle\left\langle e^{i2(\phi_1+\phi_2)}\right\rangle \\
&- 6\left\langle e^{i2\phi_1}\right\rangle\left\langle e^{i2\phi_2}\right\rangle\left\langle e^{-i2\phi_3}\right\rangle\left\langle e^{-i2\phi_4}\right\rangle
\end{aligned} \tag{7.12}$$

This expression is general and may be used even for detectors with poor azimuthal acceptance as it naturally subtracts out "correlations" induced by a detector. The general idea is to subtract off all possible ways of factoring the 4-particle term. The coefficients for any given term may be derived by summing up the number of different ways the terms above it may be factored to yield that term (start from the 2^{nd} term and work your way down). Equation 7.12 is symmetrized in the case that particles 2-4 come from the same particle pool. It may be further symmetrized if particle 1 comes from that same pool. Particle 1 is left distinct for equation 7.12 to be useful in the next subsection. The full 4-particle cumulant expression of equation 7.12 is the form which is used for all $v_2\{4\}$ measurements shown in this dissertation.

7.2.2 Differential Cumulant

The elliptic flow averaged over particles within a narrow range–of p_t for instance– is called the *differential* elliptic flow. The differential 2-particle cumulant is simply equation 7.7 with the first particle drawing from the differential pool of particles and the second particle drawing from outside of that pool. That is, the differential 2-particle cumulant is formed by replacing ϕ_1 with Φ (particles from the differential pool):

$$\left\langle\left\langle e^{i2(\Phi-\phi_2)}\right\rangle\right\rangle = \left\langle e^{i2(\Phi-\phi_2)}\right\rangle - \left\langle e^{i2\Phi}\right\rangle\left\langle e^{-i2\phi_2}\right\rangle \tag{7.13}$$

To see how the differential 2-particle cumulant is related to elliptic flow, we use the same technique that went into equation 7.6.

$$\left\langle\left\langle e^{i2(\Phi-\phi_2)}\right\rangle\right\rangle = v_2' v_2 \tag{7.14}$$

where v_2' and v_2 is the elliptic flow coming from particle Φ and ϕ, respectively. Likewise, the full 4-particle differential cumulant is given by equation 7.12 with

ϕ_1 replaced by Φ. It's relationship to elliptic flow is given below.

$$\left\langle\left\langle e^{i2(\Phi+\phi_2-\phi_3-\phi_4)}\right\rangle\right\rangle = v_2' v_2^3 - 2(v_2' v_2)(v_2^2) = -v_2' v_2^3 \tag{7.15}$$

Again, this relationship will be modified if a detector's acceptance is poor. Given the relations in equation 7.15 and 7.11, we can now extract the 4-particle cumulant differential elliptic flow, $v_2'\{4\} \equiv v_2'$.

$$v_2'\{4\} \equiv v_2' = \frac{-\left\langle\left\langle e^{i2(\Phi+\phi_2-\phi_3-\phi_4)}\right\rangle\right\rangle}{(-\left\langle\left\langle e^{i2(\phi_1+\phi_2-\phi_3-\phi_4)}\right\rangle\right\rangle)^{3/4}} \tag{7.16}$$

It should be stressed again that the particle pool from which Φ draws from is orthogonal to the particle pool from which ϕ draws from. That is, if Φ is a charged hadron with $1.2 < p_t < 1.4$ GeV/c, then ϕ is all other charged hadrons outside of that p_t range. Therefore, the differential as well as the integrated cumulant is unique for every single differential bin!

7.2.3 Cumulant Weights

Two types of weights are applied to each of the averages in equation 7.12. The first, W_1 is a p_t weight formed from the product of the p_t's of all particles. This is designed to improve the accuracy of a flow measurement as particles with higher p_t have greater flow. The second, W_2 is an N_{poi} (particle of interest) weight. This is designed to enhance the contribution from events with more particles of interest, i.e. charged hadrons within a narrow p_t range. The weights are mathematically shown below.

$$\begin{aligned} W_{total} &= W_1 W_2 \\ W_1 &= \prod_{i}^{N_{points}} w_{p_t,i} \\ W_2 &= N_{poi} \end{aligned} \tag{7.17}$$

$$w_{p_t,i} = \begin{cases} p_{t,i} & \text{if } p_{t,i} < 2 \\ 2 & \text{otherwise} \end{cases}$$

N_{points} is the number points in the particular average (1,2,3 or 4). A saturation cut-off is also applied to the p_t weights. This is inspired by the experimentally observed saturation of v_2 versus p_t for $p_t > 2$ GeV/c. Both integrated and differential cumulants are weighted exactly the same.

7.2.4 Practicality: Evaluating a 4-particle Loop with 2-particle Loops

The first term to evaluate in equation 7.12 is a 4-particle correlation, $\left\langle e^{i2(\phi_1+\phi_2-\phi_3-\phi_4)} \right\rangle$. Practically speaking, it is unfeasible to use a nested 4-loop to compute it (too much cpu time). To evaluate it, one can use a simple math trick.

$$\left\langle e^{i2(\phi_1+\phi_2-\phi_3-\phi_4)} \right\rangle = \frac{(\sum e^{i2(\phi_i-\phi_j)})(\sum e^{i2(\phi_k-\phi_l)}) - degeneracies}{N(N-1)(N-2)(N-3)} \tag{7.18}$$

The term, degeneracies, represents all instances where particle i = particle k or l and all instances where particle j = particle k or l in the product of sums, $(\sum e^{i2(\phi_i-\phi_j)})(\sum e^{i2(\phi_k-\phi_l)})$. There will be $(N(N-1))^2 - N(N-1)(N-2)(N-3)$ degenerate terms. For the case where particles 1-4 all come from the same pool (integrated flow case) they are given by:

$$\begin{aligned} degeneracies &= \sum \left(e^{i2(\phi_i-\phi_j)}\right)^2 \\ &+ 2\left(\sum e^{i2(\phi_i-\phi_j)} e^{i2(\phi_i-\phi_k)}\right) \\ &+ 2\left(\sum e^{i2(\phi_i-\phi_j)} e^{i2(\phi_k-\phi_i)}\right) \end{aligned} \tag{7.19}$$

The evaluation of the last two terms in equation 7.19 requires a nested 3-particle loop, which is still too time consuming. The same trick is applied to each of these

terms. For instance:

$$\begin{aligned}\left(\sum e^{i2(\phi_i-\phi_j)}e^{i2(\phi_i-\phi_k)}\right) &= \left(\sum e^{i2(2\phi_i-\phi_j)}e^{-i2\phi_k}\right) \\ &= \left(\sum e^{i2(2\phi_i-\phi_j)}\right)\left(\sum e^{-i2\phi_i}\right) \\ &- \left(\sum e^{i4(\phi_i-\phi_j)}\right) \\ &- \left(\sum e^{i2(\phi_i-\phi_j)}\right) \end{aligned} \tag{7.20}$$

7.3 Results: Charged Hadron v_2

The 2-particle and 4-particle cumulant elliptic flow versus p_t averaged over all charged hadrons directly seen in the TPC ($p^{\pm}$, $\pi^{\pm}$, $K^{\pm}$) is shown in the upper part of figure 7.1. 18.5 M minimum bias events from STAR's 2007 AuAu 200GeV run were used. Only mid-central collisions are used, 10-40%. Error bars represent statistical uncertainties only. For both cumulants, v_2 is observed to first rise with p_t until a saturation point is reached at around 3 GeV/c. The difference between $v_2\{2\}$ and $v_2\{4\}$ illustrates the effect of direct 2-particle correlations (2-particle non-flow). As already mentioned, $v_2\{2\}$ is susceptible to 2-particle non-flow while $v_2\{4\}$ is not. The percentage of 2-particle non-flow in $v_2\{2\}$ is estimated in the lower part of figure 7.1. This may be regarded as the systematic error of $v_2\{2\}$, $\delta v_2\{2\}$. The systematic error for $v_2\{4\}$ should be on the order of $(\delta v_2\{2\})^3$ [BDO01] which is much smaller. We see that the percentage versus p_t is mostly flat. At high p_t we see a slight rise in the percentage which might be caused by jet correlations as jet related hard processes dominate the high p_t region. The larger statistical error bars for the higher order cumulants are generally to be expected as the percentage contribution from flow to order-n particle correlations decreases with n.

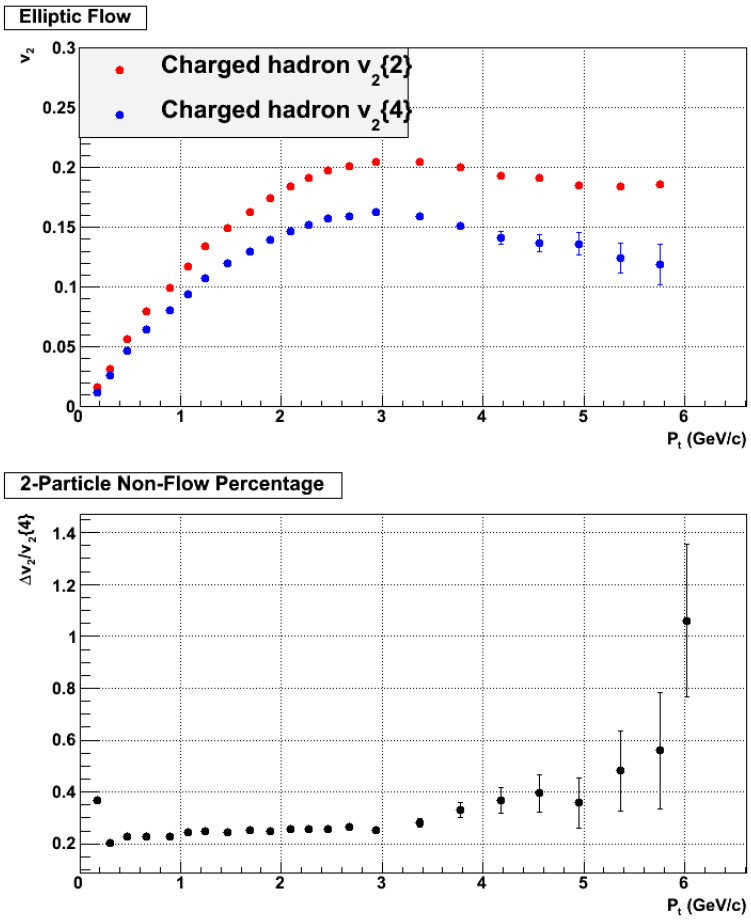

Figure 7.1: Top figure: $v_2\{2\}$ and $v_2\{4\}$ versus p_t averaged over all charged hadrons in the TPC. Bottom figure: $(v_2\{2\} - v_2\{4\})/v_2\{4\}$ versus p_t. 10-40% centrality.

7.4 Results: Pion, Kaon, and Proton v_2

Charged pions, kaons, and protons can be identified in the TPC at low momentum. Particle identification is done with a 2-sigma cut on the particle's dE/dx deviation from its respective mean value: for particle i, $|\sigma_i| < 2$. Furthermore, we require that the particle is 2-sigma away from both of the other two particle's bands: for particle $j \neq i$, $|\sigma_{j\neq i}| > 2$. $v_2\{2\}$ and $v_2\{4\}$ versus p_t for pions,

kaons, and protons in 4 different centrality bins are shown in figures 7.2 and 7.3. Data-set details are the same as those for the charged hadron results.

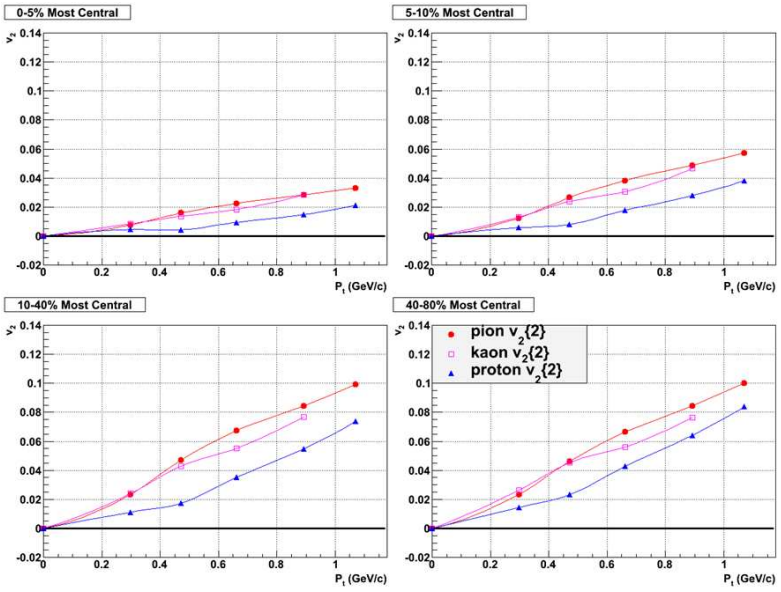

Figure 7.2: $v_2\{2\}$ for pions($\pi^- + \pi^+$), kaons($k^- + k^+$), and protons(p^+).

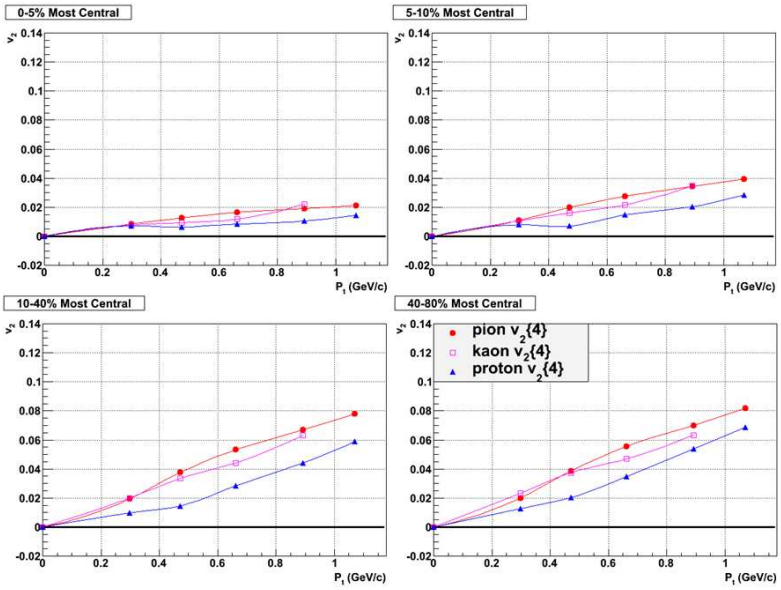

Figure 7.3: $v_2\{4\}$ for pions($\pi^- + \pi^+$), kaons($k^- + k^+$), and protons(p^+).

Several features of figures 7.2 and 7.3 are to be pointed out. Firstly, for both cumulant types and for every centrality bin we see a mass ordering of elliptic flow over the covered p_t region: particles of higher mass have a smaller v_2. Only the lowest p_t data-point for kaons appears to violate this. Secondly, in the most central collisions we observe the smallest magnitude of v_2. This is largely due to the smaller initial geometrical eccentricities in central collisions. Thirdly, we see that $v_2\{4\}$ retains the same basic functional shape as $v_2\{2\}$ and that $v_2\{4\}$ is smaller in magnitude everywhere. Although not shown, anti-proton and proton v_2 are observed to be consistent with each other except at low-pt ($p_t < .6$) where anti-proton v_2 is observed to be slightly smaller.

7.5 Results: $K^0_s, \Lambda, \Xi^{\pm}, v_2$

Elliptic flow measurements of topologically reconstructed particles must be done in two parts. First, one must measure v_2 from particle candidates within a certain invariant mass range of the particle's mass peak. This will contain contributions from both true particle candidates and false candidates. Second, one must measure v_2 from false particle candidates only to form a background v_2 measurement. The two terms are then subtracted from each other with proportions determined by the signal to background ratio. This algorithm is mathematically described by:

$$\begin{aligned} v_2^{Sig+Bkg} &= \frac{Sig}{Sig+Bkg} v_2^{Sig} + \frac{Bkg}{Sig+Bkg} v_2^{Bkg} \\ v_2^{Sig} &= \alpha v_2^{Sig+Bkg} - (\alpha - 1)\, v_2^{Bkg} \\ \alpha &= \frac{Sig+Bkg}{Sig} \end{aligned} \tag{7.21}$$

Here, the background v_2 is taken from a narrow range on either side of the particle's mass peak. The signal+background v_2 is taken from a 3σ mass window

around the peak. This is illustrated with figure 7.4. The blue(darkest) region

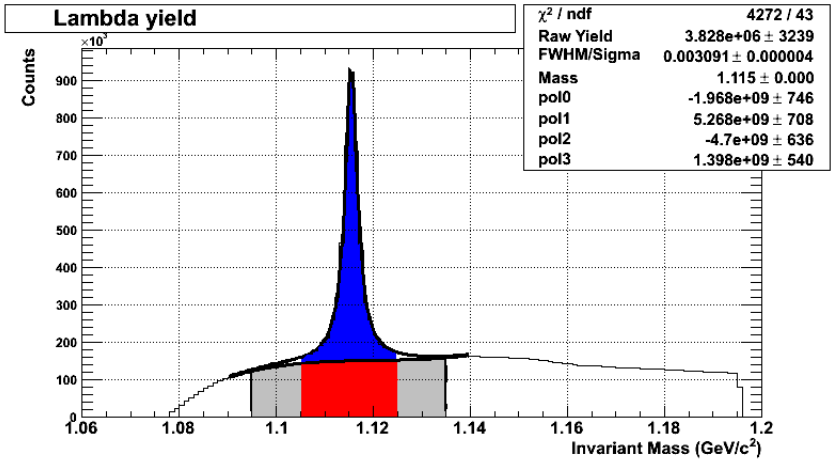

Figure 7.4: Signal and Background regions for the case of Lambdas from 0-80% centrality.

denotes the true candidates which are indistinguishable from the false candidates directly underneath. Together, the true + false candidate region form the signal+background region. The gray(lightest) regions on either side denote the background region. This extraction technique assumes that the background v_2 functional form does not change rapidly a function of invariant mass.

$v_2\{2\}$ results for K^0_s, Λ and $\Xi^{\pm}$ are shown in figure 7.5. Data set details are the same as those for the charged hadron results. Reconstruction of these particles is done with the cuts outlined in chapter 5. Error bars are statistical only. Two features are to be pointed out. One, there appears to be different saturation levels at high p_t for baryons and mesons. Two, there appears to be a mass-ordering at low p_t with heavier particles having smaller v_2.

$v_2\{4\}$ results for K^0_s, Λ and $\Xi^{\pm}$ are shown in figure 7.6. Quantitatively, one observes a smaller elliptic flow with the 4-particle approach. Qualitatively, one again observes the same two features: differing baryon/meson saturation levels

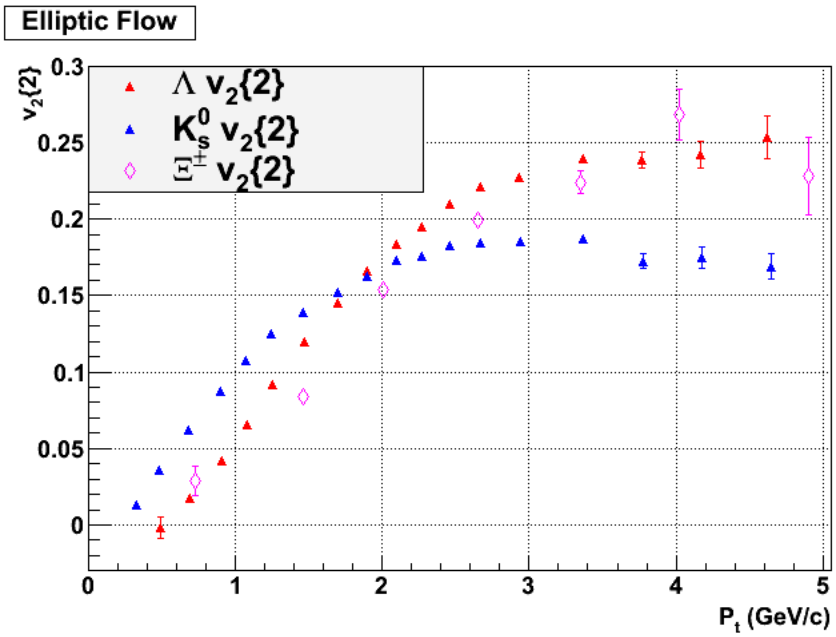

Figure 7.5: $v_2\{2\}$ results for K^0_s, Λ and $\Xi^{\pm}$. $10-40\%$ centrality.

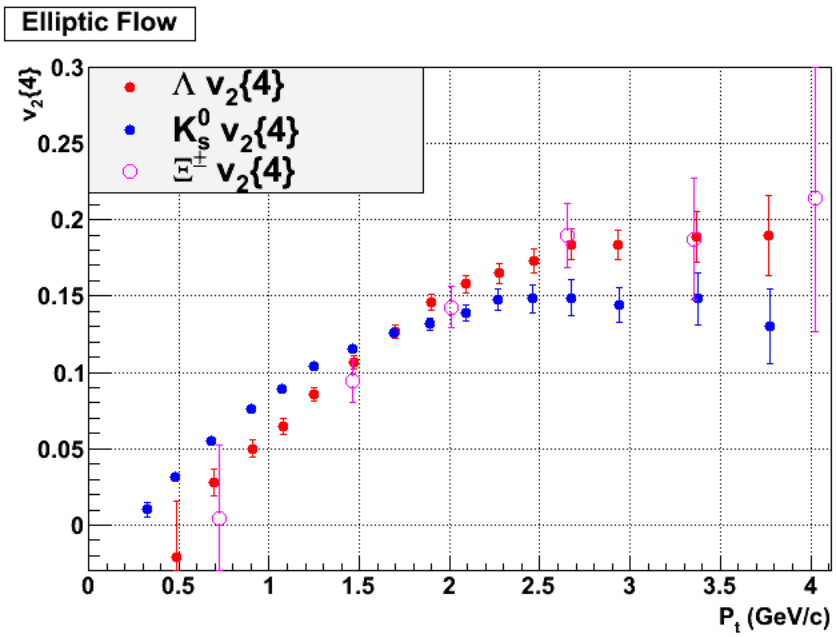

Figure 7.6: $v_2\{4\}$ results for K^0_s, Λ and $\Xi^{\pm}$. $10-40\%$ centrality.

and mass-ordering at low p_t. Thus, we may safely conclude that these two features are not caused by 2-particle non-flow which is a major source of systematic uncertainties in the more commonly used event plane method of flow analyses.

7.6 Discussion and Conclusions

Elliptic flow is a very useful tool in the understanding of early time dynamics in heavy-ion collisions. Multi-particle cumulants can be used to measure elliptic flow and typically have been calculated using an indirect method of generating functions [BDO01]. Here, a method for evaluating them directly using multi-particle correlations was presented.

One of the most striking features observed at STAR is the grouping of all baryon v_2 different from all meson v_2 at high p_t ($p_t > 2.5$ GeV/c) [Abe08a]. Figure 7.6 shows for the first time that the same feature appears to persist with $v_2\{4\}$ and is therefore not caused by 2-particle non-flow. This observed feature is most commonly explained through the coalescence model of hadron formation. In this model, the relevant degrees of freedom are not partons but massive (dressed) valence quarks [MV03]. Hadrons form via the coalescence of quarks such that the invariant spectra of hadrons is proportional to the *product* of invariant constituent-quark spectra.

$$\begin{aligned} \frac{dN_B}{d^2p_t}\left(\vec{p_t}\right) &= C_B\left(p_t\right)\left[\frac{dN_q}{d^2p_t}\left(\frac{\vec{p_t}}{3}\right)\right]^3 \\ \frac{dN_M}{d^2p_t}\left(\vec{p_t}\right) &= C_M\left(p_t\right)\left[\frac{dN_q}{d^2p_t}\left(\frac{\vec{p_t}}{2}\right)\right]^2 \end{aligned} \tag{7.22}$$

The subscripts M, B, and q represent mesons, baryons, and quarks, respectively. C_B and C_M are the probabilities for qqq →baryon and $q\bar{q}$ →meson coalescence. The elliptic flow of baryons and mesons is then inherited from the elliptic flow of their constituent quarks. If the constituent quarks have only elliptical anisotropy,

its spectrum is given by

$$\frac{dN_q}{p_t dp_t d\Phi} = \left(\frac{1}{2\pi}\right) \frac{dN_q}{p_t dp_t} \left[1 + 2v_{2,q} \cos\left(2\Phi\right)\right] \tag{7.23}$$

where Φ is the azimuthal angle of the quark relative to the reaction plane. Inserting equation 7.23 into 7.22 and averaging over $\cos\left(2\Phi\right)$ one obtains:

$$\begin{aligned} v_{2,B}\left(p_t\right) &= \frac{3v_{2,q}\left(p_t/3\right) + 3v_{2,q}^3\left(p_t/3\right)}{1 + 6v_{2,q}^2\left(p_t/3\right)} \\ v_{2,M}\left(p_t\right) &= \frac{2v_{2,q}\left(p_t/2\right)}{1 + 2v_{2,q}^2\left(p_t/2\right)} \end{aligned} \tag{7.24}$$

In the case of small v_2, these equations reduce to

$$\begin{aligned} v_{2,B}\left(p_t\right) &= 3v_{2,q}\left(p_t/3\right) \\ v_{2,M}\left(p_t\right) &= 2v_{2,q}\left(p_t/2\right) \end{aligned} \tag{7.25}$$

The validity of a coalescence model is questionable when the constituent phase-space density is very large (low p_t) and when p_t is very large (high p_t). For very large phase-space densities, hadronization can occur with very large relative momenta (ignored in equation 7.22). For high p_t, the fragmentation process of hadronization dominates over coalescence. Nonetheless, we may rescale the entire x and y axes of figures 7.5 and 7.6 by a factor of 2 for K_s^0 and a factor of 3 for Λ and $\Xi^{\pm}$. Figure 7.7 and 7.8 shows this rescaling done for $v_2\{2\}$ and $v_2\{4\}$, respectively. While the N_{CQ} scaling is not perfect, all three particles tend to generally follow the same trend for both cumulant types. This is the first time N_{CQ} scaling has been observed in 4-particle cumulants. An observation of N_{CQ} scaling implies that quarks are the underlying degrees of freedom in the matter created in 200 GeV AuAu collisions at RHIC. Furthermore, it implies that these quarks have a collective elliptic flow and that quark deconfinement is achieved at RHIC.

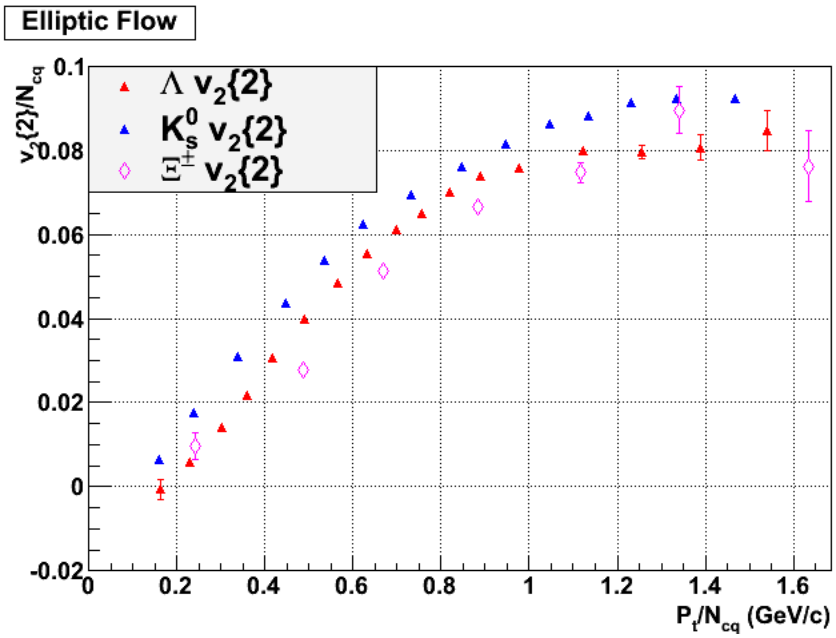

Figure 7.7: $v_2\{2\}/N_{CQ}$ versus p_t/N_{CQ} for K^0_s, Λ and $\Xi^{\pm}$

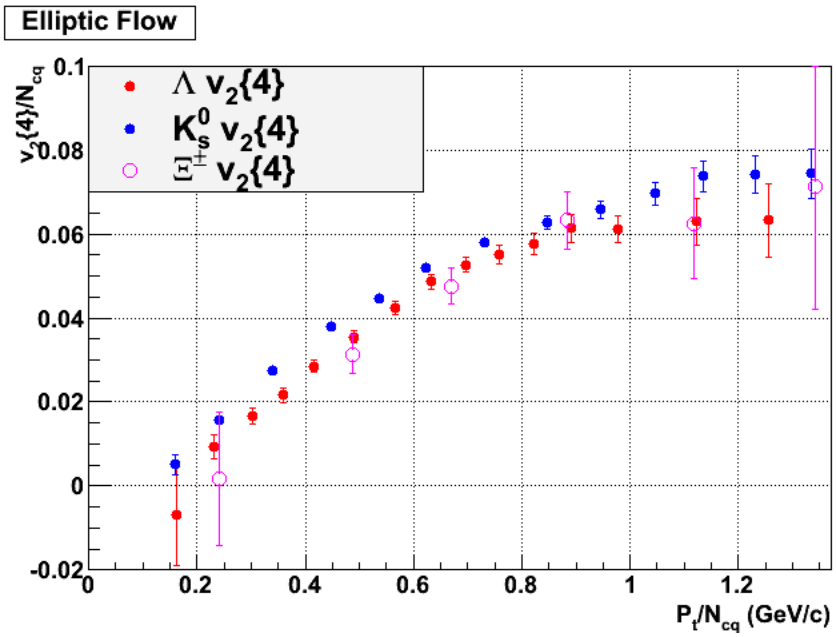

Figure 7.8: $v_2\{4\}/N_{CQ}$ versus p_t/N_{CQ} for K^0_s, Λ and $\Xi^{\pm}$

The coalescence model has also been applied to the invariant p_t spectrum of multi-strange hadrons to extract the quark p_t spectrum in a QGP phase [Che08]. Assuming that all hadrons are produced via the coalescence of quarks, one first scales the x and y axes of the p_t spectra of Ξ(ssd), Ω(sss), and ϕ(ss) by N_{CQ}. Second, one takes the ratio of Ω to ϕ and Ξ to ϕ to obtain the s and d quark spectra, respectively. This revealed that s quarks had a significantly flatter spectrum than d quarks which is consistent with hydrodynamics in a deconfined phase.

The $v_2\{4\}$ results for $\pi^{\pm}$, $p^{\pm}$, K^0_s, Λ, and Ξ are now compared to hydrodynamical models. Hydrodynamics data come from Pasi Huovinen [Huo05]. Only the 4-particle cumulant results are included in this comparison as they are a more accurate measure of v_2. The type of hydrodynamics considered here is that of a equilibrated liquid where thermodynamics applies. Three hydrodynamical models are considered here. Hydrodynamics data come from private communications with Pasi Huovinen [Huo05]. All are based on a so-called "2+1" dimensional approach whose equations are simpler to solve analytically than the full "3+1" approach. That is, calculations are done in 2 spatial dimensions (transverse plane) + time with the added assumption of longitudinal boost invariance. Viscous effects are not included in these models.

The first treats the matter in the collision region merely as a gas of hadrons and resonances, a hadron resonance gas (**HRG**) [Huo05]. It has been shown that an interacting hadron gas phase can be well approximated by a non-interacting hadron gas with the inclusion of free resonances [Huo05]. No QGP phase transition is included in the HRG model. The equation of state (EoS) is one of a "bag-model."

The second treats the matter in the collision region as a "soup" of quarks and gluons (**Q**). A 1^{st} order QGP phase transition at T=170 MeV is included in the

Q model. Chemical equilibrium is also assumed throughout the entire evolution up until kinetic freeze-out.

The third contains a lattice QCD inspired EoS (**s95p-PCE**). A smooth cross-over to a QGP phase is included. The entropy density is constrained to be 95% of the Stefan-Boltzmann limit at T=800 MeV. Partial chemical equilibrium is allowed.

Pion and proton $v_2\{4\}$ is compared to all three hydrodynamical models in figures 7.9 and 7.10, respectively. K^0_S, Λ, and Ξ are compared to all three hydrodynamical models in figures 7.11, 7.12, and 7.13, respectively.

It is observed that none of the three hydro models can completely describe the data. Of the three, EoS Q best describes the data at low p_t. All models diverge largely from data at high p_t ($p_t > 2$ GeV/c) indicating that ideal hydrodynamics may no longer be valid after a certain point in p_t. The presence of viscosity (non-ideal) could change this interpretation greatly. The models used here do not include viscous effects. The inclusion of viscosity in hydrodynamics tends to suppress the development of elliptic flow as it reduces the number of scattering events a particle may undergo in the medium created in heavy-ion collisions. Currently, it is not well understood how to unambiguously treat viscosity in hydrodynamic calculations and so comparisons to viscous hydro cannot be made at this moment.

Still, the agreement between the data and the EoS Q hydrodynamical model seems to suggest that some amount of bulk-collectivity (thermalization) is established for low-p_t particles in 200 GeV AuAu collisions at RHIC. It is difficult to tell exactly how much thermalization is actually attained since viscous corrections will also drive v_2 to the smaller values observed here. What is clear however is that past RHIC v_2 measurements based on 2-particle methods (similar to 2-

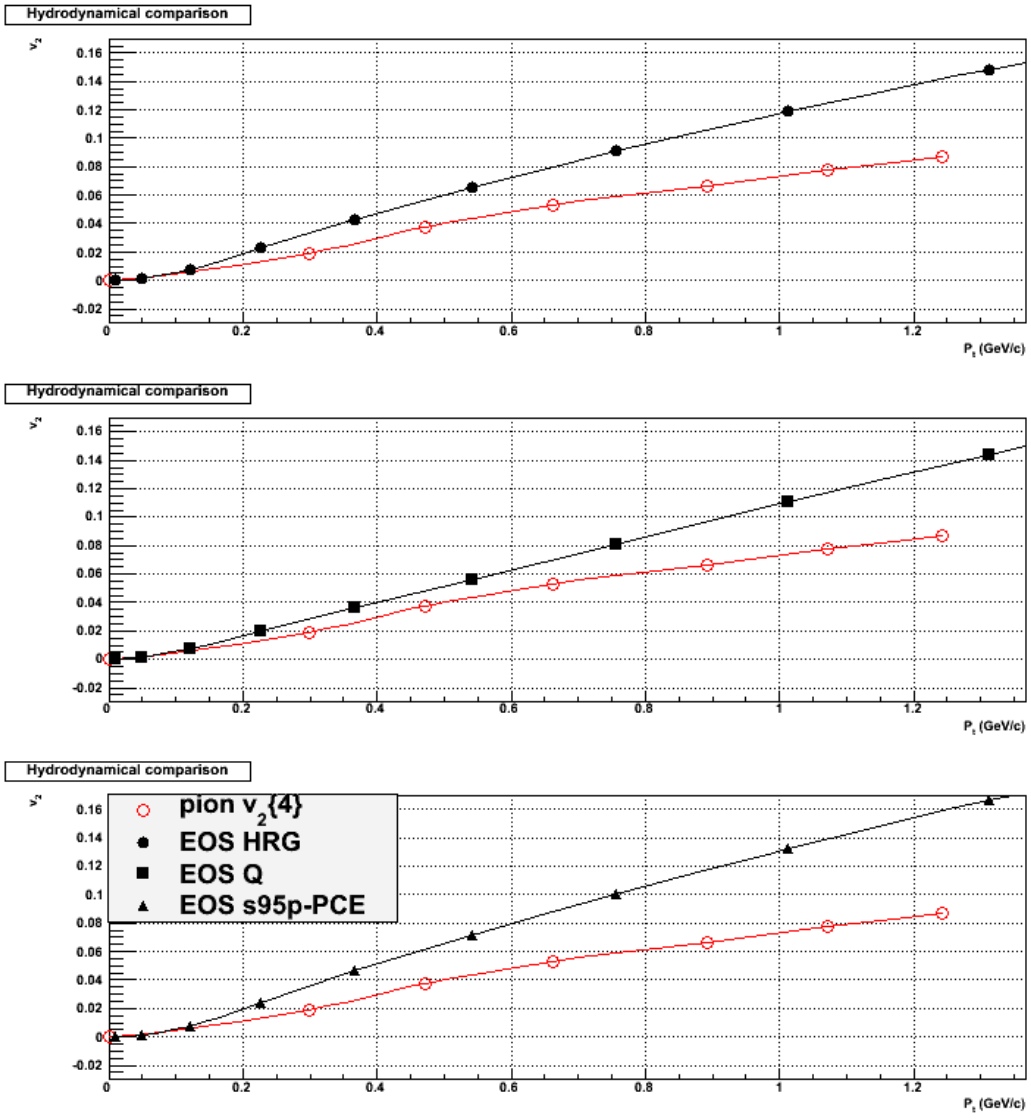

Figure 7.9: $\pi^{\pm}$ $v_2\{4\}$ compared to three hydrodynamical models. Real data are shown by red hollow circles. $10-40\%$ centrality.

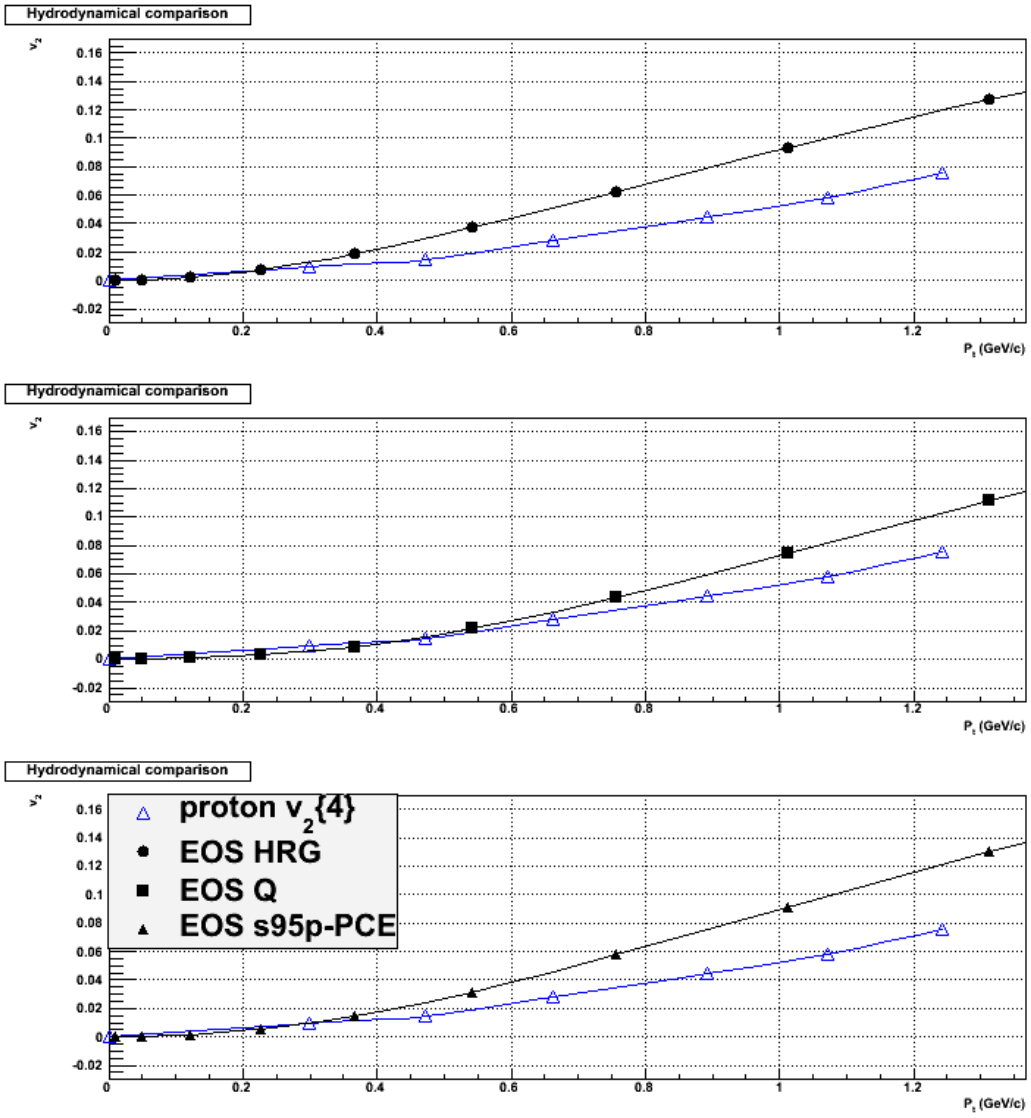

Figure 7.10: p^+ $v_2\{4\}$ compared to three hydrodynamical models. Real data are shown by blue hollow triangles. $10-40\%$ centrality.

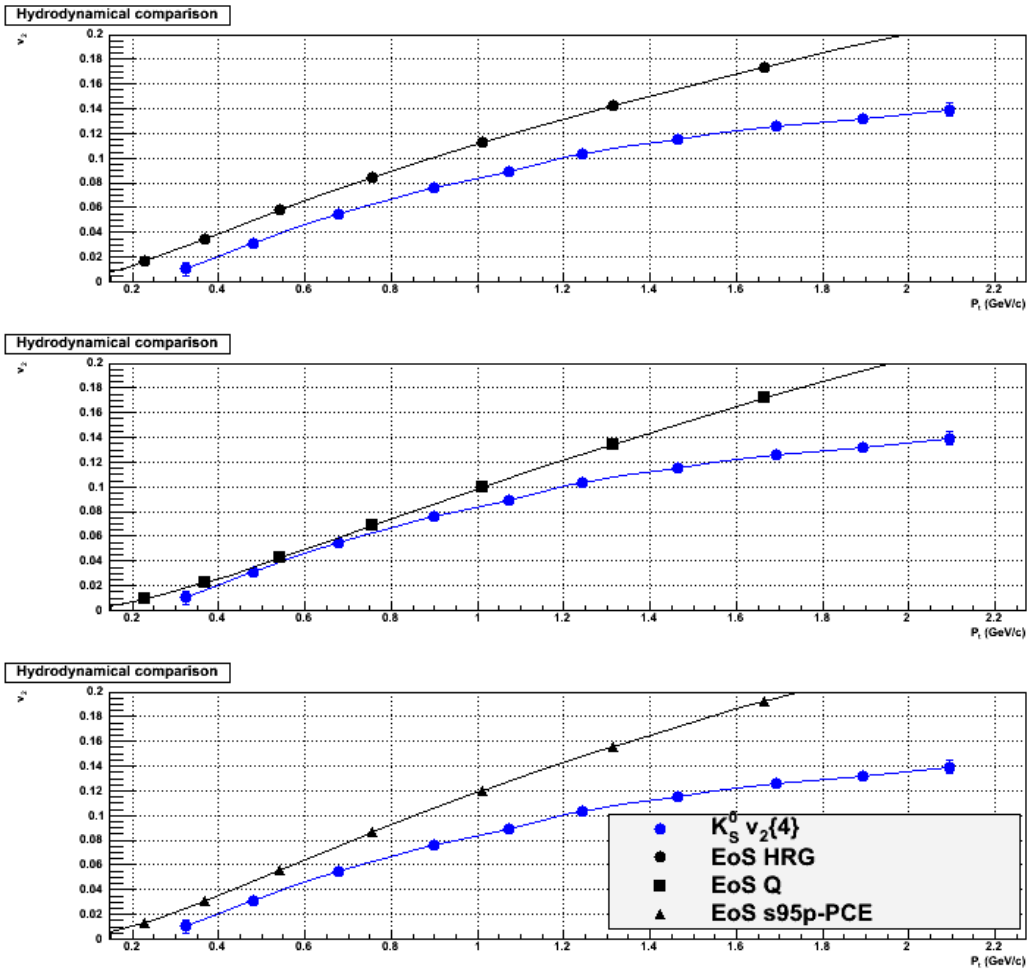

Figure 7.11: K^0_s versus p_t data versus hydrodynamical model comparison. Real data are shown by solid blue circles. $10 - 40\%$ centrality.

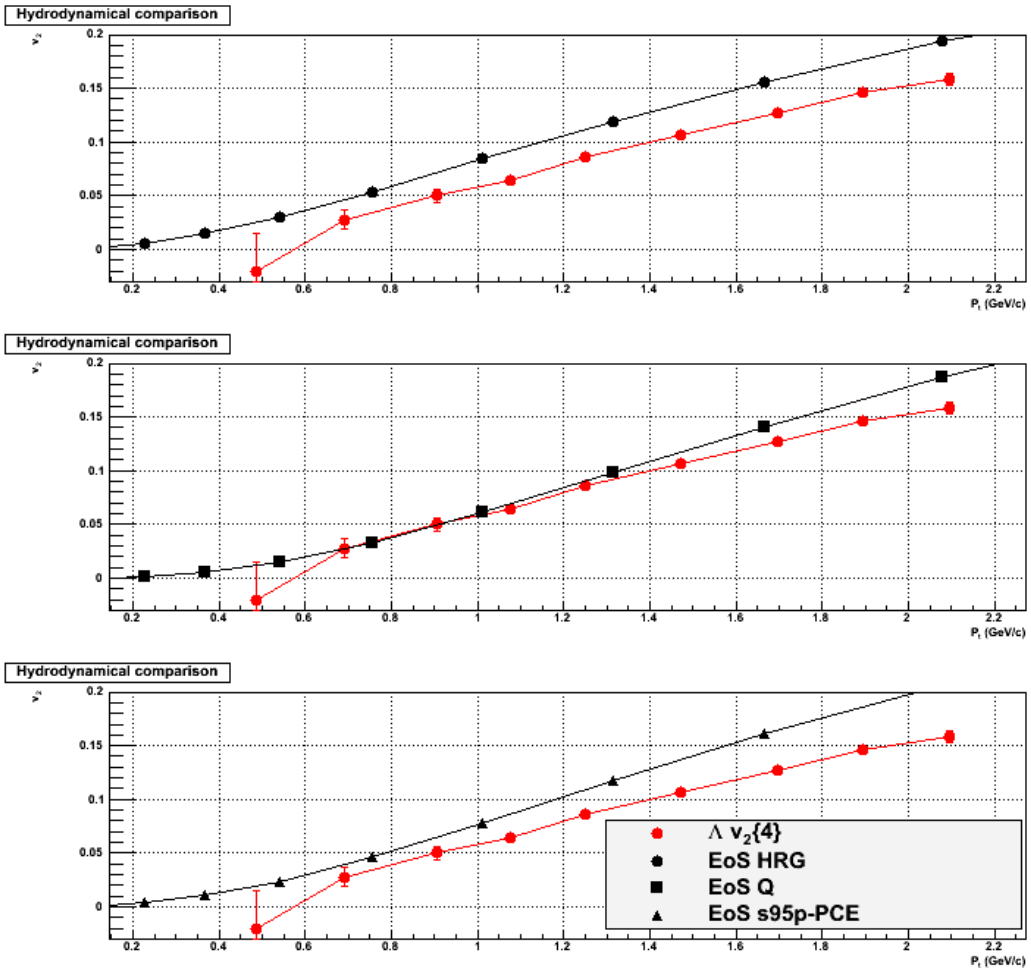

Figure 7.12: Λ versus p_t data versus hydrodynamical model comparison. Real data are shown by solid red circles. $10 - 40\%$ centrality.

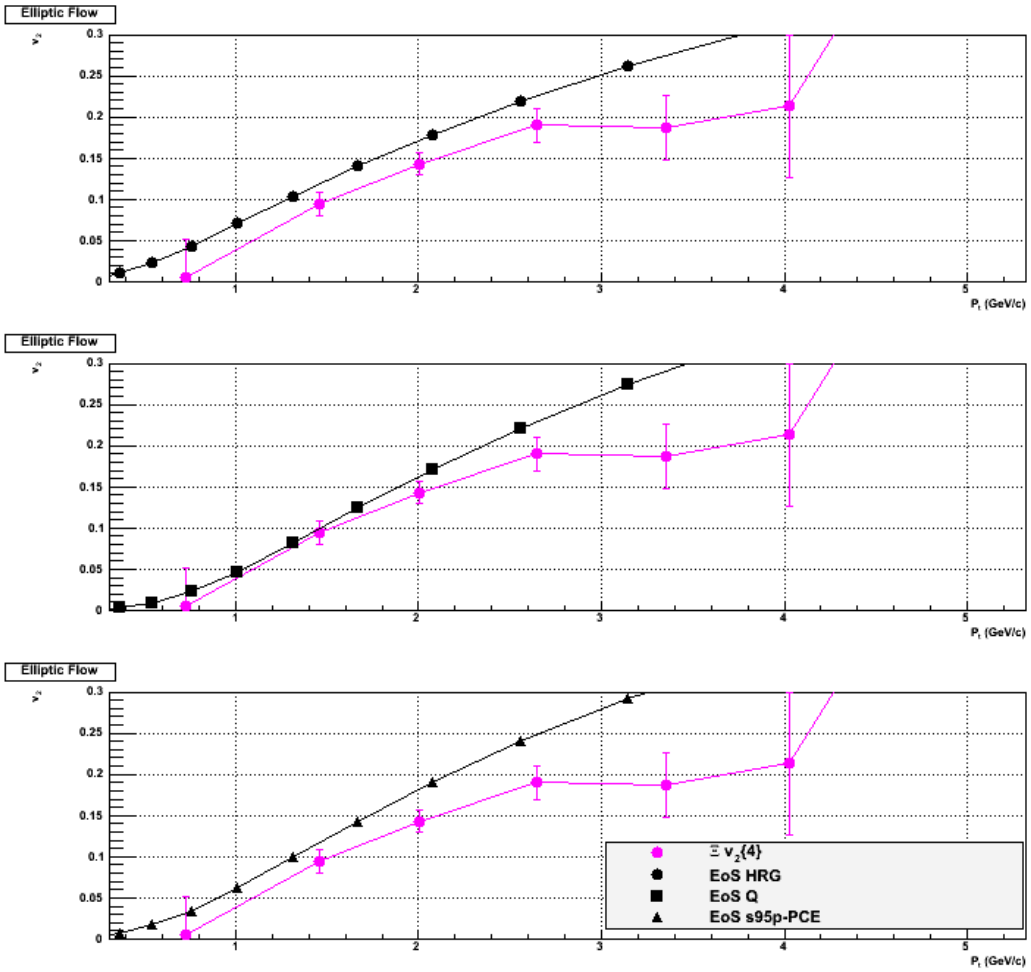

Figure 7.13: $\Xi^{\pm}$ versus p_t data versus hydrodynamical model comparison. Real data are shown by solid pink circles. $10-40\%$ centrality.

particle cumulants) had overestimated the magnitude of the true v_2. Incomplete thermalization and viscosity now seem to be real possibilities at RHIC.

The phenomenon of the mass hierarchy observed for both cumulant types at low-p_t also appears in the hydrodynamical models presented here. The initial spatial eccentricity of the nuclear overlap region induces elliptic flow for all particles. In the proceeding hydrodynamical evolutionary stage heavier particles gain more momentum than lighter particles through multiple scattering. Therefore, the v_2 "rise" observed in the data is effectively pushed to higher momentum for more massive particles. This leads to a mass hierarchy [Vol97][Huo01].

However, it is also interesting to note that a mass hierarchy at low p_t can also arise after the hydrodynamic stage in a coalescence model of hadronization [MV03] (assuming its validity in this p_t range). This comes about as heavier hadrons can be formed from quarks with larger relative momentum such that when they coalesce, their v_2 can interfere destructively. This feature was ignored in equation 7.22.

Elliptic flow continues to be a very useful tool in understanding early-time dynamics of heavy-ion collisions. Identified particle elliptic flow will soon be extended much further in p_t with the time of flight (TOF) upgrade at STAR. This will allow for a more critical comparison to future hydrodynamic models with viscosity and shed more light on the issue of viscosity and thermalization in heavy-ion collisions. Also, the LHC will soon collide Pb ions at an energy over $\sim$30 times higher than the highest energy at RHIC. It is expected for elliptic flow to continue to rise at these higher energies as viscous effects are expected to decrease.

APPENDIX A

QCD and its Vacua

The part of the SU(3)×SU(2)×U(1) invariant standard model Lagrangian dealing only with the intaractions of quarks and gluons is the subject of Quantum Chromodynamics. The SU(3) invarient QCD Lagrangian is given by:

$$L_{QCD} = -\frac{1}{4}F^{(a)}_{\mu\nu}F^{(a)\mu\nu} + i\sum_q \bar{\psi}^i_q \gamma^\mu (D_\mu)_{ij}\psi^j_q - \sum_q m_q \bar{\psi}^j_q \psi_{qi} \tag{A.1}$$

where

$$F^{(a)}_{\mu\nu} = \partial_\mu A^a_\nu - \partial_\nu A^a_\mu - g_s f_{abc} A^b_\mu A^c_\nu \tag{A.2}$$

and

$$(D_\mu)_{ij} = \delta_{ij}\partial_\mu + ig_s \sum_a \frac{\lambda^a_{ij}}{2} A^a_\mu \tag{A.3}$$

g_s is the QCD coupling constant. f_{abc} is the SU(3) group theory factor. λ^a_{ij} is a particular matrix element(i, j) of the element a in the SU(3) group.

The vacuum structure of QCD is studied when we only consider the first term of equation A.1. The topological charge of the vacuum is given by

$$\nu = \frac{g^2}{32\pi^2}\int d^4x F^a_{\mu\nu}\tilde{F}^a_{\mu\nu} \tag{A.4}$$

The solution with $\nu = 1$ in Euclidean space is given by [Hoo76]

$$A^a_\mu(x) = \frac{2}{g}\frac{\eta_{a\mu\nu}(x - x_0)^\nu}{(x - x_0)^2 + \lambda^2} \tag{A.5}$$

x_0 is free because of translational invarience. λ is a free scale parameter and η is a tensor which maps antisymmetric representations of SO(4) onto vectors of one of its two invarient subgroups SO(3):

$$\begin{aligned} \eta_{a\mu\nu} &= \epsilon_{a\mu\nu}(a, \mu, \nu = 1, 2, 3) \\ \eta_{a4\nu} &= -\delta_{a\nu}(a, \nu = 1, 2, 3) \\ \eta_{a\mu 4} &= \delta_{a\mu}(a, \mu = 1, 2, 3) \\ \eta_{a44} &= 0 \end{aligned} \tag{A.6}$$

APPENDIX B

Landau Levels

For a uniform applied magnetic field H in the z-direction the vector potentials can be given by:

$$\begin{aligned} A_x &= -Hy \\ A_y &= A_z = 0 \end{aligned} \tag{B.1}$$

The quantized wave functions for a particle in an applied magnetic field are given by the Landau eigenfunctions:

$$\psi_n = e^{(i/\hbar)(p_x x + p_z z)} \chi_n(y) \tag{B.2}$$

$$\chi_n(y) = \frac{1}{\pi^{1/4} a_H^{1/2} \sqrt{2^n n!}} \left[e^{-(y-y_0)^2/2a_H^2} \right] H_n\left(\frac{y - y_0}{a_H} \right) \tag{B.3}$$

$H_n(x)$ are the Hermite polynomials. H_0-H_3 are given below.

$$\begin{aligned} H_0(x) &= 1 \\ H_1(x) &= x \\ H_2(x) &= x^2 - 1 \\ H_3(x) &= x^3 - 3x \end{aligned} \tag{B.4}$$

APPENDIX C

Statistical Bias

The event cut applied at the end of chapter 6 for the out-of-plane analysis is

$$N_+^T = N_-^T \tag{C.1}$$

$$N_+^B = N_-^B \tag{C.2}$$

For the in-plane analysis we just replace (T,B) with (L,R) in the above equations. We now check to see if any statistical bias is introduced with these constraints for the case of fixed multiplicity M first. The same-sign number correlations are proportional to

$$\left\langle N_\pm^{T,B}(N_\pm^{T,B}-1) - 2N_\pm^T N_\pm^B \right\rangle \tag{C.3}$$

which equals zero for a purely statistical distribution of charges. We now impose the constrains of D.1 and D.2 on D.3 and obtain

$$\begin{aligned} \left\langle N_\pm^{T,B}(N_\pm^{T,B}-1) - 2N_\pm^T N_\pm^B \right\rangle &= \left\langle 2N_+^{T,B}(N_+^{T,B}-1) - 4N_+^T N_+^B \right\rangle \\ &= 2\left\langle N_+^{T,B}(N_+^{T,B}-1) - 2N_+^T N_+^B \right\rangle \\ &= 0 \end{aligned} \tag{C.4}$$

since N_+^T is still allowed to freely fluctuate. The opposite-sign correlations are proportional to

$$\left\langle 2N_+^{T,B}N_-^{T,B} - 2N_\pm^T N_\mp^B \right\rangle \tag{C.5}$$

Now we impose the constraints of D.1 and D.2 and obtain

$$\begin{aligned}
&\left\langle 2N_+^{T,B}N_-^{T,B} - 2N_\pm^T N_\mp^B \right\rangle \\
&= \left\langle 2(N_+^T)^2 + 2(N_+^B)^2 - 2N_+^T(N_- - N_-^T) - 2N_+^B(N_- - N_-^B) \right\rangle \\
&= \left\langle 4(N_+^T)^2 + 4(N_+^B)^2 - 2N_+^T N_- - 2N_+^B N_- \right\rangle \\
&= \left\langle 8(N_+^T)^2 - 4N_+^T N_- \right\rangle \\
&= 8\left[\sigma^2 + \left\langle N_+^T \right\rangle^2\right] - \frac{4}{2}N_+^2 \\
&= 8\left[N_+ p(1-p) + \frac{N_+^2}{4}\right] - 2N_+^2 \\
&= 2N_+ \qquad \text{(C.6)}
\end{aligned}$$

Here the binomial variance σ was inserted with p=.5 (the probability for a particle to be on top or bottom). The number correlations are then given by

$$\begin{aligned}
\frac{\left\langle 2N_+^{T,B}N_-^{T,B} - 2N_\pm^T N_\mp^B \right\rangle}{2N_+N_-} &= \frac{1}{N_-} \\
&= \frac{1}{N_+} \qquad \text{(C.7)}
\end{aligned}$$

So, we have found that the opposite sign-correlations recieve a statistical bias with this event cut. This result was for a fixed multiplicity M. We wish to now average this bias over all M within a standard centraliy bin. The multiplicity distribution for the Glauber Monte Carlo model of heavy-ion collisions is shown in figure D.1. The x-axis represents the total multiplicity $N_+ + N_-$. For the event cut, $N_+ = N_-$, so we must scale the x-axis by a factor of .5. Using the standard centrality definitions at STAR and incorporating the modulation factors of MNCs of the second type we obtain the final form of the statistical bias which is to be removed from the observed correlation under the event cut.

$$\left[\langle M\rangle^2_{in-plane} - \langle M\rangle^2_{out-plane}\right]\left\langle \frac{1}{N_+} \right\rangle \qquad \text{(C.8)}$$

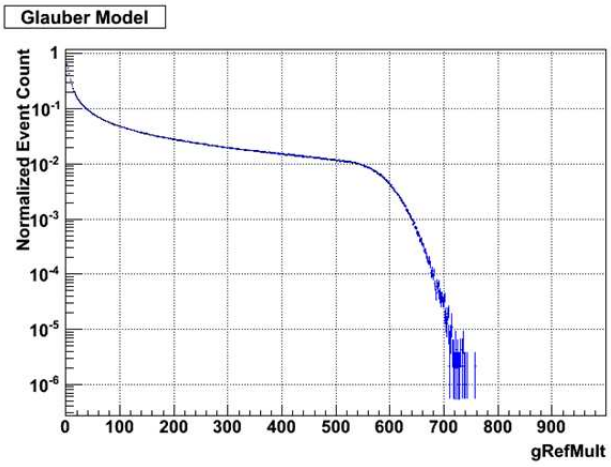

Figure C.1: Glauber Monte Carlo distribution of events vs. particle multiplicity in $|\eta| < .5$.

The averages are taken only over the multiplicities of a given centrality bin. Also, since the fiducial range used in chapter 6 is $|\eta| < 1$ whereas the multiplicty displayed on the x-axis of figure D.1 is for $|\eta| < .5$ we must scale up the multiplicities. The final scaling factors and the final statistical bias values obtained for each centrality bin are given below. Figure 6.14 reports the observed opposite-sign correlations minus these values.

Table C.1: Opposite-sign statistical bias values

Centrality	Scale factor	Statistical bias value
0-5%	1.79/2	.00007
5-10%	1.86/2	.0001
10-20%	1.96/2	.0002
20-30%	2.08/2	.0003
30-40%	2.19/2	.0005
40-50%	2.32/2	.00097
50-60%	2.45/2	.00178
60-70%	2.54/2	.0038
70-80%	2.55/2	.01

References

[Abe08a] B. I. Abelev et al. "Centrality dependence of charged hadron and strange hadron elliptic flow from $\sqrt{s_{NN}} = 200$ GeV Au+Au collisions." *Physical Review C*, **77**:54901, 2008.

[Abe08b] B. I. Abelev et al. "System-size independence of directed flow at the Relativistic Heavy-Ion Collider." *Phys. Rev. Lett.*, **101**:252301, 2008.

[Abe09] B. I. Abelev et al. "Azimuthal Charged-Particle Correlations and Possible Local Strong Parity Violation." *Phys. Rev. Lett.*, **103**:251601, 2009.

[Ack03] K.H. Ackermann et al. "STAR detector overview." *Nuclear Instruments and Methods in Physics Research A*, **499**:624–632, 2003.

[Ams08] C. Amsler et al. "Review of Paricle Physics." *Phys. Lett. B*, **667**:116–122, 2008.

[And03] M. Anderson et al. "The STAR time projection chamber: a unique tool for studying high multiplicity events at RHIC." *Nuclear Instruments and Methods in Physics Research A*, **499**:659–678, 2003.

[Arn03] L. Arnold et al. "The STAR silicon strip detector (SSD)." *Nuclear Instruments and Methods in Physics Research A*, **499**:652–658, 2003.

[BDO01] N. Borghini, P.M Dinh, and J.Y. Ollitrault. "Flow analysis from multiparticle azimuthal correlations." *Phys. Rev. C.*, **64**:054901, 2001.

[Bea04] I.G. Bearden et al. "Nuclear Stopping in Au + Au Collisions at $\sqrt{s_{NN}} = 200$ GeV." *Phys. Rev. Lett.*, **93**:102301, 2004.

[Ber03] F. Bergsma et al. "The STAR detector magnet subsystem." *Nuclear Instruments and Methods in Physics Research A*, **499**:633–639, 2003.

[Bie03] F.S. Bieser et al. "The STAR trigger." *Nuclear Instruments and Methods in Physics Research A*, **499**:766–777, 2003.

[Bjo83] J.D. Bjorken. "Highly relativistic nucleus-nucleus collisions: The central rapidity region." *Phys. Rev. D.*, **27**:140–151, 1983.

[Bro01] K.A. Brown. "Resonant Extraction Parameters for the AGS Booster." In *Proceedings of the 2001 Particle Accelerator Conference*, 2001.

[Che08] J. Chen et al. "Parton distributions at hadronization from bulk dense matter produced in Au+Au collisions at $\sqrt{s_{NN}} = 200$ GeV." *Physical Review C*, **78**:034907, 2008.

[Col85] S. Coleman. *Aspects of Symmetry.* Cambridge University Press, Cambride, U.K., 1985.

[Dia03] D. Diakonov. "Instantons at Work." *Prog. Part. Nucl. Phys.*, **51**:173–222, 2003.

[GW73] D. Gross and F. Wilczek. "Ultraviolet Behavior of Non-Abelian Gauge Theories." *Phys. Rev. Lett.*, **30**:1343–1346, 1973.

[Hah03] H. Hahn et al. "The RHIC design overview." *Nuclear Instruments and Methods in Physics Research A*, **499**:245–263, 2003.

[Hoo76] G. 't Hooft. "Symmetry Breaking through Bell-Jackiw Anomalies." *Phys. Rev. Lett.*, **37**:8–11, 1976.

[Huo01] P. Huovinen et al. "Radial and elliptic flow at RHIC: further predictions." *Phys. Lett. B*, **503**:58–64, 2001.

[Huo05] P. Huovinen. "Anisotropy of flow and the order of phase transition in relativistic heavy ion collisions." *Nuclear Physics A.*, **761**:296–312, 2005.

[Kar02] F. Karsh. "Lattice QCD at High Temperature and Density." *Lecture Notes in Physics*, **583**:209, 2002.

[KMW08] D.E. Kharzeev, L.D. McLerran, and H.J. Warringa. "The effects of topological charge change in heavy ion collisions: "Event by event P and CP violation."." *Nucl. Phys. A*, **803**:227–253, 2008.

[Leo94] W.R. Leo. *Techniques for Nuclear and Particle Physics Experiments.* Springer-Verlag, Heidelberg, Germany, 1994.

[LL77] L.D. Landau and E.M. Lifshitz. *Quantum Mechanics: Non-Relativistic Theory.* Pergamon Press Ltd., Oxford, U.K., 1977.

[LY56] T.D. Lee and C.N. Yang. "Question of Parity Conservation in Weak Interactions." *Physical Review*, **104**:254–258, 1956.

[Mid83] R. Middleton. "A Versatile High Energy Negative Ion Source." *Nuclear Instruments and Methods*, **214**:139–150, 1983.

[MV03] D Molnar and S.A. Voloshin. "Elliptic Flow at Large Transverse Momenta from Quark Coalescence." *Phys. Rev. Lett.*, **91**:092301, 2003.

[PV98] A.M. Poskanzer and S.A. Voloshin. "Methods for analyzing anisotropic flow in relativistic nuclear collisions." *Physical Review C*, **58**:1671–1678, 1998.

[Sau77] F. Sauli. "Principles of Operation of Multiwire Proportional and Drift Chambers." Lectures given in the Academic Training Programme of CERN, 1977.

[Sch86] W. Scharf. *Particle Accelerators and their Uses*. Harwood Academic Publishers, Chur, Switzerland, 1986.

[Sor03] P.R. Sorensen. "Kaon and Lambda Production at Intermediate p_T: Insights into the Hadronization of the Bulk Partonic Matter Created in Au+Au Collisions at RHIC." UCLA dissertation, 2003.

[Ste01] D.B. Steski et al. "Upgrade and Operation of the BNL Tandems for RHIC Injection." In *Proceedings of the 2001 Particle Accelerator Conference*, 2001.

[SV08] I. Selyuzhenkov and S.A. Voloshin. "Effects of nonuniform acceptance in anisotropic flow measurements." *Phys. Rev. C.*, **77**:034904, 2008.

[Vol97] S. Voloshin. "Transverse radial expansion and directed flow." *Phys. Rev. C*, **55**:1630, 1997.

[Vol04] S.A. Voloshin. "Parity violation in hot QCD: how to detect it." *Phys. Rev. C.*, **70**:057901, 2004.

[Wu57] C.S. Wu. "Experimental Test of Parity Conservation in Beta Decay." *Physical Review*, **105**:1413–1415, 1957.

[WV84] E. Whitten and C. Vafa. "Parity Conservation in Quantum Chromodynamics." *Phys. Rev. Lett.*, **53**:535–536, 1984.

[YHM05] K. Yagi, T. Hatsuda, and Y. Miake. *Quark-Gluon Plasma*. Cambridge University Press, Cambride, U.K., 2005.